SYNCHROTRON X-RAY ABSORPTION SPECTROSCOPY AND THERMAL ANALYSIS STUDY OF PARTICLE-REINFORCED ALUMINIUM ALLOY COMPOSITES

A Thesis Submitted to the College of Graduate Studies and Research
in Partial Fulfillment of the Requirements for the Degree of
Master of Science
in the Department of Mechanical Engineering
University of Saskatchewan
Saskatoon, Saskatchewan
Canada

By
Williams Alozie Uju

PERMISSION TO USE

In presenting this thesis in partial fulfillment of the requirements for the Masters degree from the University of Saskatchewan, I agree that the Libraries of this University may make it freely available for inspection. I further agree that permission for copying of this thesis in any manner, in whole or in part, for scholarly purposes may be granted by the professor who supervised my thesis work, Prof. I. N. A. Oguocha, or, in his absence, by the Head of the Department or the Dean of the College in which my thesis work was done. It is understood that any copying or publication or use of this thesis or parts thereof for financial gain shall not be allowed without my written permission. It is also understood that due recognition shall be given to me and to the University of Saskatchewan in any scholarly use which may be made of any material in my thesis.

Requests for permission to copy or to make other use of material in this thesis in whole or part should be addressed to:

Head of the Department of Mechanical Engineering
57 Campus Drive
University of Saskatchewan
Saskatoon, Canada, S7N 5A9

ABSTRACT

There is a great need in the transportation industry for high strength, high stiffness and lightweight materials with excellent dimensional stability. The use of these materials reduces fuel consumption and greenhouse gas emission as well as malfunctioning of components when subjected to fluctuating temperatures. Metal matrix composites (MMCs) are designed to meet these needs of transportation and other industries. However, their use is limited by lack of information on their thermal behaviour. In addition, reactions that occur in MMCs alter their microstructure and properties. These reactions have been widely investigated using X-ray Diffractometry (XRD) and electron microscopy (EM). However, these techniques cannot provide information such as charge transfer and local elemental structures in materials. Synchrotron X-ray Absorption Spectroscopy (XAS) could be used to identify reaction products in MMCs as well as provide information which XRD and EM cannot provide.

The thermal behaviour of Al-Mg alloy A535 containing fly ash particles as well as charge transfer and reactivity in particulate aluminium alloy metal matrix composites (MMCs) were investigated in this work. The materials studied were (i) Al-Cu-Mg alloy AA2618 and its composites reinforced with 10 and 15 vol.% alumina (Al_2O_3) particles and (ii) Al-Mg alloy A535 and its composites reinforced with a mixture of 5 wt.% fly ash and 5 wt.% silicon carbide, 10 wt.% and 15 wt.% fly ash. The investigative techniques used included Differential Scanning Calorimetry (DSC), Thermomechanical Analysis (TMA), Optical Microscopy (OM), Scanning Electron Microscopy (SEM), Energy Dispersive X-ray Spectroscopy (EDS), and synchrotron X-ray Absorption Spectroscopy (XAS).

The results obtained showed that the coefficient of thermal expansion (CTE) of A535 decreased with the addition of fly ash and silicon carbide. Also, the addition of these

particles improved the dimensional stability of the alloy in that the residual strain, ε_p, cycling strain, ε_c, and CTE decreased. The results obtained from XAS measurements showed evidence of charge redistribution in the aluminium in AA2618 with the addition of alumina particles. The results obtained from XAS measurements showed evidence of charge redistribution in the aluminium in AA2618 with the addition of alumina particles. The addition of alumina particles into AA2618 increased the *p*-orbital population and also changed the surface chemistry of the matrix. It was also demonstrated that the XAS technique can be used to determine the presence of various oxides in industrial fly ash and spinel ($MgAl_2O_4$) in alumina and fly ash particles extracted from the MMCs.

ACKNOWLEDGEMENT

I would like to express my profound gratitude to my supervisor, Professor I. N. A. Oguocha, for his expert advice, incisive and constructive criticism, careful attention to details and, in particular, his enthusiasm for my total well being. He was not only a supervisor, but also a friend indeed.

My appreciation goes to my supervisory committee members, Dr. R. Sammynaiken and Professor D. Torvi, for their invaluable support, advice, constructive criticism and useful suggestions. My special thanks also go to Professors M. Chaturvedi and O. Ojo of the University of Manitoba for use of their Scanning Electron microscopy (SEM) and Energy Dispersive Spectroscopy (EDS) facilities and Drs. Yangfeng Hu, Lucia Zuin, Robert Blyth and Tom Reiger of the Canadian Light Source (CLS) Inc., Saskatoon, for use of their XAS facilities. I also acknowledge Dr. Jason Lo, CANMET MTL, Ottawa (Canada), and Duralcan Aluminium Inc., San Diego (USA), for supplying the test materials. The technical assistance given to me by Mr. Robert Peace, Mr. Christopher James and other Departmental Assistants in Mechanical Engineering Department is gratefully acknowledged. I am also grateful to the entire Materials Science Group for their encouragement throughout this research.

With a profound sense of in-depth-gratitude and happy obligation, I thank my parents (Chukwuma and Odimara), siblings (Chikezie, Oguzie, Nkiru, Chidozie and Kelechi), and brother-in-law (Okechukwu Nwafor) for the unconditional love and affection they showed on me throughout this academic journey. The support and encouragement of Dr. and Mrs K. I. Chukwu and other friends are acknowledged.

The research fund given to my supervisor by the University of Saskatchewan and National Science and Engineering Research Council (NSERC) as well as the

scholarships awarded to me by the College of Graduate Studies and Research and Department of Mechanical Engineering are highly acknowledged.

To my God of compassion, who makes all things beautiful in his time, I pledge my absolute loyalty.

DEDICATION

To my parents and siblings

TABLE OF CONTENTS

TITLE PAGE

PERMISSION TO USE i

ABSTRACT ii

ACKNOWLEDGEMENT iv

DEDICATION vi

TABLE OF CONTENTS vii

LIST OF TABLES xi

LIST OF FIGURES xiii

NOMENCLATURE xvii

1.0 INTRODUCTION 1

1.1 Background 1

1.2 Motivation 2

1.3 Objectives 5

1.4 Thesis Outline 5

2.0 LITERATURE REVIEW 6

2.1 Metal Matrix Composites 6

2.2 Matrices Used for MMCs 7

2.2.1. Al-Cu-Mg Alloy AA2618 8

2.2.2 Al-Mg Alloy A535 9

2.3 Reinforcements Used for Fabricating Aluminium Metal Matrix Composites 9

2.4 Fly ash 11

2.5 Fabrication of Particulate Aluminium MMCs 13
2.6 Thermal Behaviour of Aluminium MMCs 14
2.6.1 Thermal Cycling Behaviour of Aluminium MMCs 14
2.6.2 The CTE of Aluminium MMCs 17
2.7 Factors Affecting the CTE of Aluminium MMCs 18
2.7.1 Effect of Service Temperature 18
2.7.2 Effect of the Nature of Reinforcements 19
2.7.3 Effect of the Volume Fraction and Size of Reinforcements 19
2.7.4 Effect of the Microcracks and Microvoids 20
2.8 Models for Prediction of CTE of MMCs 20
2.8.1 Rule of Mixtures 21
2.8.2 Turner's Model 21
2.8.3 Kerner's Model 22
2.8.4 Schapery's Model 23
2.9 Reactions in Aluminium MMCs 24
2.10 Experimental Techniques for Thermal Analysis and XAS Study of Aluminium MMCs 26
2.10.1 Optical Microscopy 26
2.10.2 Electron Microscopy 27
2.10.3 X-ray Diffractometry 27
2.10.4 Thermal Analysis 27
2.10.5 X-ray Absorption Spectroscopy 29
3.0 MATERIALS AND EXPERIMENTAL METHODS 33
3.1 Materials 33
3.2 Sample Preparation 34
3.2.1 Optical Microscopy and Scanning Electron Microscopy 34
3.2.2 X-ray Absorption Spectroscopy 35
3.2.3 Differential Scanning Calorimetry 35
3.2.4 Thermomechanical Analysis 36
3.3 Experimental Procedure 36

3.3.1 Optical Microscopy 36
3.3.2 Scanning Electron Microscopy 36
3.3.3 X-ray Diffractometry Measurements 36
3.3.4 X-ray Absorption Spectroscopy Measurements 37
3.3.5 Differential Scanning Calorimetry 41
3.3.6 Thermomechanical Analysis 42

4.0 RESULTS AND DISCUSSION 48
4.1 Thermal Behaviour Study of Aluminium alloy A535 and Its Composites 48
4.1.1 The Effect of Fly Ash on the Coefficient of Thermal Expansion of A535 48
4.1.2 Effect of Thermal Cycling on the Dimensional Stability of A535 and Its Composites 58
4.2 Reactivity in A535 MMCs 70
4.2.1 Microstructural Examination of A535 72
4.2.2 DSC Study of reactivity in A535 and its MMCs 78
4.3 X-ray Absorption Spectroscopy Study of Aluminium Alloys and their MMCs 95
4.3.1 X-ray Absorption Spectroscopy Study of AA2618 and its MMCs 95
4.3.2. X-ray Absorption Spectroscopy Study of Al-Mg Alloy A535 and Its MMCs Reinforced with Fly ash 106
4.4. Summary 115

5.0 CONCLUSIONS AND RECOMMADATIONS 119
5.1 Conclusions 119
5.2 Recommendations for Future Work 120

REFERENCES 121

APPENDIX 131
Appendix A. Operational Manuals 131
A.1.0 Standard Operational Procedure for Seteram DSC 111 131
A.1.1 Setting-up Experiment 131
A.1.2 Data Processing 133

A.1.3 Miscellaneous Information 134
A.2.0 Standard Operational Procedure for Seteram Evolution 2000 Thermomechanical Analyser 135
A.2.1 Setting-up Experiment 135
A.2.2 Data Processing 138
Appendix B A535 and its MMCs 139
B.1.0 Sample Calculations of the CTE of A535 and its MMCs 139
B.2.0 Peak temperatures and enthalpies of the reaction peaks in A535 and its MMCs (second sample) 142

LIST OF TABLES

Table 2.1. Designations of wrought and cast aluminium alloy.....8

Table 2.2. Typical physical and mechanical properties of A535 alloy.....10

Table 2.3. Properties of some oxides in fly ash and silicon carbide.....12

Table 3.1. Chemical compositions of AA2618 and its MMCs.....34

Table 3.2. Chemical composition of A535.....34

Table 3.3. Chemical composition of fly ash.....34

Table 3.4. Energy ranges used for XAS measurements.....39

Table 4.1. Average CTEs of the test materials obtained experimentally at 100 ^{o}C and those calculated using various models.....58

Table 4.2. Elemental compositions of the phases labeled *a*, *b*, and *c* in Figures 4.12 and 4.13.....78

Table 4.3. Average peak reaction temperatures and enthalpies of peaks labeled *a* and *b* in Figure 4.16.....80

Table 4.4. Average peak reaction temperatures and enthalpies of reactions labeled *b* and *c* in Figure 4.17.....83

Table 4.5. Average peak reaction temperatures and enthalpies of the peaks labeled *b′* and *c′* in Figure 4.18.....85

Table 4.6. Area under the peak in Al K-edge TEY spectra of AA2618 and its MMCs. .99

Table 4.7. Area under the peak in Al L-edge spectra of AA2618 and its MMCs. 103

Table 4.8. XRD analysis of extracted alumina. 105

Table 4.9. Area under the peak labeled *b* in Al K-edge spectra of industrial and extracted fly ash. 116

Table B.1.1. Properties of A535, Al-5 wt.% Mg, some oxides in fly ash, and silicon carbide. 139

Table B.1.2. Densities of the constituents of fly ash. 139

Table B.1.3. Vol.% of the constituents of fly ash. 139

Table B.2.1. Peak temperatures and enthalpies of the reaction peaks in the thermograms of A535. 142

Table B.2.2. Peak temperatures and enthalpies of the reaction peaks in the thermograms of A535/Hybrid/10_p. 142

Table B.2.3. Peak temperatures and enthalpies of the reaction peaks in the thermograms of A535/Fly ash/10_p. 143

Table B.2.4. Peak temperatures and enthalpies of the reaction peaks in the thermograms of A535/Fly ash/15_p. 143

LIST OF FIGURES

Figure 2.1. SEM micrograph of fly ash particles. 12

Figure 2.2. Typical thermal strain-temperature curve showing the formation of a hysteresis loop during thermal cycling. 16

Figure 2.3. A schematic of the potential energy curve of two atoms separated by a distance, *r*. 18

Figure 2.4. A typical DSC thermogram. 28

Figure 2.5. A schematic diagram of: (a) the electron-transitions that occur when an X-ray beam is incident on a material and (b) XAS spectrum. 30

Figure 2.6. Charge compensation mechanism between two elements in a material system. 32

Figure 3.1. A typical sample used for thermomechanical analysis. 37

Figure 3.2. Use of two-polynomial-fit in WINXAS^{TM} for (a) pre-edge background subtraction and (b) normalization. 40

Figure 3.3. Assignment of peak positions using PeakFit^{TM}. 40

Figure 3.4. Temperature-time profile used for DSC measurements. 42

Figure 3.5. Typical DSC thermograms of A535 and its MMCs: (a) below 100 ^{o}C and (b) above 750 ^{o}C. 43

Figure 3.6. Temperature-time profiles used for (a) CTE and (b) thermal cycling experiments. 45

Figure 3.7. Typical (a) average and (b) true CTEs of A535 and its MMCs. 47

Figure 4.1. Change in length (displacement) of A535 and its composites. 49

Figure 4.2. Comparison of average CTE of A535 obtained experimentally and that from reference [59]. 49

Figure 4.3. Variation of the average CTE of A535 with the addition of fly ash: (a) one test sample and (b) average of two test samples. The error bars are based on standard deviation. 51

Figure 4.4. Effect of double heat treatment on the CTE of: (a) A535, (b) A535/Hybrid/10_p, (c) A535/Fly ash/10_p and (c) A535/Fly ash/15_p. 52

Figure 4.5. Variation of instantaneous/true CTE with temperature for: (a) A535, (b) A535/Hybrid/10_p, (c) A535/Fly ash/10_p, (d) A535/Fly ash/10_p and (e) all samples. 55

Figure 4.6. Thermal displacement versus temperature plots obtained for A535 and the composites during thermal cycling. 59

Figure 4.7. Thermal strain versus temperature plots obtained for A535 and the composites during thermal cycling. 61

Figure 4.8. ε_p, ε_T, ε_c and $\Delta\varepsilon$ obtained for the test materials as a function of number of cycles. 64

Figure 4.9. ε_p, ε_T, ε_c and $\Delta\varepsilon$ obtained for the test materials as a function of number of cycles obtained from the strains computed by Setsoft 2000 software. 66

Figure 4.10. Average CTE versus number of thermal cycles obtained for A535 and the composites. The error bars are based on standard deviation. 69

Figure 4.11. Thermal displacement obtained for A535 and its composites after the (a) CTE and (b) thermal cycling experiments using the micrometer screw gauge. 70

Figure 4.12. Typical optical micrographs of as-received A535 showing the various phases present in it. 73

Figure 4.13. Typical optical micrograph of heat treated A535 showing the various phases present in it. 74

Figure 4.14. Typical SEM micrographs of the phases labeled a, b, and c in Figures 4.12 and 4.13. 75

Figure 4.15. Typical EDS spectra obtained from the phases labeled *a*, *b*, and *c* in Figures 4.12 and 4.13. 76

Figure 4.16. Typical DSC thermograms obtained for A535, Al and Mg on heating from 100 to 750 ^oC: The (a) complete thermographs, and its expanded views between (b) 100 and 500 ^oC and (c) 500 and 750 ^oC. 79

Figure 4.17. Typical DSC thermograms obtained for A535 and its composites on heating from 100 to 750 ^{o}C: The (a) complete thermograms, and its expanded views between (b) 100 and 400 ^{o}C, (c) 400 and 500 ^{o}C and (d) 500 and 750 ^{o}C.....81

Figure 4.18. Typical DSC thermograms obtained for A535 and its MMCs on cooling from 750 to 100 ^{o}C: (a) The complete thermograms, and its expanded views between (b) 100 and 500 ^{o}C and (b) 500 and 750 ^{o}C. 84

Figure 4.19. Typical DSC thermograms of A535 and its composites compared with that of fly ash on heating from 100 to 750 ^{o}C: (a) The complete thermograms, and its expanded views between (b) 100 and 400 ^{o}C, (c) 400 and 500 ^{o}C and (d) 500 and 750 ^{o}C. 86

Figure 4.20. Typical DSC thermograms of A535 and its composites compared with that of Al-Mg mixture on heating from 100 to 750 ^{o}C: (a) The complete thermograms, and its expanded views between (b) 100 and 400 ^{o}C, (c) 400 and 500 ^{o}C and (d) 500 and 750 ^{o}C.....89

Figure 4.21. Typical DSC thermograms of A535 and its composites compared with that of Al-Mg-fly ash mixture on heating from 100 to 750 ^{o}C: (a) The complete thermogram, and its expanded views between (b) 100 and 400 ^{o}C, (c) 400 and 500 ^{o}C and (d) 500 and 750 ^{o}C.....91

Figure 4.22. Typical DSC thermograms of A535 and its composites compared to that of Al-Mg-fly ash mixture on cooling from 750 to 100 ^{o}C: (a) The complete thermograms, and its expanded views between (b) 100 and 400 ^{o}C, (c) 400 and 500 ^{o}C and (d) 500 and 750 ^{o}C.....93

Figure 4.23. Typical Al K-edge spectra of AA2618 and its composites before pre-edge background subtraction and post-edge normalization. (a) TEY and (b) FLY. 96

Figure 4.24. Typical Al L-edge FLY spectra of AA2618 and its composites before pre-edge background subtraction and post-edge normalization. 97

Figure 4.25. Normalized TEY and FLY Al K-edge spectra for high-purity Al, AA2618 and its MMCs: (a) TEY of high-purity Al and AA2618, (b) TEY of AA2618 and its MMCs, (c) FLY of high-purity Al and AA2618 and (d) FLY of AA2618 and its MMCs. 97

Figure 4.26. Normalized Al L-edge XAS spectra for high-purity Al, spinel, high-purity alumina, AA2618 and its MMCs: (a) High-purity aluminium, spinel and alumina, (b) high-purity aluminium and AA2618, (c) AA2618 and its MMCs and (d) AA2618 MMCs and high-purity alumina. 101

Figure 4.27. Normalized FLY Al L-edge spectra from (a) extracted alumina and high-purity alumina and (b) spinel and extracted alumina. 104

Figure 4.28. XRD diffraction patterns of extracted alumina. 105

Figure 4.29. Typical Mg K-edge spectra of industrial fly ash before pre-edge background subtraction and post-edge normalization: (a) TEY and (b) FLY. 107

Figure 4.30. Typical Mg K-edge spectra of extracted fly ash before pre-edge background subtraction and post-edge normalization: (a) TEY and (b) FLY. 108

Figure 4.31. Typical Al K-edge spectra of extracted fly ash and fly ash before pre-edge background subtraction and post-edge normalization: (a) TEY and (b) FLY. 109

Figure 4.32. Typical Si K-edge spectra of extracted and industrial fly ash before pre-edge background subtraction and post-edge normalization: (a) TEY and (b) FLY. 110

Figure 4.33. Normalized TEY and FLY Al K-edge spectra of industrial fly ash and Al_2O_3 and spinel: (a) TEY and (b) FLY. 111

Figure 4.34. Normalized TEY and FLY Si K-edge spectra of industrial fly ash, SiO_2, and graphite tape: (a) TEY and (b) FLY 112

Figure 4.35. Normalized TEY and FLY of Al K-edge of extracted fly ash, industrial fly ash and spinel. 113

Figure 4.36. Normalized TEY and FLY of Al K-edge spectra of extracted fly ash, industrial fly ash, SiO_2, and graphite tape: (a) TEY and (b) FLY. 115

NOMENCLATURE

Acronyms

AA	Aluminium Association
CCBs	Coal Combustion By-products
CLS	Canadian Light Source
CTE	Coefficient of Thermal Expansion
$\overline{\text{CTE}}$	Average of the Average Coefficient of Thermal Expansion
CSA	Canadian Standard Association
DSC	Differential Scanning Calorimeter or Differential Scanning Calorimetry
DTA	Differential Thermal Analysis
EDS	Energy Dispersive X-ray Spectroscopy
EM	Electron Microscopy
EXAFS	Extended X-ray Fine Structure
FLY	Fluorescence Yield
MMCs	Metal Matrix Composites
NEXAFS	Near-Edge X-ray Absorption Fine Structure
OM	Optical Microscopy
ROM	Rule of Mixture
SGM	Spherical Grating Monochrometer
SOP	Standard Operational Procedure
TA	Thermal Analysis

TEM Total Electron Yield

VLS-PGM Variable Line Spacing Plane Grating Monochrometer

TMA Thermomechanical Analyzer or Thermomechanical Analysis

XAS X-ray Absorption Spectroscopy

XRD X-ray Diffractiometry or X-ray Diffraction

Symbols

$CE_{(T)}$	Expansion coefficient at temperature T of the the sample ($\mu/^{o}C$)
$CR_{(T)}$	Expansion coefficient at temperature T of the the reference sample ($\mu/^{o}C$)
$CP_{(T)}$	Expansion coefficient at temperature T of the the tube ($\mu/^{o}C$)
$D_{1(T)}$	Displacement of sample at T (μm)
$D_{2(T)}$	Displacement of reference sample at T (μm)
E	Energy (eV) and Young's modulus (N/m^2)
E	Sample length (mm)
$F(T)$	Temperature distribution function
G	Shear modulus of the reinforcement (N/m^2)
K	Bulk modulus (N/m^2)
l	Final sample length (mm)
l_o	Original sample length (mm)
m	Weight of sample (mg)
m_1	Weight of sample + crucible (mg)
m_2	Weight of crucible (mg)
r	Interatomic distance (Å) and reference sample length (mm)
T	Temperature (^{o}C)
U	Potential energy (J)
V	Volume fraction (m^3)
dL/dT	The first derivative of the final length with respect to temperature
ε	Thermal strain

ε_c	Thermal cyclic strain
$\Delta\varepsilon$	Strain height
ΔG	Gibbs free energy of a reaction (kJ/kg)
α	Coefficient of thermal expansion ($^oC^{-1}$)
σ	Thermal stress (N/m^2)
hv	Energy (eV)
v	Poison's ratio
$\overline{\alpha}$	Coefficient of thermal expansion calculated using the rule of mixture ($\mu/^oC$)
$\Delta\alpha$	The difference between the coefficient of thermal expansion of the reinforcement and that of the matrix ($\mu/^oC$)

Subscripts

c	Composite
m	Matrix
o	Equilibrium potential energy and interatomic distance
P	Residual thermal plastic strain
r	Reinforcement
T	Total thermal strain

Superscripts

Lower	Lower limit
Upper	Upper limit

1.0 INTRODUCTION

1.1 Background

Aluminium alloys have attractive properties such as high specific strength and stiffness, very good formability, good thermal and electrical conductivities, high ductility and weldability, and excellent atmospheric corrosion resistance which have made them choice materials for many engineering applications [1-8]. They are used widely in manufacturing components for aircrafts, ships, automobiles and sensitive measuring instruments. Among the commercially available aluminium alloys that are used widely in industries are A535 and AA2618.

A535 is a non-age-hardenable cast aluminium alloy with approximately 6.2 wt.% magnesium. It has good corrosion resistance against mild alkaline and salt spray exposure, which makes it well suited for automotive and military applications [6]. Its exceptionally dimensional stability makes it a good material for use in welded structures [7, 9] and parts of computing devices, aircrafts and missile guidance systems [8] and measuring instruments [4].

AA2618 is an age-hardenable wrought aluminium alloy with copper and magnesium as the main alloying elements. Its good elevated temperature strength makes it an attractive material for fabricating automobile and aircraft engine components [1]. It exhibits three aging sequences, with the main stable phases being *S* (Al_2CuMg) [10-14], θ (Al_2Cu) [13] and *X* [13, 14]. It also contains intermetallic phases such as AlCuNi, $(CuFe)Al_3$ and Al_9NiFe [12, 14, 15] which result from solid-state reactions between aluminium and the alloying elements. The Copper-rich intermetallics reduce the amount of copper atoms available for solid solution strengthening. However, the aluminide phase (Al_9NiFe) forms preferentially when iron and nickel are in small amount, making more copper

atoms available for solid solution strengthening [15].

To enhance the mechanical and thermal properties as well as the wear resistance of AA2618 and A535, they have been reinforced with ceramic particles to form metal matrix composites. A535 has been reinforced with fly ash (FA) [16, 17] and silicon carbide (SiC) [16], while AA2618 has been reinforced with alumina (Al_2O_3) [13, 18], aluminium nitride (AlN) [19] and SiC [20] particles. Ceramic particles have high hardness, high stiffness, very good wear resistance and low coefficient of thermal expansion (CTE) when compared with the metal matrix. The difference in CTE between the matrix and the reinforcing ceramic particles induces thermal mismatch stress in the composite during cooling from the fabrication and heat treatment temperatures [21-24]. In addition, chemical reactions occur between the matrix and the reinforcement phases in MMCs, thereby complicating the analysis of their properties and microstructures [16, 25-33].

1.2 Motivation

Many structural components in aerospace, automobile, measuring instrument and electronic devices are subjected to steady and fluctuating temperatures. Components subjected to temperature fluctuations could fail when the induced thermal stress is more than the yield strength of the material used [18, 22]. As such, materials used in such applications should be dimensionally stable (i.e., low and stable CTE and high specific heat capacity (C_p)) to avoid malfunctioning and catastrophic failures.

The thermal properties of aluminium alloy MMCs depend on such factors as the properties of the matrix, fabrication technique, amount of reinforcement material present and properties of the interfacial phase between the reinforcement and matrix [22, 35-37]. For example, the CTE of aluminium alloys A360 and A359 was reported to decrease with the addition of SiC [35, 37], which was attributed to the low CTE of SiC particles. As the volume fraction of SiC in A359 increased from 10 to 40%, its CTE decreased from about 16.2 to 10 μ^oC^{-1} at 25-50 ^oC [35]. Interfacial reactions that occur between the

reinforcement and the matrix affect the CTE of particulate aluminium MMCs. Fei and Wang [38] reported that as solutionalizing time of AA6061 reinforced with *β*–eucryptide ($LiAlSiO_4$) increases, the CTE of the composite increases due to the consumption of the *β*–eucryptide in interfacial reactions with the matrix. Studies on the effect of ceramic particles on the thermal behaviour of aluminium alloy A535 are scarce in the open literature. The lack of this knowledge will limit the use of its MMCs in applications where stringent dimensional stability is a critical materials selection criterion. Therefore, it is important to investigate the effect of ceramic particles on the thermal behaviour of A535.

The microstructure and properties of MMCs are affected by chemical reactions between the matrix and the reinforcement [16, 25-33]. Although ceramic particles are considered inert, there is a thermodynamic tendency for some of them (e.g., zirconia (ZrO_2), titania (TiO_2), alumina and silicon oxide (SiO_2)) to react with magnesium-containing aluminium alloys to form spinel ($MgAl_2O_4$), magnesium oxide (MgO), magnesium dititanate ($MgTi_2O_5$) or some combination of these reaction products during fabrication [13, 16, 25-33]. Mcleod *et al.* [26] have reported the formation of spinel in Al-1 wt.% Mg aluminium alloy reinforced with alumina and this reduced the amount of magnesium in the alloy. Spinel has also been detected in AA2618 [13, 33] and A535 [16, 25, 39] reinforced with alumina and fly ash, respectively. Banerjee and Rohatgi [30] observed reaction zones, which are rich in magnesium, around the zirconia and titania reinforcements in Al-11.8 wt.% Si-1 wt.% Mg aluminium alloy. The changes observed in the microstructures of particulate MMCs suggest that ceramic particles alter the chemistry and charge compensation mechanisms of the matrix.

Reactions in aluminium alloy MMCs have been studied using the Transmission Electron Microscopy (TEM) [27, 29, 40, 41], Scanning Electron Microscopy (SEM) [13, 16, 42, 43], Thermal Analysis (TA) [44-47], X-ray Diffractometry (XRD) [39, 43, 48], Optical Microscopy (OM) [39, 49] and Energy Dispersive X-ray Spectroscopy (EDS) [13, 16, 41]. However, the use of these techniques is limited by several factors. The TEM requires high operational skill and extensive sample preparation (which could change the

structure of the sample) to produce the thin electron-transparent samples. The resolution of SEM is affected by charging of non-conducting intermetallic particles and reaction products in aluminium alloy MMCs. The optical microscope has limited resolution power, while EDS has poor resolution, detection limits and signal-to-noise ratio. An alternative or complementary technique to these techniques is synchrotron X-ray Absorption Spectroscopy (XAS). Unlike the TEM, the use of conventional XAS requires less operational skills, and sample preparation is not very time consuming and costly. In XAS, the fluorescence and electron yields from conductive materials are not affected by charging effect. XAS can be used to identify and quantify chemical species present in a material. It can also be used to probe unoccupied states to give information on electronic structure as well as to obtain local structural information.

XAS can be used to provide information about chemical species present in materials [50-52] because it is sensitive to change in valency, coordination number and bond length. Mondal *et al.* [50] used XAS technique to show that Cr-P obtained via electron deposition is amorphous. Pattanaik *et al.* [51] used XAS to determine the structure of various calcium minerals present in cementitiuos materials derived from coal combustion by-products (CCBs). XAS was used to identify phases present in cubic boron nitride based composites [52].

The use of XAS to study the electronic structure and identify phases in aluminium alloys reinforced with ceramic particles is very scarce in the open literature. In this study, the electronic structure of AA2618 reinforced with ceramics was investigated using the Al K-edge ($1s \rightarrow 3p$ transition) and L-edge ($2p \rightarrow 3d$ transition) XAS. An understanding of the electronic structure of the aluminium in the AA2618 MMCs will be useful in tailoring them to meet the desired electrical properties. In addition, XAS was used to identify phases present in AA2618 MMCs and A535 MMCs.

1.3 Objectives

The objectives of this research work were:

1. To investigate the effect of ceramic particles on the thermal expansion behaviour of A535.
2. To study reactivity in aluminium alloys reinforced ceramic particles.
3. To probe the effect of the addition of alumina particles on the electronic structure of AA2618 using XAS.

1.4 Thesis Outline

This thesis is divided into five chapters. Chapter one gives background information on the subject matter studied and the scope of the work carried out. Chapter two reviews the literature pertaining to the present work. The materials and experimental procedures used are discussed in chapter three. Chapter four presents and discusses the results obtained. Chapter five presents the conclusions obtained from this work and gives recommendations for further studies.

2.0 LITERATURE REVIEW

This chapter reviews topics that are pertinent to the studies carried out in this thesis. The topics include metal matrix composites (MMCs), aluminium alloys, fly ash, thermal behaviour of MMCs, reactivity in MMCs, and experimental techniques for investigating the thermal behaviour and reactivity in MMCs.

2.1 Metal Matrix Composites

Metal matrix composites (MMCs) are made up of a metal matrix and a reinforcement. When a matrix contains two or more reinforcements, the resulting MMC is called a hybrid MMC. MMCs are made by dispersing the reinforcement phase(s) into a metal matrix via solid-state or liquid-state processing routes. MMCs are usually classified as continuous fiber-reinforced, whisker or short fiber-reinforced and particle-reinforced MMCs. Their properties are derived from a combination of the high strength, high stiffness, superior wear resistance, and excellent dimensional stability of the reinforcement material(s) with the good ductility of a metal-matrix. One major limitation to the applications of MMCs is cost. Thus, they are used in areas where a combination of properties that cannot be found in a monolithic material is required.

MMCs have good properties that make them attractive for solving many engineering materials problems. The main advantage they have over unreinforced alloys is that their properties can be tailor-made to meet a specific service requirement through appropriate selection of the base alloy, reinforcement and processing technique. They are used in aerospace, automotive and marine industries for fabricating components such as electrical contacts, robotic arms, cutting tools, nozzles, spark plug electrodes, bearings, pistons, drive shafts, cylinders and brake rotors [22, 53].

2.2 Matrices Used for MMCs

Metal matrices used for developing MMCs include aluminium and its alloys, titanium alloys, magnesium and its alloys, copper, cobalt, silver and nickel [22]. Among them, aluminium and its alloys have been used extensively in the fabrication of particulate MMCs due to their relative low cost, high strength-to-weight ratio, high toughness and excellent atmospheric corrosion resistance [6, 22, 53, 54]. Aluminium-based MMCs have been used in manufacturing automobile engine parts such as drive shafts, brake drums and discs, connecting rods, cylinder liners, motor block and pistons [53].

Aluminium alloys are classified as either cast or wrought aluminium alloys based on their manufacturing processes. Wrought aluminium alloys are processed into final product by extrusion, rolling, pressing, forging or a combination of these fabrication techniques. They are sub-classified into heat treatable and non-heat treatable alloys. The microstructure and properties of heat-treatable wrought aluminium alloys change with age-hardening heat treatment (precipitation hardening), while those of non-heat treatable aluminium alloys are not altered. The non-heat treatable wrought alloys are strengthened either by stain-hardening, solid solution strengthening or a combination of both. Wrought aluminium alloys are classified based on a 4-digit system given by the Aluminium Association (AA), where the first digit indicates the major alloying element(s) [1, 9]. Table 2.1 shows the AA designations of wrought and cast Al alloys as well as the main alloying elements in them [9].

Cast aluminium alloys are cast into the desired shape. Similar to wrought aluminium alloys, they are sub-classified as either heat treatable or non-heat treatable, depending on how their properties react to heat treatment. They are designated by a 4-digit system of the Aluminium Association, with a decimal point separating the last 2 digits [1, 9]. The first digit indicates the major alloying element(s) in the alloy, while the last digit indicates the product form (i.e., castings and ingots designated by “0” and “1”, respectively).

Table 2.1. Designations of wrought and cast aluminium alloy [9].

AA Designation		Main alloying elements
Wrought Aluminium alloy	Cast Aluminium alloy	
1XXX	1XX.X	High-purity Aluminium (Al)
2XXX	2XX.X	Copper (Cu)
3XXX	3XX.X	Manganese (Mn)
4XXX	4XX.X	Silicon (Si)
5XXX	5XX.X	Magnesium (Mg)
6XXX	6XX.X	Magnesium and Silicon
7XXX	7XX.X	Zinc (Zn)
8XXX	8XX.X	Others

2.2.1. Al-Cu-Mg Alloy AA2618

Aluminium alloy AA2618 is an age-hardenable wrought aluminium alloy with copper and magnesium as the main alloying elements. It also contains other elements such as iron and nickel to produce a variety of strengthening phases in the alloy which enhance the stability of the alloy at high temperatures. It was developed for manufacturing components exposed to high temperature in automobile and aerospace industries [1]. It has been used as a matrix material for fabricating MMCs [18-20, 41, 42, 55].

AA2618 derives its strength from a combination of precipitation and dispersion hardening [10-14]. It exhibits three aging sequences, with the stable phases being *S* (Al_2CuMg) [10-14], θ (Al_2Cu) [13] and *X* [13-15]. It also contains intermetallic phases such as AlCuNi, $(CuFe)Al_3$ and Al_9FeNi which arise from solid-state reactions between aluminium and alloying elements in AA2618 [12, 14, 15]. The Cu-rich phases reduce the amount of copper available for solid solution strengthening of the alloy [15]. However, the Al_9FeNi phase forms preferentially over the copper-rich phases when iron and nickel are in the ratio of about 1:1 [15]. The presence of Al_9FeNi phase in the alloy helps to control grain size, the amount of copper available for solid solution strengthening, and impede movement of dislocations [15].

2.2.2 Al-Mg Alloy A535

Aluminium alloy A535 (also called Almag 35 or A05350) is a cast aluminium alloy with magnesium as its main alloying element. It has the highest combination of strength, shock resistance and ductility of any cast aluminium alloy [57]. It has good corrosion resistance against mild alkaline and salt spray exposure, which makes it well suited for automotive, marine and military applications [6]. Its exceptional dimensional stability makes it a good material for fabricating brackets, C-clamps and optical equipment [8] as well as parts of computing devices, aircrafts and missile guidance systems [6, 55]. Table 2.2 shows typical properties of as-cast A535 [6, 7, 56].

The limitations to the use of A535 is that it is slightly (about 10%) more expensive than most cast aluminium alloys [57]. It is not easy to cast the alloy in permanent moulds as it is prone to hot shortness because of its long freezing range [6, 54]. However, the fabrication cost is often offset by the good mechanical properties and dimensional stability it exhibits [6, 7].

2.3 Reinforcements Used for Fabricating Aluminium Metal Matrix Composites

The materials usually used as reinforcement in MMCs include carbides (e.g., SiC, TiC, B_4C, WC), oxides (e.g., Al_2O_3, SiO_2), nitrides (e.g., SiN_4, AlN) and single element materials (e.g., C, Si). These reinforcements are usually in the form of continuous fibers, short fibers, and particles. A continuous fiber has an aspect (length-to-width) ratio > 1000, while a short fiber and a particle have aspect ratios of 10-1000 and 1–4, respectively [22]. Of these three forms, particulate reinforcements (e.g., SiC and alumina) have been used more than the others because they are available in several varieties at a relatively low cost [22]. Also, the manufacturing techniques used for fabricating particulate MMCs are very similar to those used for conventional alloys [22].

Table 2.2. Typical physical and mechanical properties of A535 alloy.

Properties	Values*
Tensile strength (0.5% extension underload)	275.8 MPa [7]
Tensile Strength (As-cast sample)	250 MPa [6]
Yield strength (0.5% extension under load)	144.8 MPa [8]
Yield Strength of As-cast sample (0.2% extension under load)	124 MPa [6]
Shear strength	193.1 MPa [7]
Elongation (2 inch gauge length)	13% [6]
Elongation (As-cast sample)	9% [7]
Compressive yield strength	165.5 MPa [7]
Density	2629.6 kg/m^{3}K [6]
Thermal conductivity @ 25 ^{o}C	96.3 W/mK [7]
Coefficient of thermal expansion (20 – 100 ^{o}C)	23.6 μ/^{o}C [7]
Coefficient of thermal expansion (20 – 300 ^{o}C)	26.6 μ/^{o}C [7]
Coefficient of thermal expansion (-50 – 20 ^{o}C)	21.6 μ/^{o}C [56]
Coefficient of thermal expansion (20 – 100 ^{o}C)	23.4 μ/^{o}C [56]
Coefficient of thermal expansion (20 – 200 ^{o}C)	25.6 μ/^{o}C [56]
Coefficient of thermal expansion (20 – 300 ^{o}C)	26.6 μ/^{o}C [56]
Melting range (liquidus-solidus) in ^{o}C	548.9-640.1 [7]
Brinell hardness	70 [7]
Resistance to hot cracking	F [7]
Pressure tightness	F [7]
Fluidity	VG [7]
Solidification shrinkage tendency	F [7]
Strength at elevated temperatures	F [7]
Corrosion resistance	E [7]
Machineability	E [7]
Polishing	E [7]
Gas welding	G [7]
Arc welding	G [7]
Electroplating	VG [7]
Brazing	No [7]
Normally heat-treated	No [7]
Anodizing appearance	Many colors [7]

* E, VG, G and F represent excellent, very good, good and fair, respectively. Numbers in square bracket are references

2.4 Fly ash

Fly ash is a by-product of coal combustion which is extracted from the exhaust gases using bag houses or electrostatic precipitators. It contains oxides of silicon, aluminium, iron, magnesium and calcium [59]. Figure 2.1 shows a typical SEM micrograph of fly ash particles. They are spherical particles with size varying from 1 to 100 μm and their density ranges between 1.3 and 4.8 g/cm^3 [16].

Fly ash can be classified based on either the ASTM C 618 standard (2004) or the Canadian Standard Association (CSA). ASTM C 618 standard classifies fly ash into three groups, namely, classes N, F and C. Classes N, F and C fly ash are produced from the combustion of raw or calcined natural pozzalans, anthracite or bituminous coal, and lignite or sub-bituminous coals, respectively. The sum of weight percentages of silicon oxide (SiO_2), alumina (Al_2O_3) and iron oxide (Fe_2O_3) contained in classes N and F fly ash is 70 wt.%, while that in class C fly ash is 50 wt.%. The CSA classifies fly ash as classes F, CI, or CH based on its calcium oxide content. Class F fly ash has < 8 wt.% calcium oxide, while classes CI and CH have 8-20 wt.% and > 20 wt.% calcium oxide, respectively. Table 2.3 shows some of the properties of the main constituents of fly ash and those of SiC [60]. As can be seen, the CTEs of alumina and magnetite are higher than that of SiC.

Fly ash production is increasing as nations industrialize and the demand for electricity increases. In 2002, 4.7 million metric tons of fly ash was generated in Canada out of which only 25% was utilized as a supplementary cementing material in cement and concrete, and filler material in paints [59, 61]. The remaining 75% was dumped in landfills, ash dams and lagoons and as such pose a disposal problem. In order to alleviate the economic, environmental and land use problems associated with its disposal, considerable efforts have been made to find alternative uses for it. A potential application for fly ash is as a reinforcement material in metal matrix composites (MMCs) [16, 36, 55, 62, 63].

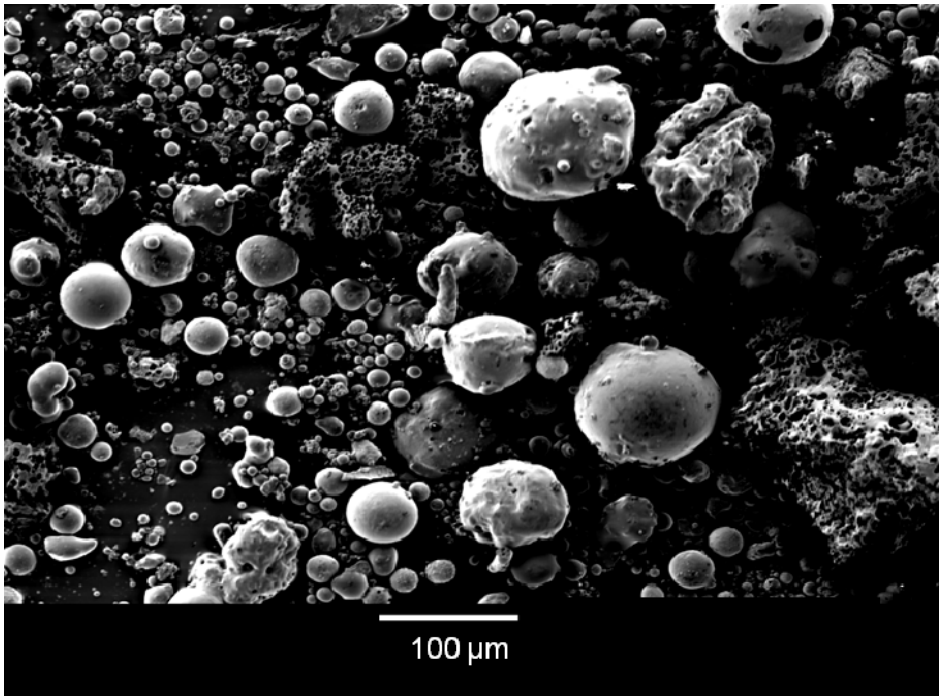

Figure 2.1. SEM micrograph of fly ash particles [16].

Table 2.3. Properties of some oxides in fly ash and silicon carbide [60].

Materials	Bulk Modulus (GPa)	Shear Modulus (GPa)	CTE (µ /^{o}C)
Alumina (Al_2O_3)	322.5	180	8.1
Silica (SiO_2)	35.9	28.6	1.2
Magnetite (Fe_2O_3)	222	60.3	8.72
Silicon Carbide (SiC)	221	200	4.1

Fly ash is an inexpensive resource of solid and hollow spheres. Its low cost as well as lightweight makes the use of the MMCs reinforced with it cost effective. Guo *et al.* [44] reported a decrease in the density of aluminium-fly ash composite with increase in fly ash content. Similarly, Rohatgi *et al*. [55] reinforced fly ash reinforcement in aluminium reduces the weight of the aluminium-matrix as well as improves its dimensional stability. In addition, the substitution of some percentage of aluminium alloys with fly ash to form composites reduces the energy and green house gases emitted during the production of aluminium alloys.

2.5 Fabrication of Particulate Aluminium MMCs

There are two methods for fabricating particulate MMCs, namely, solid state and liquid state processes. An example of solid state process is powder metallurgy, while that of liquid state process is stir casting. The method of fabrication and the details of any post fabrication processes such as extrusion, forging and pressing affect the physical, chemical, thermal, tribological and mechanical properties of the MMCs.

Solid state processing involves mixing ceramic and metal powders homogenously followed by extrusion, pressing, sintering, or forging [22]. Several microstructural changes, such as particle fracture, morphology, poor interfacial bonding and alignment of reinforcement particles along the extrusion or forging axis occur in composites fabricated via solid state processes [22, 32, 63]. Guo *et al.* [63] fabricated aluminium–fly ash composites via a powder metallurgy route followed by sintering. They reported a decrease in the strength and hardness of the composites due to plastic deformation of the aluminium matrix and poor interfacial bonding between fly ash particles and aluminium-matrix. They concluded that powder metallurgy was not very promising for producing aluminium-fly ash composites. In addition, the use of powder metallurgy is limited by the cost of production as well as the generation of high material waste [22].

The liquid-state processing technique involves mixing of liquid metal matrix and the reinforcement(s). It can be carried out through either direct addition of particles into the molten metal while stirring continuously (stir casting technique) or infiltrating the molten metal matrix into a particulate preform (pressure infiltration technique). The advantages of the liquid-state technique are its relatively low cost and capability of producing large complex shapes [22, 62]. The liquid-state process has been used extensively in fabricating particulate aluminium MMCs [22, 55, 62, 64]. Rajan *et al.* [64] used stir casting to synthesize Al-7 wt.% Si-0.35 wt.% Mg composite reinforced with 9 vol.% fly ash. Rohatgi *et al.* [62] also used stir casting technique to successfully disperse fly ash in aluminium alloy A356. In another work, Rohatgi *et al.* [55] synthesized aluminium-fly ash composites with a high volume fraction (65%) of fly ash

cenospheres via the pressure infiltration technique. The fabrication of MMCs through liquid state process is limited by the inability to control reinforcement distribution in the matrix as well as the adverse interfacial reactions that occur between the matrix and the reinforcement due to the high temperatures involved in liquid-state processing route [22].

2.6 Thermal Behaviour of Aluminium MMCs

The thermal cycling behaviour as well as the CTEs of aluminium MMCs and factors that affect them are presented in this subsection.

2.6.1 Thermal Cycling Behaviour of Aluminium MMCs

Materials undergo thermal fatigue when subjected to thermal excursion while in use. Typical applications where materials are subjected to thermal excursion are in internal combustion engines. Thermal fatigue could lead to catastrophic failure of materials, which, in turn, damages machine elements and could lead to loss of life in severe cases.

Temperature fluctuating environments are among the most severe conditions for MMCs. This is because the matrix deform plastically when the induced stress arising from the difference in the CTEs of the matrix and reinforcement is more than its yield strength. The thermal stress induced in a monotonic material and MMCs can be expressed mathematically as given in equations (2.1) [58] and (2.2) [55], respectively.

$$\sigma = \frac{\alpha E}{1-\nu} F(T) \tag{2.1}$$

$$\sigma = \Delta T \times \Delta\alpha \times E_m \tag{2.2}$$

where σ, α, ν, E and $F(T)$, ΔT, E_m and $\Delta\alpha$ are the thermal stress, CTE, Poisson's ratio and Young's modulus of the material, temperature dependence function,

temperature difference, Young's modulus of the matrix and the difference between the CTE of reinforcement and that of the matrix, respectively. It can be seen from equations (2.1) and (2.2) that the induced thermal stress not only depends on the CTE of the material, but also on the Young's modulus, Poisson's ratio and temperature distribution. Such a stress is difficult to determine as it is dependent on properties that vary with temperature. In view of this limitation, thermal strain-temperature curves of materials subjected to thermal cycling are used for analyzing their dimensional stability [58, 65-68].

Figure 2.2 shows a typical thermal strain-temperature curve of MMCs subjected to thermal cycling [43, 58, 65-68, 80]. Hysteresis loops induced in the MMCs are due to the stresses induced in them as they are cooled from the maximum cycling temperature [58, 65]. The strain parameters (i.e., residual plastic strain (ε_p), cyclic strain (ε_c), total strain (ε_T) and strain height ($\Delta\varepsilon$)) are shown in the figure. ε_p and $\Delta\varepsilon$ arise as a result of plastic deformation induced in the matrix when the thermal stress induced during thermal cycling exceeds its yield strength. The amount of hysteresis loop induced in a material can be evaluated based on the strain height, $\Delta\varepsilon$ [58]. According to the Wu *et al.* [58], $\Delta\varepsilon$ increases with hysteresis loop induced in a material. ε_c is the elastic strain induced in the matrix in each cycle, while ε_T is the sum of plastic and cyclic strain as shown in equation (2.3).

$$\varepsilon_T = \varepsilon_p + \varepsilon_c \tag{2.3}$$

Several thermal cycling studies have been conducted on Al MMCs because of the potential to use them in applications where stringent dimensional stability is required [58, 65-68]. From these studies, it has been found that ceramic reinforcements improve the dimensional stability of the matrix [43, 58, 65-68, 80]. Zhang *et al.* [65] reported that an appreciable amount of plastic deformation was induced in a hypereutectic Al-Si alloy as it is cycled between 20 and 400 ^{o}C at a rate of 5 ^{o}C/min. However, the induced plastic deformation decreased with the addition of SiC. A similar thermal cycling behaviour

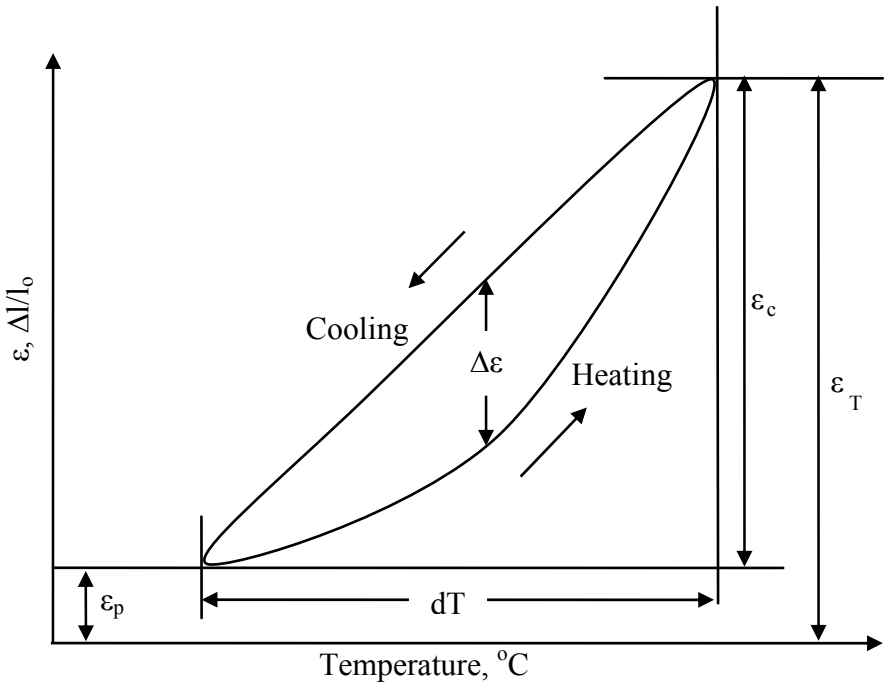

Figure 2.2. Typical thermal strain-temperature curve showing the formation of a hysteresis loop during thermal cycling.

was observed by Huang *et al.* [66] for aluminium alloy (KS1275®) MMCs reinforced with 20 vol.% Saffil®, Maftech®, Kaowool®, and Supertech® fibers and Tjong *et al*. [67] for Al-based MMCs reinforced with titania, alumina and boron particles. The authors in reference [67] attributed this thermal behaviour to the thermal stability of the reinforcement and improved reinforcement-matrix bond. Thermal cycling of MMCs has been reported to produce more plastic deformation in the initial few cycles than the subsequent cycles [65, 68]. Zhang *et al.* [65] attributed this behaviour to a partial relief of initial stresses in Al-Si alloy MMCs reinforced with SiC during previous cycles and work hardening effect induced by plastic deformation.

The extent of damage of MMCs due to thermal cycling depends on several factors. These include (i) the maximum temperature reached, (ii) heating and cooling rates, (iii) the rate of formation and propagation of microcracks and voids, (iv) fiber and particle fracture, (v) strength of the interfacial bonds, (vi) matrix microstructural transformation, (vii) matrix-reinforcement reactions, (viii) the mismatch in the CTEs of the matrix and

reinforcement, and (ix) tensile properties of the matrix. A review of the effect of these factors has been carried out by Baiden *et al.* [43].

2.6.2 The CTE of Aluminium MMCs

The Expansion of a material with increasing temperature is due to the asymmetric nature of the inter-atomic forces and the increase in the amplitude of vibration of atoms in the material with temperature [69]. Figure 2.3 shows a typical potential energy (U) curve of two atoms as a function of inter-atomic distance, r [69]. It can be seen that the potential energy curve is asymmetric in nature, with the potential energy curve broader in the $r > 0$ region. As potential energy increases with temperature, the atoms vibrate about their equilibrium position ($-U_o$ and r_o) thereby stretching and compressing the bonds. Also, the potential energy curve is broader in the $r > 0$ region, which makes the atomic bonds to stretch more than it compresses as temperature fluctuates. The cumulative stretching of the atomic bond gives rise to the phenomenon of thermal expansion and the fractional change in length of a material per degree rise in temperature is proportional to a thermal property of the material called the coefficient of thermal expansion (CTE). The average and true CTEs of materials are expressed in equations (2.4) and (2.5), respectively.

$$\lambda_n = \frac{1}{L_o}\frac{(L - L_o)}{(T - T_o)} \tag{2.4}$$

$$\lambda_T = \frac{1}{L_o}\frac{\delta L}{\delta T} \tag{2.5}$$

where λ_n, λ_T, L, L_o and $\frac{\delta L}{\delta T}$ represent the average CTE, true CTE, instantaneous length, original length, first derivative of final with respect to temperature, respectively. The CTE of MMCs has been extensively studied [34, 35, 37, 38, 55, 70-81, 86]. From these studies it is found that the CTE of MMCs is influenced by several factors such as (i) the reinforcement phase, and (iii) microcracks and microvoids. These make it difficult to predict accurately the CTEs of MMCs. A discussion of these factors is presented below.

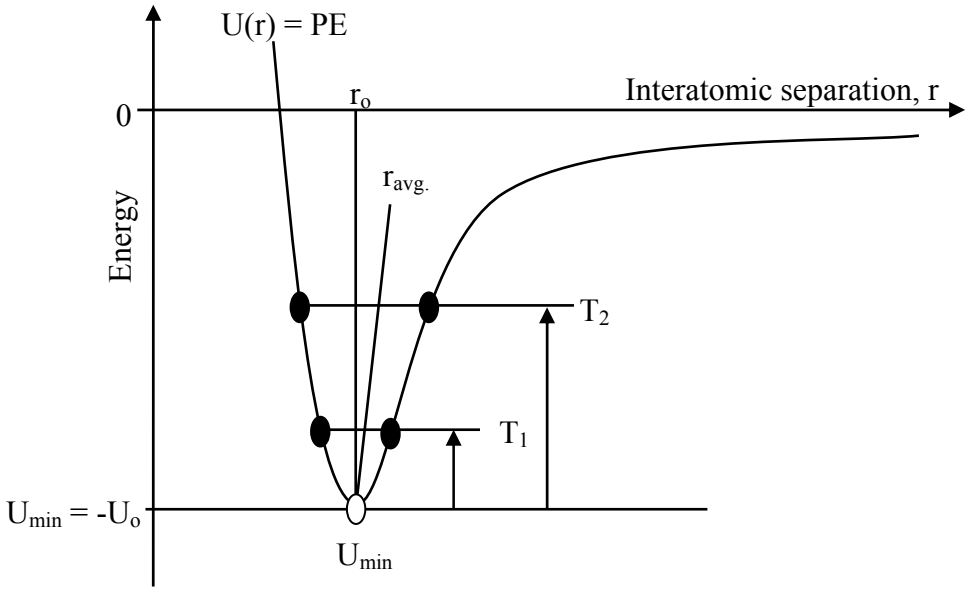

Figure 2.3. A schematic of the potential energy curve of two atoms separated by a distance, *r*.

2.7 Factors Affecting the CTE of Aluminium MMCs

This sub-section reviews some of the factors affecting the CTE of aluminium MMCs.

2.7.1 Effect of Service Temperature

Temperature fluctuation in aluminium alloy MMCs has been reported to alter their CTEs [35, 74, 80]. This affects the use of the composites where dimensional stability is a critical materials selection criterion. Lemiux *et al.* [35] showed that the CTE of A359-SiC and A360-SiC composites increased with temperature. A similar trend was also reported in reference [74] for pre-strained Al/Al_2O_3 MMCs. The authors in reference [74] attributed this to the thermal stress induced in the MMCs due to the difference in the CTE of the reinforcement and matrix material. This induced stress caused particle shattering and debonding, which promoted the deformation of the matrix plastically. Chen *et al.* [80] also reported that the CTE of aluminium MMCs reinforced with 50 wt.% SiC increased with temperature. It has also been found that during thermal cycling,

the CTE of composites increases rapidly initially and gradually approaches a saturation value due to the relaxation of the thermal stresses built up in the composite [22, 80].

2.7.2 Effect of the Nature of Reinforcements

The properties which MMCs exhibit throughout their work life depend on the nature of the reinforcement phase(s). Consequently, different reinforcements behave differently in the same metal matrix as a result of differences in their thermal, mechanical, and chemical properties [38, 55, 70]. Fei and Wang [38] reported that interfacial reaction affected the CTE of AA6061 MMC reinforced with *β*-eucryptite greatly. They attributed this to the interfacial strength, which allowed for the debonding of the reinforcement from the matrix at high temperatures, as well as the reduction in the amount of *β*-eucryptites in the composites due to their reaction with the matrix. Rohatgi *et al.* [55] showed that the CTE of A359 reinforced with 40 vol.% SiC was higher than when it was reinforced with 40 vol.% Al_2O_3. They attributed this difference to the CTE of SiC being higher than that of Al_2O_3. Sandanandam *et al*. [70] showed that at 50 ^oC, the CTE of aluminium alloy AA2124 composites reinforced with 20 vol.% SiC, Al_2O_3, and TiC were 18.6, 13.6 and 12.6 $\mu/^oC$, respectively.

2.7.3 Effect of the Volume Fraction and Size of Reinforcements

The CTE of aluminium alloy composites also decreases with increasing volume fraction [35, 37, 71] as well as decreasing size of the ceramic reinforcement [73, 86]. Park *et al.* [37] reported a decrease in the CTE of A390-SiC composites as the volume fraction of SiC increased and the size decreased. Lemieux *et al.* [35] observed a decrease in the CTE of Al-Si alloy MMCs with increasing weight percent of SiC. A similar trend was observed by Sharma [71] on the CTE of A6061 alloy composites reinforced with albite particles. In another study [73], it was reported that the CTE of aluminium MMCs reinforced with oxidized SiC particles increased with the size of the particles. These authors attributed this behaviour to the degree of oxidation of the ceramic particles,

which was greater in small sized particles than in the large ones. A similar trend was observed by Xu *et al.* [86] for aluminium MMCs reinforced with TiC.

2.7.4 Effect of the Microcracks and Microvoids

The CTE of MMCs has also been reported to be affected by the presence of microcracks [75] and microvoids [74-76]. Elomari *et al*. [74] reported an increase in CTE of pre-strained A6061-Al_2O_3 composites with increasing fraction of broken particles. They attributed this to lattice distortion associated with the pre-staining, which led to the formation and propagation of microcracks that stimulated plastic deformation of the matrix. Zhao *et al.* [75] reported that the CTE of aluminium MMCs reinforced with SiC foam was lower than that reinforced with discrete SiC discrete particles. They attributed this to the presence of micropores in the MMCs reinforced with SiC foam, which allowed the matrix to expand into the pores freely as temperature increased thereby reducing the increase of their bulk volume. Balch *et al.* [76] also reported the closure of voids in Al-SiC foam-reinforced MMC as it is cycled between room temperature and 330 ^{o}C. They attributed this to local matrix plastic deformation driven by high thermal stress at sites where voids existed.

2.8 Models for Prediction of CTE of MMCs

The CTE of MMCs is difficult to predict due to the effect of the several factors discussed in the preceding sections. However, several theoretical models have been reported in the literature for predicting it [22, 77-79]. Amongst these, the Rule of Mixtures [22] and the models proposed by Turner [78], Kerner [79] and Schapery [77] are the most used and will be discussed further below.

2.8.1 Rule of Mixtures

The Rule of Mixtures (ROM) model as applied to CTE evaluation is a mathematical expression that relates the CTE of MMCs to the CTEs and volume fractions of the reinforcement(s) and metal matrix. ROM is based on a number of assumptions such as (i) uniform, parallel and continuous reinforcement(s), (ii) perfect bonding between the reinforcement(s) and the matrix, and (iii) the matrix and reinforcement being equally strained when loaded. The ROM model is expressed mathematically as [22]:

$$\alpha_c = \alpha_m V_m + \alpha_r V_r \tag{2.6}$$

where α is the CTE, V is the volume fraction, and the subscripts c, m and r refer to the composite, metal matrix and reinforcement, respectively. It is a simplified method of determining the CTE and other properties of MMCs and does not consider such factors as the nature of the reinforcement and stress distribution in composites that affect their properties [22]. However, Balch *et al.* [76] reported for a thermal cycling study that the average CTE of aluminium MMC reinforced with SiC (in the form of crushed foam) in the second cycle is approximately the same as that predicted by the ROM in the first.

2.8.2 Turner's Model

Turner [78] derived the CTE of composites by making the following assumptions: (i) homogeneous distribution of reinforcement material, (ii) homogeneous strain throughout the composite, (iii) each constituent of the composite changes dimensions with temperature at the same rate as the composite, and (iv) shear deformation is negligible. The model is expressed as:

$$\alpha_c = \frac{\alpha_r V_r K_r + \alpha_m V_m K_m}{V_r K_r + V_m K_m} \tag{2.7}$$

where K, V, and α are bulk modulus, volume fraction and CTE, and the subscripts c, m and r refer to the composite, metal matrix and reinforcement, respectively. Baldi *et al.* [76] reported that the average CTEs of aluminium MMCs reinforced with SiC foam and SiC particle below 150 ^{o}C was in good agreement with those predicted by Turner's model.

2.8.3 Kerner's Model

Another model used for predicting the CTE of MMCs is the Kerner's model [79]. It assumes that: (i) the composite is made up of spherically shaped reinforcement, (ii) the reinforcement is wetted by a uniform layer of matrix, and (iii) there is perfect mechanical bonding between the matrix and the particle. The Kerner's model is expressed as:

$$\alpha_c = \overline{\alpha} + V_r * (1 - V_r) * (\alpha_r - \alpha_m) * \left[\frac{K_r - K_m}{(1 - V_r)K_m + V_r K_r + (3K_r K_m / 4G_m)} \right] \tag{2.8}$$

where $\overline{\alpha}$ is the CTE calculated using the ROM model, K is the bulk modulus, G is the shear modulus, V is the volume fraction, α is the CTE, and the subscripts c, m and r refer to the composite, metal matrix and reinforcement, respectively. The bulk, Young's (E) and shear moduli are interrelated as shown in equation (2.9).

$$K = \frac{E}{3\left(3 - \frac{E}{G}\right)} \tag{2.9}$$

Lemieux *et al.* [35] reported that the Kerner's model predicted the CTE of A359-SiC and A360-SiC composites at high temperatures fairly well. On the other hand, another study showed that the model could not predict the CTE of pre-strained aluminium MMCs reinforced with alumina [81]. The authors attributed this to the complex stress

transfer mechanisms between the matrix and the particle during pre-straining which Kerner's model did not consider.

2.8.4 Schapery's Model

Schapery derived the CTE of isotropic and anisotropic composites with isotropic phase using the extremum principles of thermoelasticity [77]. The model relates the CTE of composites to the overall bulk modulus of the composite and the bulk moduli of the matrix and the reinforcement. The upper and lower bounds of Schapery's model are expressed respectively in equations (2.10) and (2.11).

$$\alpha_c = V_r\alpha_r + V_m\alpha_m + \left[\frac{4G_m}{K_c}\right]\left[\frac{(K_c - K_r)(\alpha_m - \alpha_r)V_r}{4G_m + 3K_r}\right] \tag{2.10}$$

$$\alpha_c = V_r\alpha_r + V_m\alpha_m + \left[\frac{4G_r}{K_c}\right]\left[\frac{(K_c - K_m)(\alpha_r - \alpha_m)V_m}{4G_r + 3K_m}\right] \tag{2.11}$$

where K, V, G and α are bulk modulus, volume fraction, shear modulus and CTE, respectively, and the subscripts c, m and r refer to the composite, metal matrix and reinforcement, respectively. K_c is obtained from the Hashin-Shtrikman analytical model [83] which is given in equations (2.12) and (2.13).

$$K_c^{upper} = K_r + \left[\frac{V_m}{\frac{1}{K_m - K_r} + \frac{V_r}{K_r + 4\frac{G_r}{3}}}\right] \tag{2.12}$$

$$K_c^{lower} = K_m + \left[\frac{V_r}{\frac{1}{K_r - K_m} + \frac{V_m}{K_m + 4\frac{G_m}{3}}}\right] \tag{2.13}$$

Elomari *et al.* [74] reported that Sharpery's model predicted the CTE of pre-strained aluminium MMCs reinforced with alumina. They used the experimental bulk modulus to compute the CTE, thereby eliminating the effect of pre-strain. Similarly, Elomari and Llyods [72] showed that the CTE of aluminium alloy AA6061 reinforced with 10, 20 and 40 vol.% Al_2O_3 fell within the upper and lower elastic bounds derived by Schapery.

2.9 Reactions in Aluminium MMCs

In synthesizing aluminium MMCs via solid-state or liquid-state processes, they are exposed to high temperatures. At these high temperatures, there is a thermodynamic tendency for reactions to occur between the matrix and the reinforcement, forming reaction products with properties that differ from those of the matrix and the reinforcement. These reaction products affect the microstructure and, hence, the properties of the MMCs [13, 16, 25-33].

Typical reactions that can occur in aluminium MMCs and their corresponding Gibbs free energy [84] are shown in equations (2.14)–(2.23). The reactions that occur in a given aluminium MMC depend on the chemical constituents of the matrix and the reinforcement(s), the amount of heat input, the length of time spent at elevated temperatures, and the cooling rate during fabrication [22]. Hence, it is a difficult exercise to design a method for controlling reactions in aluminium MMCs.

$3Mg_{(l)} + 4Al_2O_{3(s)} \leftrightarrow 3MgAl_2O_{4(s)} + 2Al_{(l)}$ (ΔG = -178.8 kJ/kg at 1000 K) (2.14)

$2SiO_{2(s)} + 2Al_{(l)} + Mg_{(l)} \leftrightarrow MgAl_2O_{4(s)} + 2Si_{(s)}$ (ΔG = -36.4 kJ/kg at 1000 K) (2.15)

$3Mg_{(l)} + 4Al_2O_{3(s)} \leftrightarrow 2Al_{(l)} + 3MgAl_2O_{4(s)}$ (ΔG = -161.8 kJ/kg at 1000 K) (2.16)

$4Al_{(l)} + 3SiO_{2(s)} \leftrightarrow 3Si_{(s)} + 2Al_2O_{3(s)}$ (ΔG = 86.7 kJ/kg at 1000 K) (2.17)

$2Mg_{(l)} + SiO_{2(s)} \leftrightarrow Si_{(s)} + 2MgO_{(s)}$ (ΔG = -96.6 kJ/kg at 1000 K) (2.18)

$Si_{(s)} + 2Mg_{(l)} \leftrightarrow Mg_2Si_{(s)}$ (ΔG = -89.9 kJ/kg at 1000 K) (2.19)

$4Al_{(l)} + 3SiC_{(s)} \leftrightarrow Al_4C_{3(s)} + 3Si_{(s)}$ (ΔG = -51.2 kJ/kg at 1000 K) (2.20)

$2Al_{(l)} + Si_{(s)} + 5/2O_{2(g)} \leftrightarrow Al_2SiO_{5(s)}$ (ΔG = -1138.7 kJ/kg at 1000 K) (2.21)

$2Al_{(l)} + Fe_2O_{3(s)} \leftrightarrow 2Fe_{(s)} + Al_2O_{3(s)}$ (ΔG = -153.6 kJ/kg at 1000 K) (2.22)

$$3Mg_{(l)} + Fe_2O_{3(s)} \leftrightarrow 3MgO_{(s)} + 2Fe_{(s)} \qquad (\Delta G = -296.3 \text{ kJ/kg at } 1000 \text{ K}) \qquad (2.23)$$

Lloyd [28] reported that alumina is unstable in a magnesium-containing aluminium alloy systems because it reacts with magnesium to form either spinel ($MgAl_2O_4$) or magnesium oxide (MgO), depending on the magnesium content of the alloy. The presence of spinel in aluminium alloy MMCs has been reported in AA2618 MMCs reinforced with alumina [33], Al-1 wt.% Mg MMCs reinforced with alumina [26], A535 alloy MMCs reinforced with fly ash [39], Al–7 wt.% Si–0.35 wt.% Mg alloy MMCs reinforced with fly ash [64], and AA6061 alloy reinforced with alumina [85]. The aforementioned authors attributed the formation of spinel to chemical reactions between the metal matrix and the reinforcement.

The presence of magnesium disilicide (Mg_2Si) in magnesium-containing aluminium alloy MMC has been reported by several researchers [16, 25, 87,88]. It was identified in a Al-5 wt.% Mg composite reinforced with SiC [90], Al-2 wt.% Mg alloy reinforced with SiC [87], and A535 reinforced with fly ash [25]. According to [25], Mg_2Si formed from the reaction between solid solution magnesium atoms and excess silicon injected into the matrix by reduction reactions involving SiO_2 in fly ash. The formation of Mg_2Si in A535 MMCs depleted solid solution magnesium atoms thereby decreasing their mechanical strength.

The presence of Al_3C_4 phase in aluminium MMCs reinforced with graphite and SiC has been reported [88-90]. It was also identified in aluminium alloy A359 reinforced with SiC [89]. It occurred at the interface between Al matrix and graphite fiber reinforcement in reference [90] and was attributed to a chemical reaction between aluminium and SiC.
Reactions in MMCs can be controlled by coating the reinforcement, choosing appropriate fabrication technique, or by altering the volume fraction, size and distribution of the reinforcement phase. Coating is the most recommended method of controlling interfacial reactions in MMCs because of the low process cost, uniform distribution of the material coated around reinforcement and the wide varieties of coating materials with different properties that can be achieved by altering the

composition of the coating-solution [22, 88, 91]. Yang *et al.* [88] used a thin film of SnO_2 coating to reduce the amount of interfacial reaction between aluminium and SiC in an aluminium-SiC composite. Gao *et al.* [91] coated alborate whiskers with copper using an electroless plating method in order to improve their chemical stability in magnesium-containing aluminium alloy-matrix. They observed a reduction in whisker degradation, which resulted in an enhance tensile strength of the composites.

2.10 Experimental Techniques for Thermal Analysis and XAS Study of Aluminium MMCs

Reactions that occur in particulate aluminium MMCs have been investigated using various materials characterization techniques such as optical microscopy [16, 49, 92], Transmission Electron Microcopy (TEM) [40, 41, 85], Thermal Analysis [44, 46, 47], Scanning Electron Microscopy (SEM) [40, 42, 43, 45], Energy Dispersive X-ray Spectroscopy (EDS) [13, 40, 41, 45], X-ray Diffractometry (XRD) [39, 43, 49, 94] and X-ray Absorption spectroscopy (XAS). A brief discussion of these techniques follows.

2.10.1 Optical Microscopy

Optical microscopy (OM) uses the combined effects of visible light and a system of lenses to study the microstructure of materials. It has been used extensively to study reactivity in MMCs [16, 48, 92]. Towle *et al.* [48] used it to identify globular or blocky shaped intermetallic phases in AA6061-safill MMCs, which were not present in the matrix. Ren *et al.* [92] used it in combination with XRD to identify the presence of Al_4C_3 in Al-SiC composites. However, the resolution power of OM limits its use for identifying very fine reaction products in materials. To overcome this limitation, electron microscopes with higher resolution than OM are used.

2.10.2 Electron Microscopy

Electron microscopy (EM) is used for examining microstructures of materials at a much higher resolution than OM. It can be used for both qualitative and quantitative analysis of reaction products formed in MMCs if equipped with EDS capability. SEM was used to verify the presence of spinel around alumina particles in AA6061-alumina composites [42]. Mei *et al.* [45] also used SEM equipped with an EDS capability to identify Al_2O_3 and $FeAl_2O_4$ as reaction products that formed in Al-iron oxide thermite reaction. A TEM equipped with an EDS system was used to identify the presence of Si-rich alumosilicate phases at the interface between aluminium and constituent oxides of fly ash in Al-fly ash composites [41]. It was also used to identify the presence of interfacial reaction products such as AlB_2, AlN, $MgAl_2O_4$, $Al_3B_{48}C_2$ in Al-Mg alloy AA5052 composites reinforced with B_4C [40].

2.10.3 X-ray Diffractometry

X-ray Diffractometry (XRD) is commonly used to identify phases in materials by comparing their diffraction patterns with those from known reference phases or materials. It was used to identify the presence of reaction products such as Mg_2Si, Al_4C_3 and $MgAl_2O_4$ in Al-Cu-Mg alloy AA2009 MMCs reinforced with SiC whiskers [48]. Lee *et al.* [93] reported the presence of $MgAl_2O_4$ in AA6061 reinforced with alumina particles using XRD. Also, it was used to determine that the amount of solid solution magnesium depleted in Al-Mg alloy A535 due to the addition of fly ash [39].

2.10.4 Thermal Analysis

Thermal analysis comprises a group of techniques such as Thermomechanical Analysis (TMA), Differential Thermal Analysis (DTA) and Differential Scanning Calorimetry (DSC), which measures a physical property of a sample as a function of temperature and time. Figure 2.4 shows a typical DSC thermogram of a material. Exothermic and endothermic processes give rise to concave and convex shaped peaks, respectively. DSC

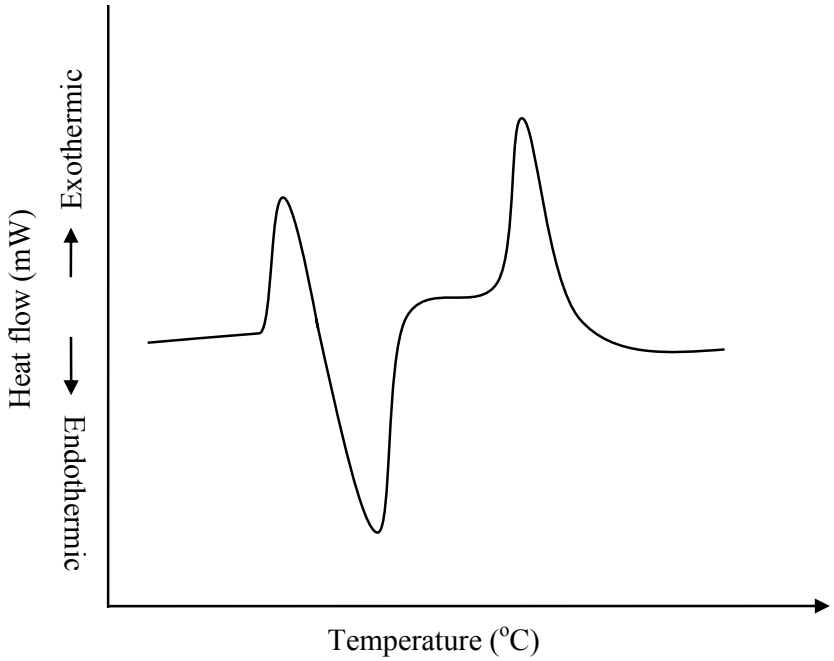

Figure 2.4. A typical DSC thermogram.

thermograms are fingerprints of materials and are used for determining their melting, glass transition and crystallization temperatures, phase diagrams, heat capacities, and enthalpies of reactions.

Thermal analysis techniques have been used extensively in studying phase transformations and reactions in MMCs [44-47]. DTA was used to study the stability of aluminium-fly ash composites between 450 and 700 ^{o}C [44] and it was found that the oxides of iron and silicon oxide in fly ash were reduced to iron and silicon, respectively, by the aluminium matrix. DTA was also used to study reactivity in Fe_2O_3-Al system [45] and it was found that a two-stage reaction occurred at 960 ^{o}C, forming Al_2O_3 and Fe_3O_4, and at 1060 ^{o}C, forming Al_2O_3 and $FeAl_2O_4$. It was used to study reactivity in Al-9 wt.% Cu MMCs reinforced with aluminium borate ($Al_{18}B_40_{33}$) whiskers [46]. The authors reported an exothermal peak at 762.5 °C during the first scan due to the formation of alumina, which did not appear when the sample was rescanned through the same temperature range. Shabestari *et al.* [47] used thermal analysis method to investigate pre- and post-eutectic reactions that occur in A319 aluminium alloy. They reported a

pre-eutectic reaction at 600 ^{o}C and a post-eutectic reaction at 544.9 ^{o}C that led to the formation of the Chinese script-like $Al_{15}(Fe,Mn)_3Si_2$ and $Al_8Mg_3FeSi_6$ phases. TMA has been used extensively for studying thermal cycling behaviour of aluminium MMCs as well as for determining their CTEs and the variation of CTE with such factors as temperature [35, 74], microcracks and microvoids [74-76], and nature [38, 55, 70], size and volume fraction of the reinforcement [35, 37, 71-73]. The environments in which these materials are subjected to during measurement depend on their potential applications. The environmental conditions include constant or fluctuating temperatures as well as inert, oxidizing or humidifying.

2.10.5 X-ray Absorption Spectroscopy

X-ray Absorption Spectroscopy (XAS) probes local structures of an element in a sample. It uses a synchrotron radiation facility or an X-ray tube which generates the required monochromatic X-ray beam. Nevertheless, a synchrotron radiation is used more often than X-ray tube facilities because of the bright, intense and monochromatic X-ray beam it generates.

Figure 2.5 shows a schematic diagram of typical electron-transitions that occur when an X-ray beam is incident on a material and a typical XAS spectrum [94]. In Figure 2.5(a), electrons in the material are excited to an unoccupied state or to the continuum when an X-ray beam with energy (*hv*) more than the binding energy of the electrons is incident on it. This creates instability in the electronic structure of the material which nature abhors. In order for the electronic structure to attain its original stable state, an electron drops from a high energy orbital to fill the core hole created, thereby emitting fluorescence X-rays or auger electron(s).

Figure 2.5(b) shows a typical XAS spectrum, showing the different levels of atomic interactions that occur as X-ray beam probes a material system. XAS spectra are used to identify chemical species, and are also sensitive to changes in chemical species in materials. XAS spectra of standard reference materials can be used to identify chemical

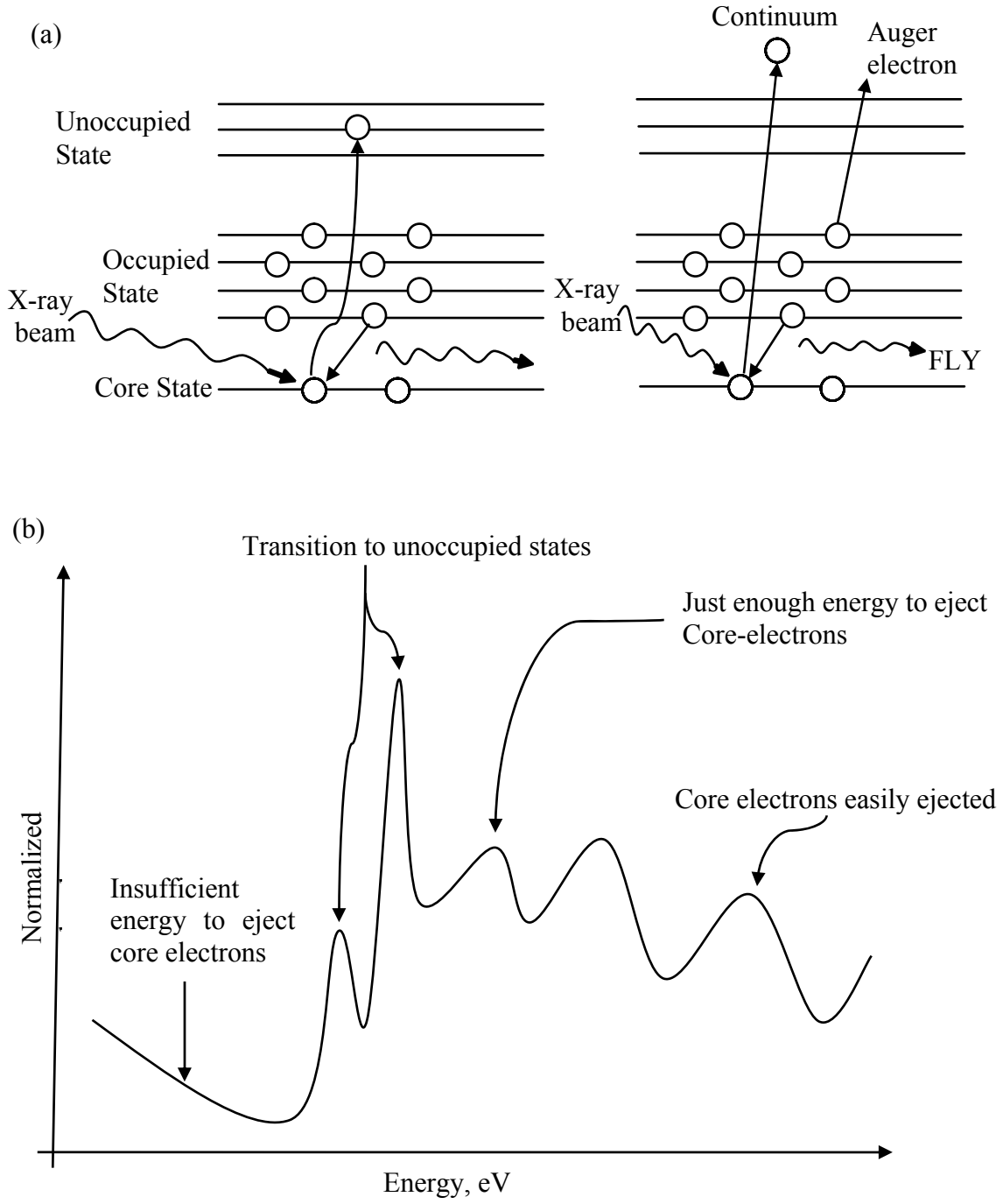

Figure 2.5. A schematic diagram of: (a) the electron-transitions that occur when an X-ray beam is incident on a material and (b) XAS spectrum [94].

species present in a material through peak matching. The S and Ca K-edges XAS of cementitious coal combustion by-products (CCBs) were used to determine various forms

of S and Ca minerals present in it [51]. Local structural information on the coordination number and bond lengths of elements in materials can also be obtained from XAS spectrum by monitoring the Extended X-ray Fine Structure (EXAFS) oscillations due to constructive and destructive wave interferences as core-hole electrons excite to the continuum in a material-system. EXAFS was used to verify the amorphous nature of electrodeposited Cr-P alloy [50]. Near-edge X-ray absorption fine structure (NEXAFS) was used also to identify tetrahedral, octahedral and square planer geometries of Al in zeolites [97].

XAS have been used to investigate the electronic structure of materials [98, 99]. It is sensitive to the number of unoccupied states in materials and, as such, can be used to investigate charge transfer mechanism between elements in a materials system. Figure 2.6 shows a schematic representation of the charge transfer mechanism between orbitals in elements *A* and *B* in a materials system. As can be seen, it involves the transfer of charges (electrons) from orbitals in both elements in such a way that the net charge in them is zero. The mechanism of charge transfer between elements in a material system can be investigated by probing the population of electrons in all the orbitals in the elements that make-up the material system. Lalvani *et al.* [98] observed charge transfer from Ni to phosphorous *p*-orbitals in electrodeposited Ni-P coat using XAS. It was also used in reference [99] to observe the depletion of *d* charge in Au upon alloying with Ag, which was accompanied by a compensating charge flow of *s* charge onto Au sites.

XAS is a surface and bulk sensitive technique. It can be used to investigate chemical speciation and local elemental structure in materials at different depths. Zou *et al.* [95] used it to observe that the thickness of the surface oxide on pure Al samples increased with annealing temperature. They also reported that about 320 Å of the Al layer underneath the oxide remained metallic in the sample annealed at 600 ^{o}C. This is an indication that the sampling depth of Al K-edge FLY is about 320 Å. Similarly, Kasrai *et al.* [96] observed that the Si L-edge TEY and FLY have sampling depths of about 5 nm and 70 nm, respectively.

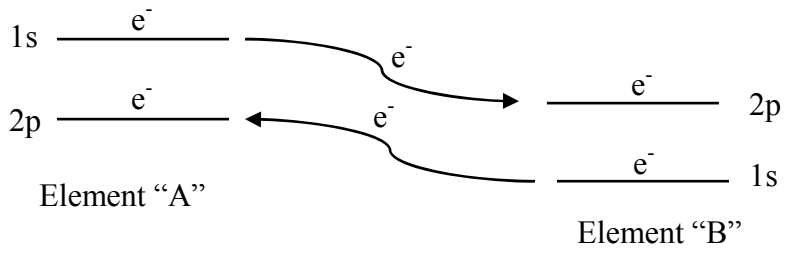

Figure 2.6. Charge compensation mechanism between two elements in a material system.

3.0 MATERIALS AND EXPERIMENTAL METHODS

The materials and experimental methods used in this study are discussed in this chapter. Also, the problems encountered and methods used to solve them are presented.

3.1 Materials

Two aluminium alloy systems and their particulate MMCs were studied in this work, namely: (i) Al-Cu-Mg alloy AA2618 and its composites reinforced with 10 and 15 vol.% alumina (Al_2O_3) particles (AA2618+10 and AA2618+15, respectively) and (ii) Al-Mg alloy A535 and its composites reinforced with a mixture of 5 wt.% fly ash and 5 wt.% silicon carbide (A535/Hybrid/10_p), 10 wt.% fly ash (A535/Fly ash/10_p), and 15 wt.% fly ash (A535/Fly ash/15_p). AA2618 and its composites were manufactured by a proprietary casting route, followed by extrusion, while A535 and its composites were fabricated using a proprietary stir casting technique. The industrial fly ash used as a reinforcement material in the A535 MMCs was obtained from a coal-based thermal plant in Ontario, Canada. High-purity aluminium (Al), magnesium (Mg), magnesium oxide (MgO), alumina (α-Al_2O_3), spinel ($MgAl_2O_4$), iron II oxide (Fe_2O_3), and iron III oxide (Fe_3O_4) powders purchased from Alfa Aesar®, Massacheusset, USA, as well as the industrial fly ash were used as reference materials. The chemical compositions of AA2618 and its composites as supplied by the manufacturers are shown in Table 3.1, while those of A535 and fly ash are shown in Tables 3.2 and 3.3, respectively [16].

Table 3.1. Chemical compositions of AA2618 and its MMCs.

Materials	Elements									
	Si	Fe	Cu	Mn	Mg	Cr	Ni	Zn	Ti	Al_2O_3
AA2618	0.18	1.19	2.34	---	1.59	---	1.05	---	0.07	---
AA2618+10	0.17	1.15	2.15	0.01	1.69	0.002	1.08	0.02	0.07	9.3*
AA2618+15	0.18	1.09	2.11	0.01	1.53	0.004	1.04	0.02	0.07	15.7*

* Composition in vol.%. Balance = Al. AA2618+10 = AA2618/Al_2O_3/10_p composite; and AA2618+15 = AA2618/Al_2O_3/15_p composite.

Table 3.2. Chemical composition of A535 [16].

Element	Mg	Cu	Si	Fe	Ti	Al
Wt.%	6.17	0.01	0.01	0.02	0.04	Bal.

Table 3.3. Chemical composition of fly ash [16].

Element	SiO_2	Al_2O_3	Fe_2O_3	MgO	CaO	TiO_2	K_2O	Na_2O	SO_3
Wt.%	44.8	22.2	24.0	0.9	1.8	0.8	2.4	0.9	0.04

Balance = oxides of other trace elements.

3.2 Sample Preparation

The methods used in preparing samples used for the experiments conducted in this work are documented in the following sub-section.

3.2.1 Optical Microscopy and Scanning Electron Microscopy

The samples used for Optical Microscopy (OM) and Scanning Electron Microscopy (SEM) were rectangular coupons (measuring 5 x 5 x 2 mm) cut from the as-received materials using high precision diamond cutting tool (IMPTECH EUROPE Precision Cutter). They were encased in an epoxy mould and polished to a high degree of smoothness using several grades of emery papers and 1 μm diamond paste. They were subsequently rinsed in distilled water and methanol, and dried.

3.2.2 X-ray Absorption Spectroscopy

Samples of the test materials used for X-ray Absorption Spectroscopy (XAS) measurements were similar in size to those used for OM and SEM. The samples of AA2618 and its MMCs were solution heat treated at 530 ± 5 ^{o}C for 2 h, water quenched, polished using emery cloths, rinsed in methanol and distilled water, and then overaged at 200 ^{o}C for 7 days (168 h), while those of A535 and its MMCs were studied in the as-cast condition. In order to optimize the use of XAS for investigating the reaction products formed in the MMCs of AA2618 and A535, Aqua Regia was used to extract alumina and fly ash particles from the composites, respectively. The Aqua Regia used was prepared by mixing 1 part concentrated HNO_3, 3 parts concentrated HCl and 1 part distilled water under a fumehood. The extracted particles were thoroughly rinsed with distilled water and methanol before drying in air. The dry extracts are designated "Extracted alumina" and "Extracted fly ash" in this work.

3.2.3 Differential Scanning Calorimetry

The samples used for Differential Scanning Calorimetry (DSC) measurements were A535, fly ash-A535 MMCs and some of the reference materials. The A535 and MMC samples were studied in the as-cast condition. The weight of all DSC samples was kept between 90 and 95 mg. The samples and the alumina crucibles used as sample and reference containers in all the DSC experiments were sonicated in methanol to remove contaminants and dried in air afterwards. To simulate the alloy and the composites, mixtures of aluminium, magnesium and fly ash were prepared by mechanically mixing various proportions of these materials using mortar and pestol. A binary Al-Mg alloy with a Mg content close to that of A535 alloy was simulated by mixing 446.5 mg of pure Al with 28.5 mg of pure Mg. For the composites, A535/Fly ash/10_p was simulated by mixing the 374 mg binary Al-Mg alloy with 37.4 mg of fly ash.

3.2.4 Thermomechanical Analysis

The test samples used for thermomechanical analysis were cut from the as-cast stocks of A535 and its MMCs and machined to a size of 10 x 8 x 8 mm. A typical sample is shown in Figure 3.1. The ends of the samples were machined parallel and flat to an accuracy of ±25 μm in accordance with the ASTM E831 (2003) standard.

3.3 Experimental Procedure

3.3.1 Optical Microscopy

Optical microscopy was used to provide basic information about the microstructure of the samples. The polished samples were imaged using either a Nikon Optiphot^{TM} upright microscope equipped with a Paxcam 3^{TM} CCD camera, manufactured in Illinois, USA, that was interfaced with Pax-it^{TM} image analysis software or a Zeiss Axiovert 25^{TM} inverted microscope powered by Clemex Vision (version 3.0.037) data acquisition and analysis software.

3.3.2 Scanning Electron Microscopy

The microstructure and the chemical compositions of the phases present in the test samples were studied using a JOEL JSM 5900LV Scanning Electron Microscope equipped with an Oxford INCA^{TM} Energy Dispersive Spectroscopy (EDS) system. The polished samples were firmly held on the sample holder using a double-sided carbon tape before putting them inside the sample chamber. The SEM was operated at an accelerating voltage of 5 to 20 kV.

3.3.3 X-ray Diffractometry

The extracted alumina and fly ash were investigated to identify and quantify the reaction products in them using X-ray diffraction (XRD) technique. The same sample preparation

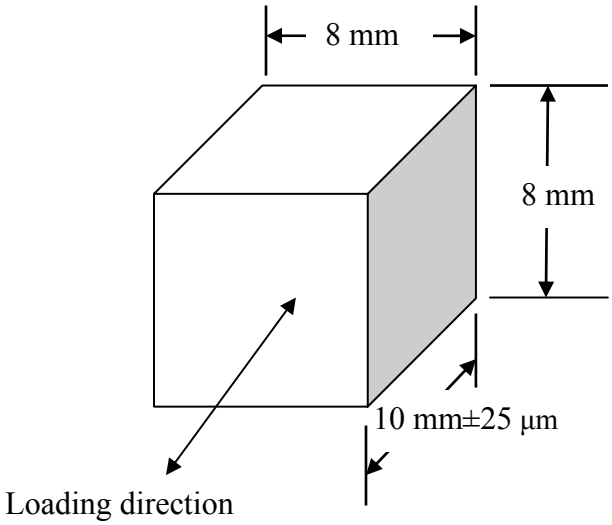

Figure 3.1. A typical sample used for thermomechanical analysis.

method that was used in extracting fly ash for the XAS measurements was used in preparing the samples used in this experiment. The sample were prepared in Diffraction data were collected with a Bruker D8 θ-θ X-ray diffractometer equipped with CoK_{α} monochromating multilayered mirrors on the incident and beam sides. A Rietveld refinement software, TOPAS^{TM}, was used for quantitative analysis.

3.3.4 X-ray Absorption Spectroscopy Measurements

XAS measurements were used to study reactivity and charge transfer in the test materials. The polished metal coupons, extracted alumina, extracted fly ash, and the reference powders were used for this study. The samples were mounted firmly on the sample holder using a double-sided graphite tape. In order to save the time spent in carrying out XAS measurements at the synchrotron beamlines, at least two bulk samples were mounted on the sample holder using a graphite tape supplied by the Canadian Light Source. After mounting, they were transferred into the vacuum chambers of the beamlines and analyzed.

XAS measurements at the Al, Mg and Si K-edges were conducted on the Spherical Grating Monochromator (SGM) beamline [100], while those of Al L-edges were on the Variable Line Spacing Plane Grating Monochromator (VLS-PGM) beamline [101] at the Canadian Light Source (CLS), Saskatoon. The ranges of the photon energies for the XAS measurements are summarized in Table 3.4. Sufficient pre-edge data was obtained for all the XAS measurements to aid pre-edge background subtraction. In all the XAS measurements, the step size was maintained at 0.1 eV and the entrance and exit slits were set at 50 x 50 μm to ensure consistency.

A monochromatic X-ray beam with the appropriate energy was incident on the samples to generate characteristic X-rays and total electron yield. The Al K- and L-edge and Si K-edge data were acquired in the Total Electron Yield (TEY) and Fluorescence Yield (FLY) modes. The maximum sampling depth of Si K-edge TEY is about 5 nm and the FLY is in several hundred nm [96]. The sampling depth of Al K-edge TEY is about 32 nm [95], while that of the FLY has not been reported in the open literature. The use of both acquisition modes (TEY and FLY) allowed probing of different regions in the test materials preferentially. TEY is surface and sub-surface sensitive, while the FLY is both bulk and surface sensitive. The Fe K-edge was not investigated because its energy is outside the SGM energy range. Data from different spots on the test samples were collected to ensure representative results.

The WINXAS^{TM} version 2.0 software was used for normalizing the XAS data as well as for pre-edge background subtraction. The normalization and pre-edge background subtraction were done using two-polynomial-fit (second order polynomial) between the energies of interest in the spectra. Figure 3.2(a) shows a typical example of the use of two-polynomial-fit in WINXAS^{TM} for pre-edge background subtraction, while Figure 3.2 (b) shows that of post-edge normalization. The Al and Si K-edge TEY and FLY data of the samples were calibrated using the energy positions of those of Al_2O_3 and those of SiO_2 as reported in references [95] and [96], respectively. The areas under peaks of interest were calculated using PeakFit^{TM} software. Figure 3.3 shows a typical case where the PeakFitTM software was used for assigning peak positions.

Table 3.4. Energy ranges used for XAS measurements.

Elements	Edge	Start energy, E_o (eV)	Stop energy, E (eV)
Aluminium	K	1545	1620
	L	70	90
Magnesium	K	1295	1350
Silicon	K	1910	1842

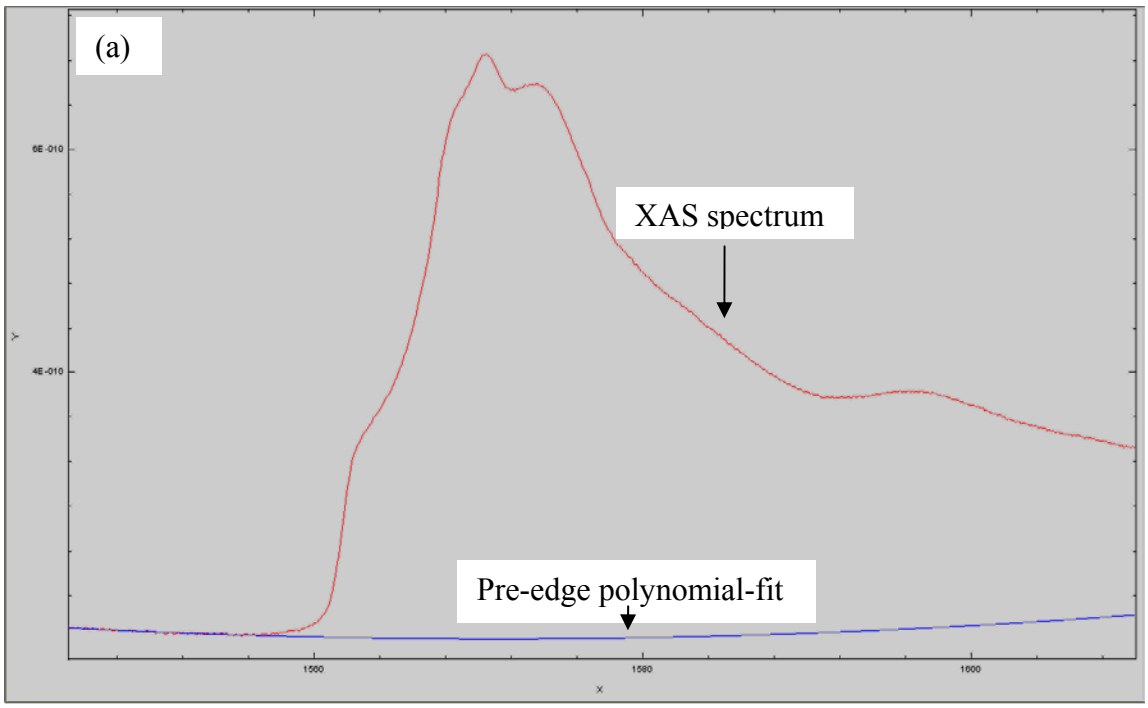

Figure 3.2. Use of two-polynomial-fit in WINXAS^{TM} for (a) pre-edge background subtraction and (b) normalization.

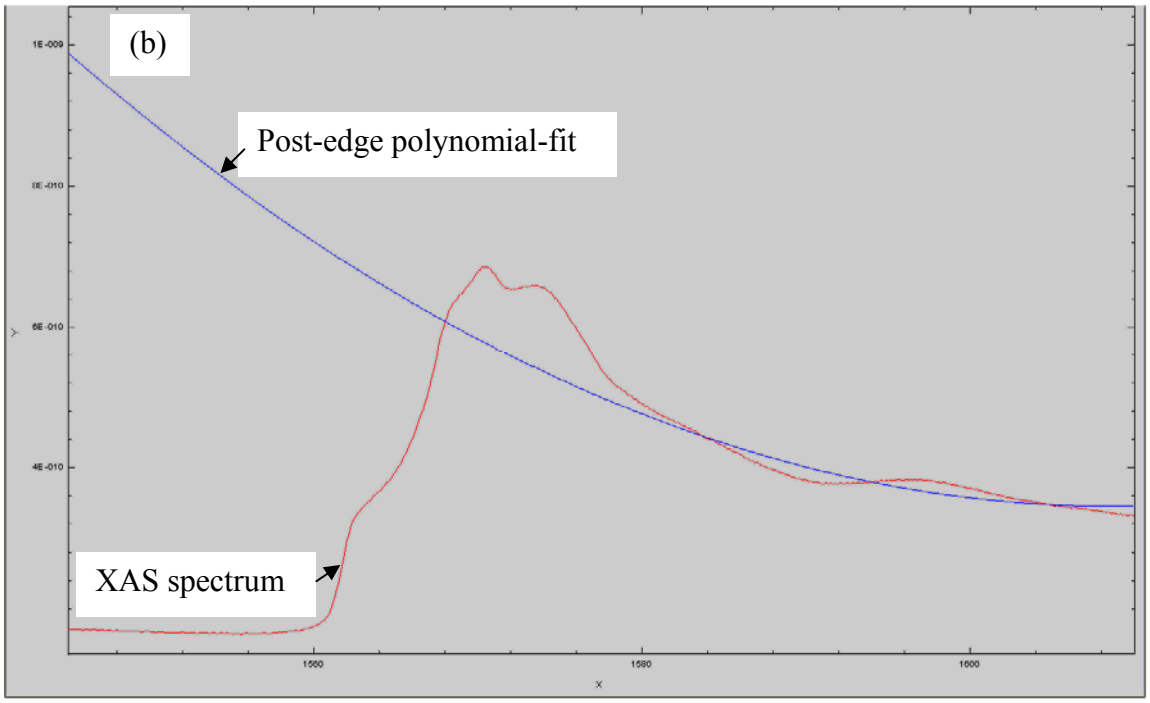

Figure 3.2 continues.

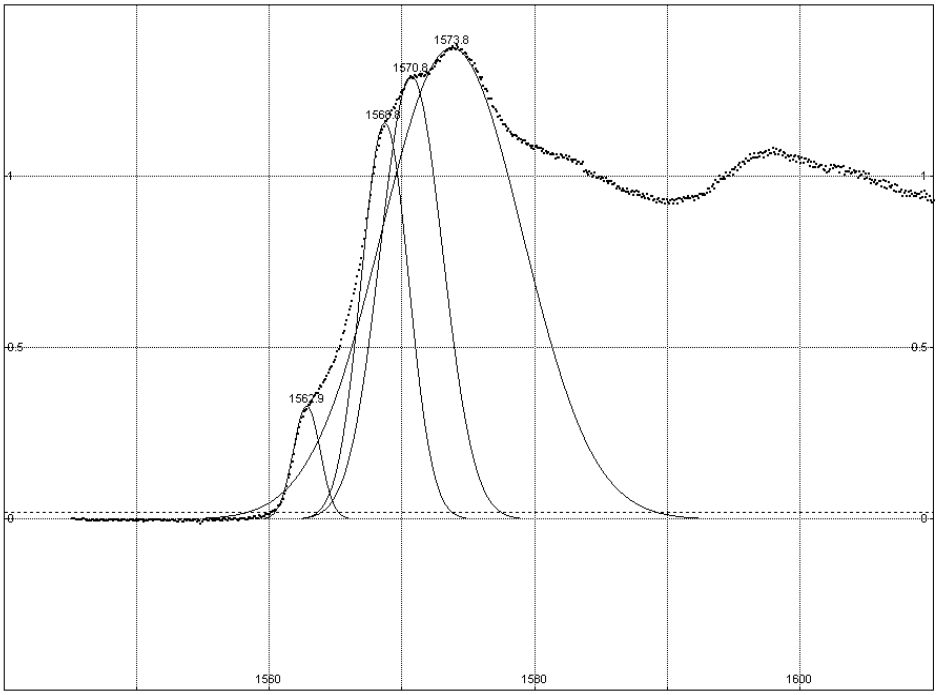

Figure 3.3. Assignment of peak positions using PeakFit^{TM}.

3.3.5 Differential Scanning Calorimetry

DSC was used to investigate reactivity in A535 and its MMCs. A Seteram TG-DSC 11, manufactured in France, interfaced with a SETSOFT 2000 software was used in this work. All the samples and crucibles used were weighed using an electronic balance (Schimadzu Corporation, Model AUW120D). The sample weight was determined using the mathematical expression given in equation (3.1).

$$m = m_1 - m_2 \tag{3.1}$$

where m, m_1 and m_2 are the weight of sample, weight of sample + crucible and weight of crucible, respectively.

A detailed standard operational procedure (SOP) developed for carrying out DSC measurements using Seteram TG-DSC 111 is contained in Appendix A.1. The DSC was run in the vertical mode in order to create uniform heat distribution in the sample and the reference. A typical temperature profile used for all the DSC runs is shown in Figure 3.4. The samples were stabilized in the furnace at 25 ^{o}C for 30 minutes before ramping up to 825 ^{o}C at a heating rate of 10 ^{o}C/min. They were further kept at 825 ^{o}C for 1 h and then cooled to 25 ^{o}C at a cooling rate of 10 ^{o}C/min. The heating and cooling rates chosen were the optimal rates needed for the DSC to pick up reaction peaks in the materials and to reduce gas consumption during the experiments. The experiment was conducted in an inert environment, which was achieved by passing argon gas through the furnace at a pressure of 40 psi (0.275 MPa).

The data obtained from DSC runs were corrected for contributions of the crucible to the heat flow in the sample using the SETSOFT 2000 software. This correction was done using the data obtained from a blank run in which the empty alumina crucible was subjected to the same thermal conditions as those of the test samples. At least two DSC runs were carried out for each sample to ensure reproducibility. Figure 3.5 show that

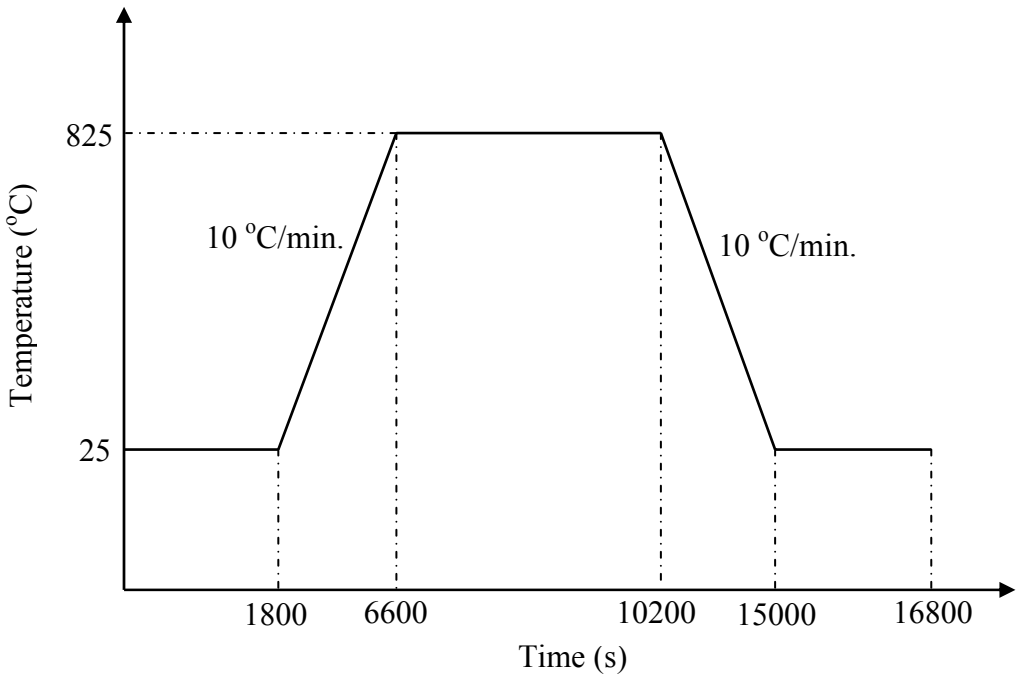

Figure 3.4. Temperature-time profile used for DSC measurements.

instrument-induced thermal lag affected the results obtained between 25 and 100 °C and between 750 and 825 °C. As such, data within these temperature ranges were not considered in interpreting the thermal behaviour of all test samples.

3.3.6 Thermomechanical Analysis

Thermomechanical analysis (TMA) was used to investigate the effect of fly ash content on the coefficient of thermal expansion (CTE) of A535 and its MMCs as well as the thermal strain induced when the materials were subjected to thermal cycling. The experiment was conducted in accordance with ASTM E831 (2003) standard using a Seteram Setsys Evolution 2000 Thermomechanical Analyzer that has an alumina hemispherical probe. A detailed SOP developed for carrying out the TMA experiments is contained in Appendix A.2. A load of 5 g was used for both experiments as recommended by the Seteram Inc. The length of the samples before and after each run was measured using a micrometer screw gauge. The initial and final sample lengths were measured five times and averaged. All the experiments were conducted in an argon

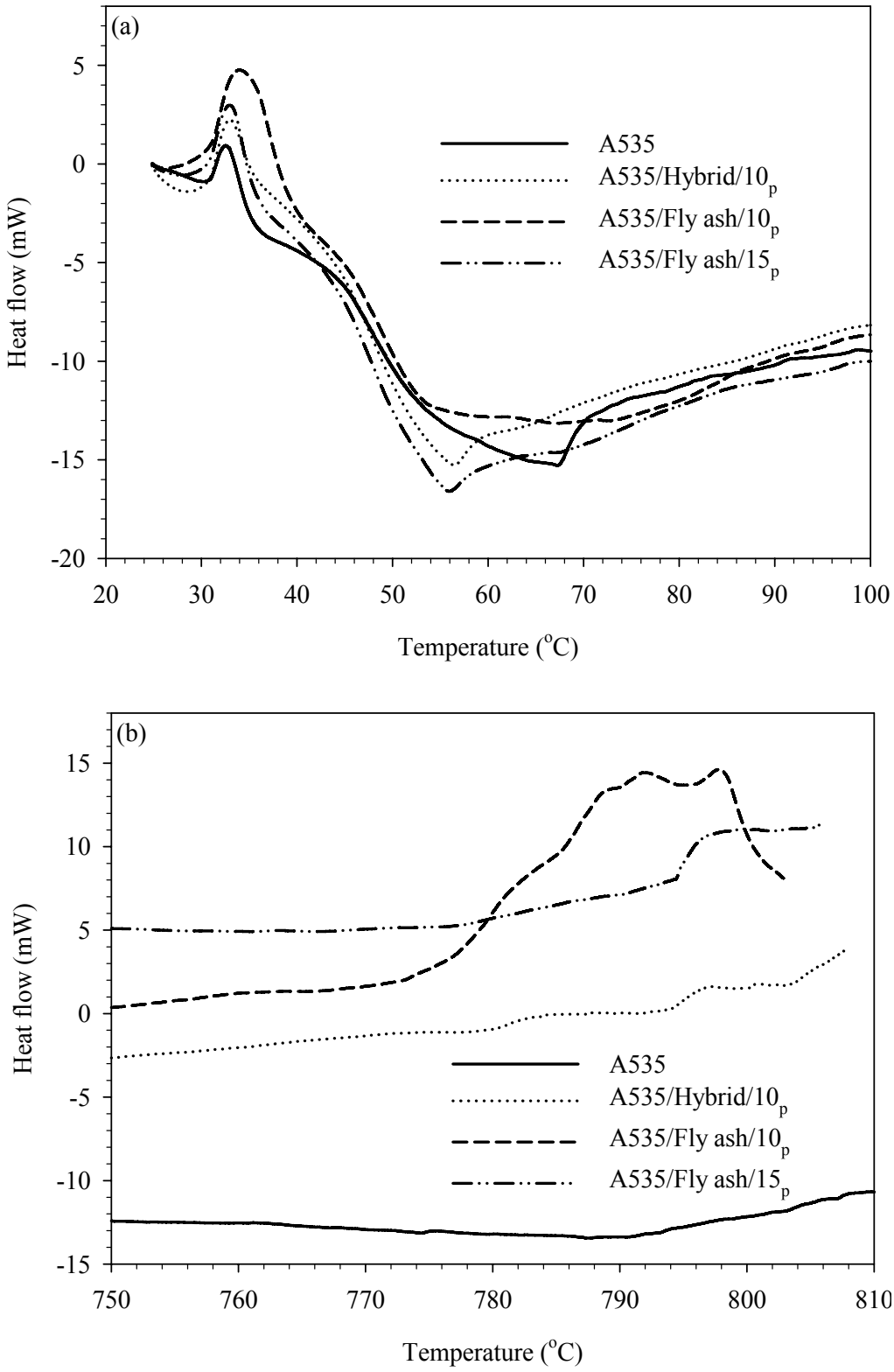

Figure 3.5. Typical DSC thermograms of A535 and its MMCs: (a) below 100 °C and (b) above 750 °C.

gas atmosphere to avoid oxidation. The gas pressure was maintained at 40 psi (0.275 MPa) for all runs.

The CTE and thermal cycling samples were subjected to the temperature-time profiles shown in Figures 3.6(a) and (b), respectively. The cooling water for the TMA was at about 40 ^{o}C because cold and hot water had to be mixed in order to sustain the flow rate required to run the TMA. The furnace temperature was maintained at 40 ^{o}C for 30 minutes for both experiments in order to achieve uniform heat distribution in the samples. In the CTE experiment, the sample temperature was raised from 40 to 500 ^{o}C at a heating rate of 2 ^{o}C/min. and then cooled to 40 ^{o}C at a cooling rate of 10 ^{o}C/min. In the thermal cycling experiment, the samples were subjected to 10 thermal cycles between 40 and 300 ^{o}C. This temperature range was chosen because the maximum operational temperature of components in internal combustion engines is up to 240 °C [102]. The samples were subjected to 10 thermal cycles in order to explore the effect of number of thermal cycles on the thermal strain generated in the samples. Two samples of each material were tested in the CTE and thermal cycling experiments to ensure reproducibility of the results obtained.

A sapphire sample tested under the same conditions as the samples was used as a reference for all TMA measurements. The displacement data generated from the sapphire run were used to calibrate the sample data in order to eliminate machine errors. The CTE of the samples was calculated using the "Average α" and "True α" subroutines in the SETSOFT 2000 software. The differences in the length of the sample and reference were corrected for when calculating the CTE of the samples using the mathematical expression shown in equation (3.3) [103].

$$e * CE_{(T)} = D_{1(T)} - D_{2(T)} + r * CR_{(T)} + (e - r) * CP_{(T)} \tag{3.3}$$

where e is the sample length in mm, r is length of the reference sample in mm, $CE_{(T)}$ is the expansion coefficient at temperature T of the sample in μ/^{o}C, $CR_{(T)}$ is the expansion

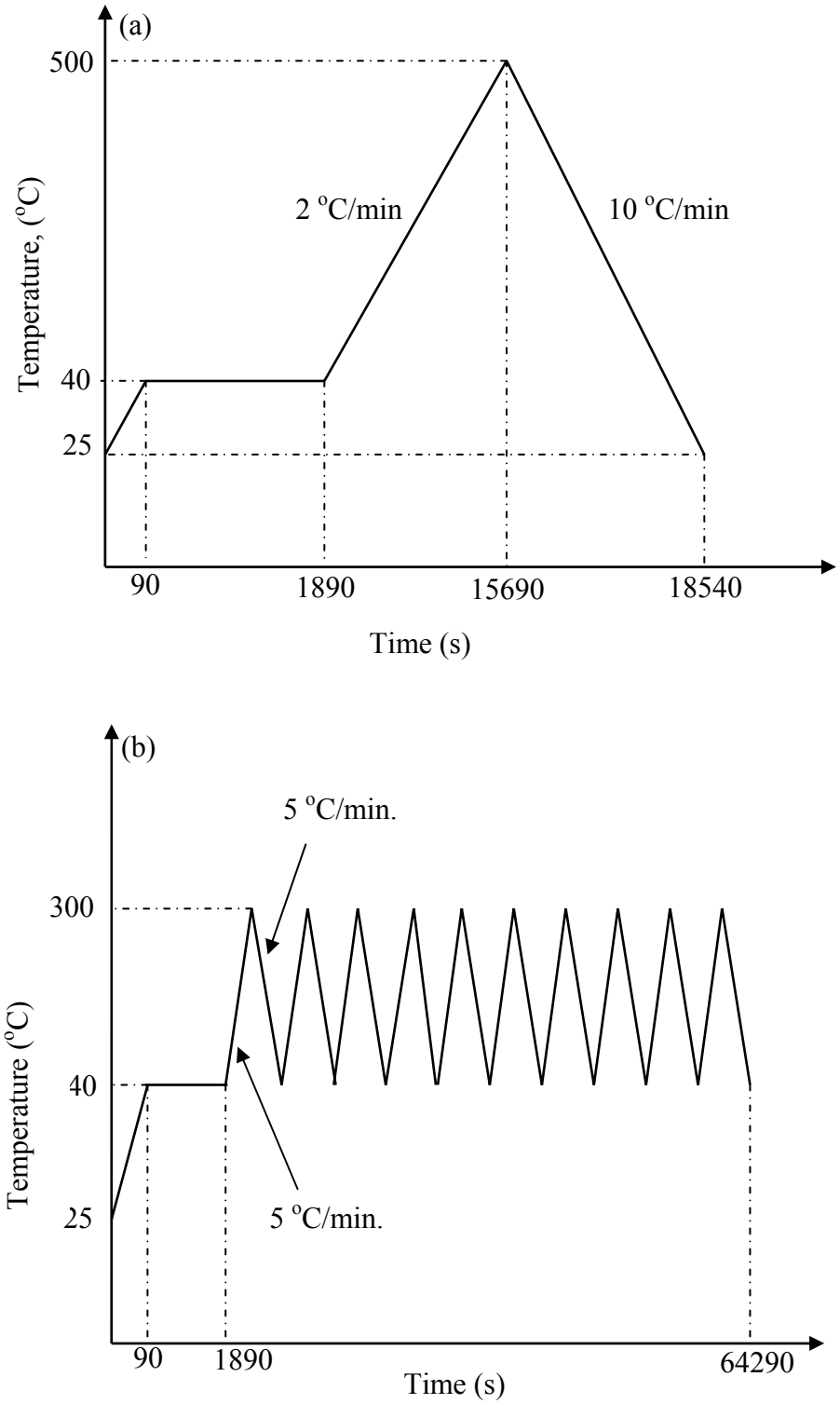

Figure 3.6. Temperature-time profiles used for (a) CTE and (b) thermal cycling experiments.

coefficient at temperature T of the reference sample in μ/°C, $CP_{(T)}$ is the expansion coefficient at temperature T of the tube by μ/°C, D_1 is displacement of the sample at temperature T in μm and D_2 is displacement of the reference sample at temperature T in μm.

Figure 3.7 shows a typical average and true CTE of the samples below 100 °C. As can be seen, a transition stage is observed at the beginning of the measurement due to thermal lag in the TMA equipment. The TMA data obtained below 100 °C might be erroneous and were not considered in interpreting the thermal behaviour of the materials.

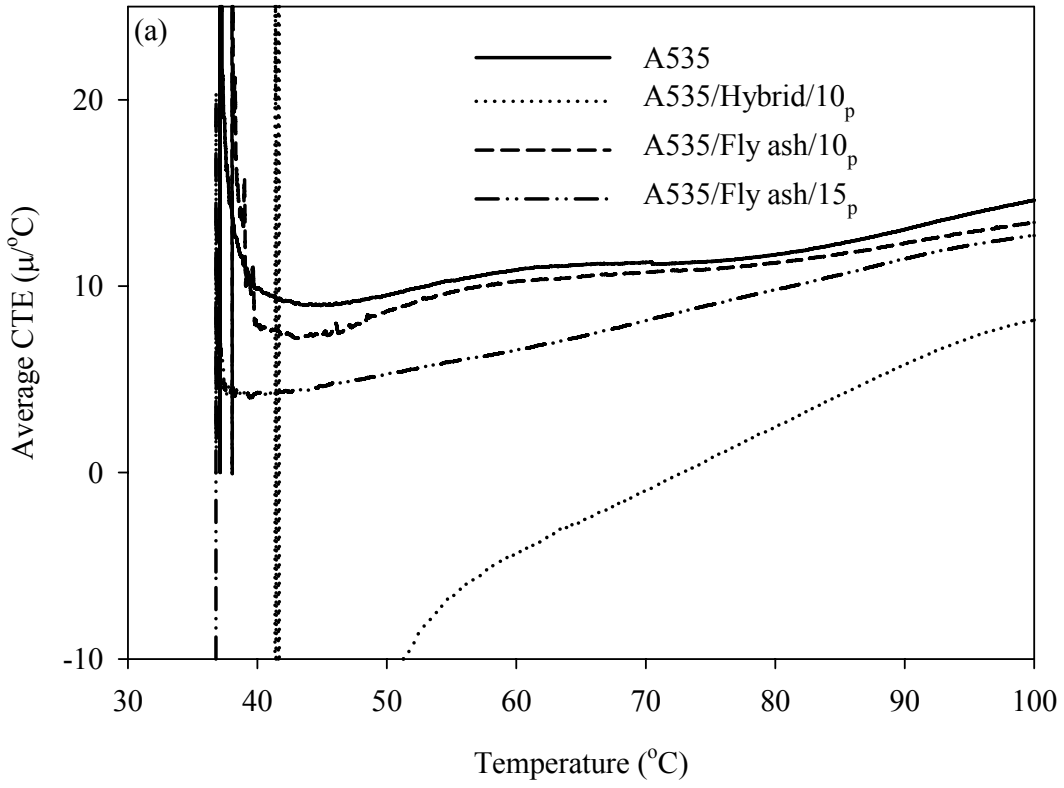

Figure 3.7. Typical (a) average and (b) true CTEs of A535 and its MMCs.

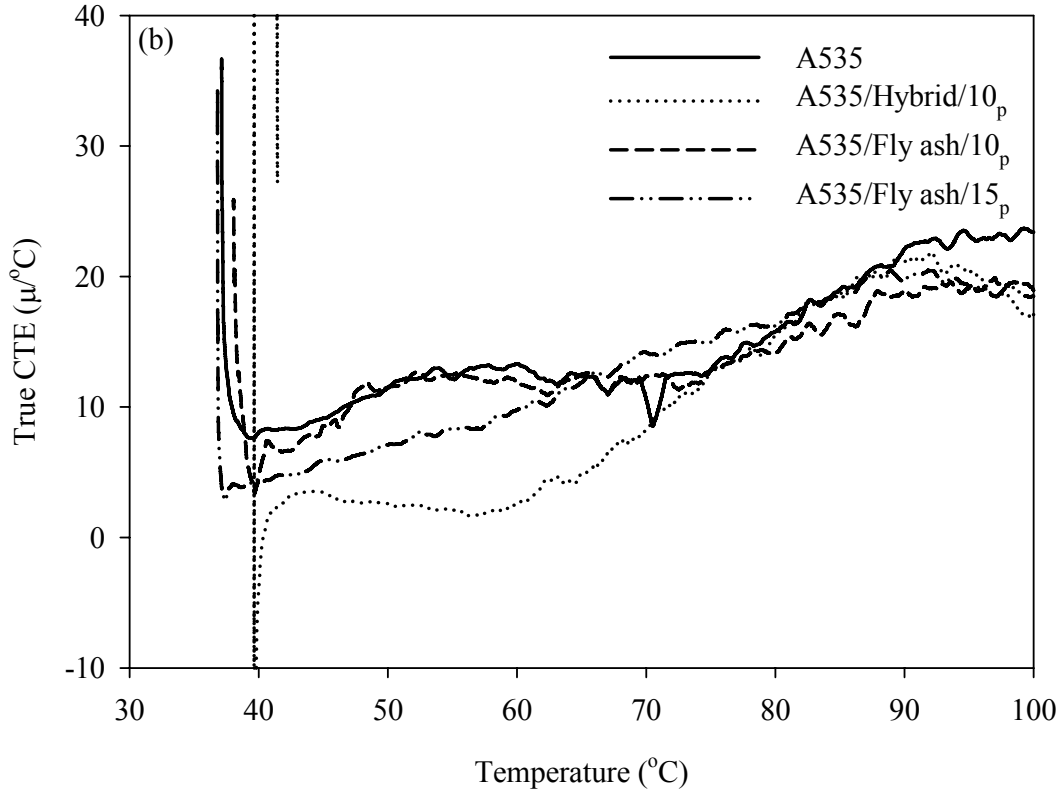

Figure 3.7 continues.

4.0 RESULTS AND DISCUSSION

This chapter presents and discusses the results obtained in this work. It is divided into three major sections, namely: (i) thermal behaviour of aluminium alloy A535 and its MMCs, (ii) reactivity in A535 and its MMCs, and (iii) X-ray absorption spectroscopy study of aluminium alloys and their MMCs.

4.1 Thermal Behaviour Study of Aluminium alloy A535 and Its Composites

The result obtained for A535 and its composites from the coefficient of thermal expansion (CTE) and thermal cycling measurements are presented in this section.

4.1.1 The Effect of Fly Ash on the Coefficient of Thermal Expansion of A535

Figure 4.1 shows the variation of displacement (change in length) of A535 and its MMCs with temperature. As expected, it can be seen that the displacement of the test materials increased with temperature. This could be attributed to the asymmetric nature of the inter-atomic forces and increase in the amplitude of atomic vibrations in the materials with temperature [69].

Figure 4.2 shows a comparison of the average CTE of A535 obtained in this work and that from reference [56]. It can be seen from Figure 4.2(a) that the CTE of A535 obtained in this work and that from reference [56] increased with temperature. However, the CTE obtained experimentally was lower than that reported in reference [56]. This could be attributed to the sample conditions, which most likely differ from that of the samples reported in references [56] and [34]. The observed increase in the average CTE with temperature agrees with what was reported in [42] for A359-SiC and A360-SiC. Also, it can be seen that there are undulations in the CTEs data. The observed undulations below 450 ^{o}C in Figure 4(a) are most likely due to vibration of the TMA or

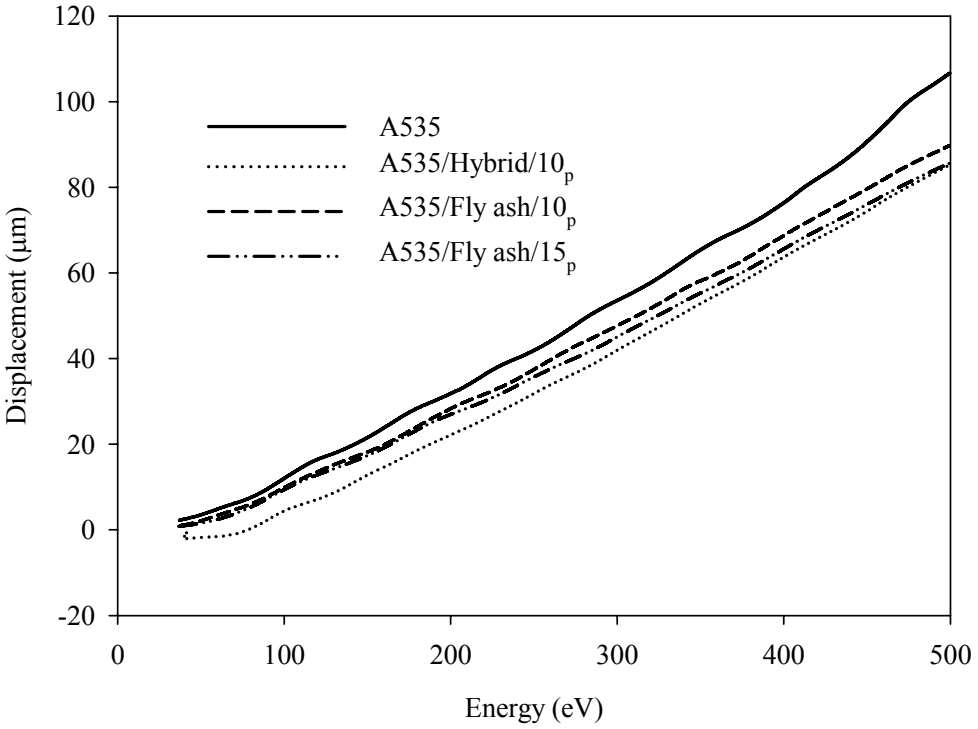

Figure 4.1. Change in length (displacement) of A535 and its composites.

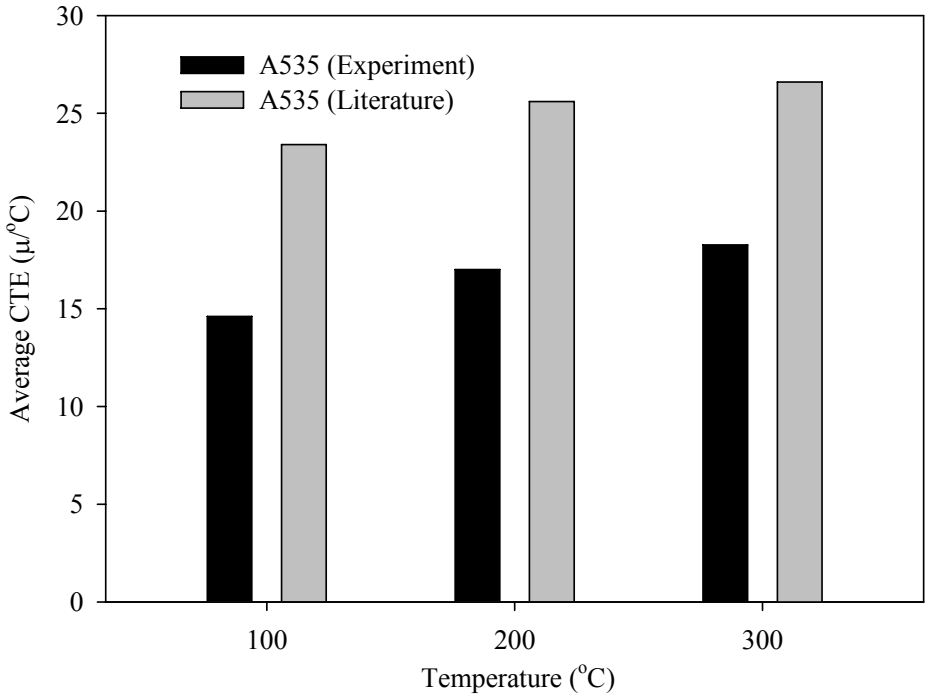

Figure 4.2. Comparison of average CTE of A535 obtained experimentally and that from reference [59].

from an external source during measurement. Those that occurred after 450 ^{o}C are within the temperature range where β-phase (Mg_2Al_3) dissolves in binary Al-16 at.% Mg alloy [105].

Figure 4.3(a) compares the CTE of A535 and its MMCs with increase in temperature composites and in [55] for Al-fly ash composites, while Figure 4.3(b) shows the plots of the average CTE obtained for two test materials obtained at 100 ^{o}C, 200 ^{o}C, *etc*. It can be seen from Figure 4.3(a) that the average CTE of A535 is greater than those of the composites and this can be attributed to the low CTEs of fly ash constituents (see Table 2.3). Similar observations were reported for the CTE of AA6061 composites reinforced with albite particles in [71] and aluminium MMC reinforced with fly ash in [55]. The CTE of the MMC reinforced with the hybrid reinforcement is the lowest among the MMCs, thereby suggesting that SiC has a stronger effect on the CTE of A535 than fly ash. This could be attributed to the low CTE of SiC when compared with some of the constituent oxides of fly ash (see Table 2.3). Elomari *et al.* [72] reported that A6061 reinforced with SiC had lower CTE than that reinforced with alumina due to the lower CTE of SiC compared to alumina. As can be seen from Figure 4.3(b), the addition of fly ash and SiC to A535 decreased its CTE.

Figure 4.4 shows the effect of double thermal excursions on the CTE of A535 and its MMCs. The samples were subjected to the same temperature-time profile used for the displacement measurements in order to evaluate the extent of thermal stresses induced in them during cooling from the maximum heating temperature. It can be seen from Figure 4.4(a) that the CTE of the alloy obtained during the first thermal excursion is higher than that obtained during the re-heat cycle. This suggests that the residual stresses induced in A535 during fabrication was relieved appreciably during the first cycle and, as such, did not affect the CTE of the alloy during the re-heat cycle. Chen *et al.* [80] have reported stress relaxation in pure aluminium during thermal excursion. It can be seen from Figure 4.4(b) that the CTE obtained for A535/Hybrid/10_p during the re-heat cycle is higher than that obtained from the first heating cycle. This behaviour could be due to the accumulation of residual stresses induced in the alloy during cooling from fabrication

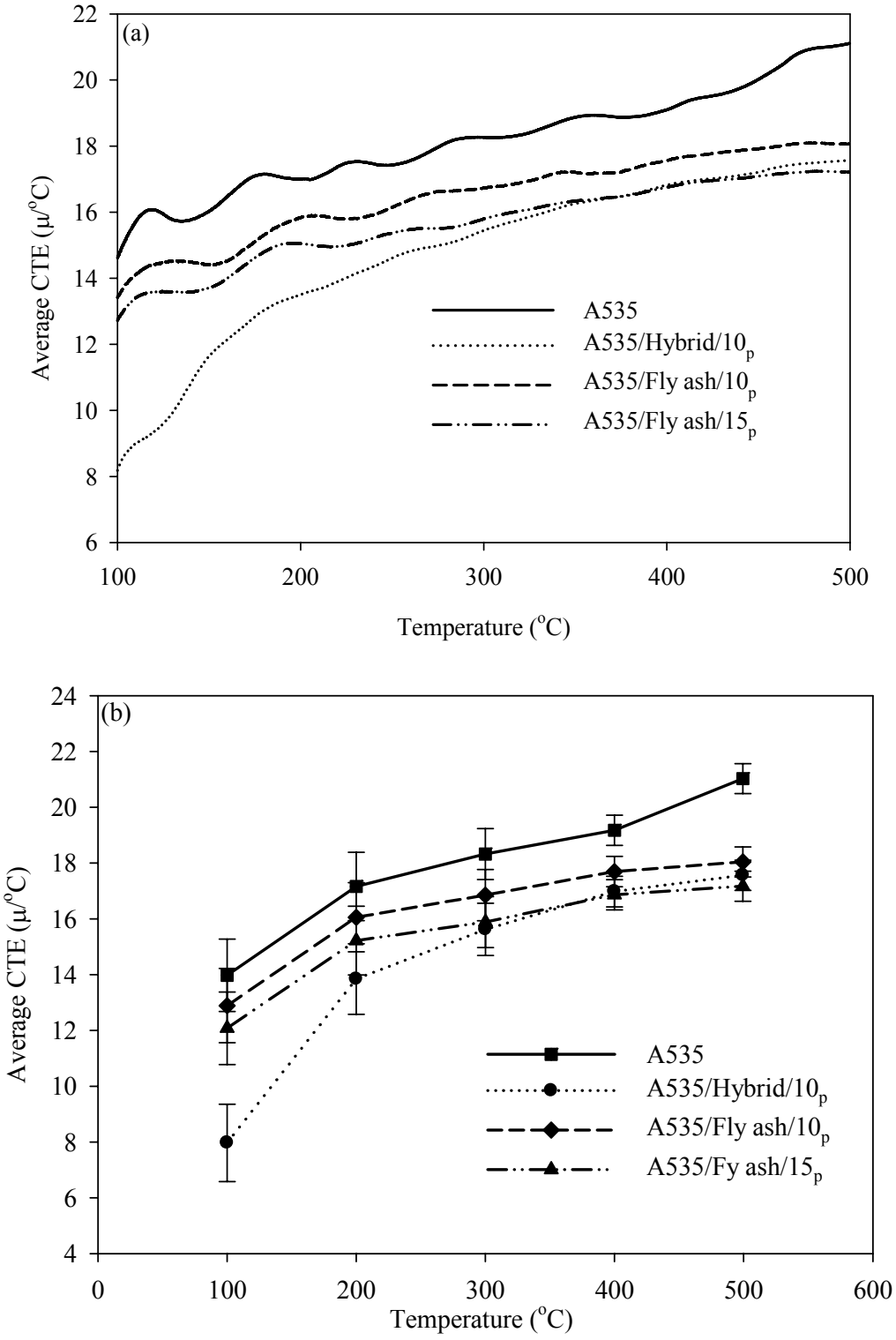

Figure 4.3. Variation of the average CTE of A535 with the addition of fly ash: (a) one test sample and (b) average of two test samples. The error bars are based on standard deviation.

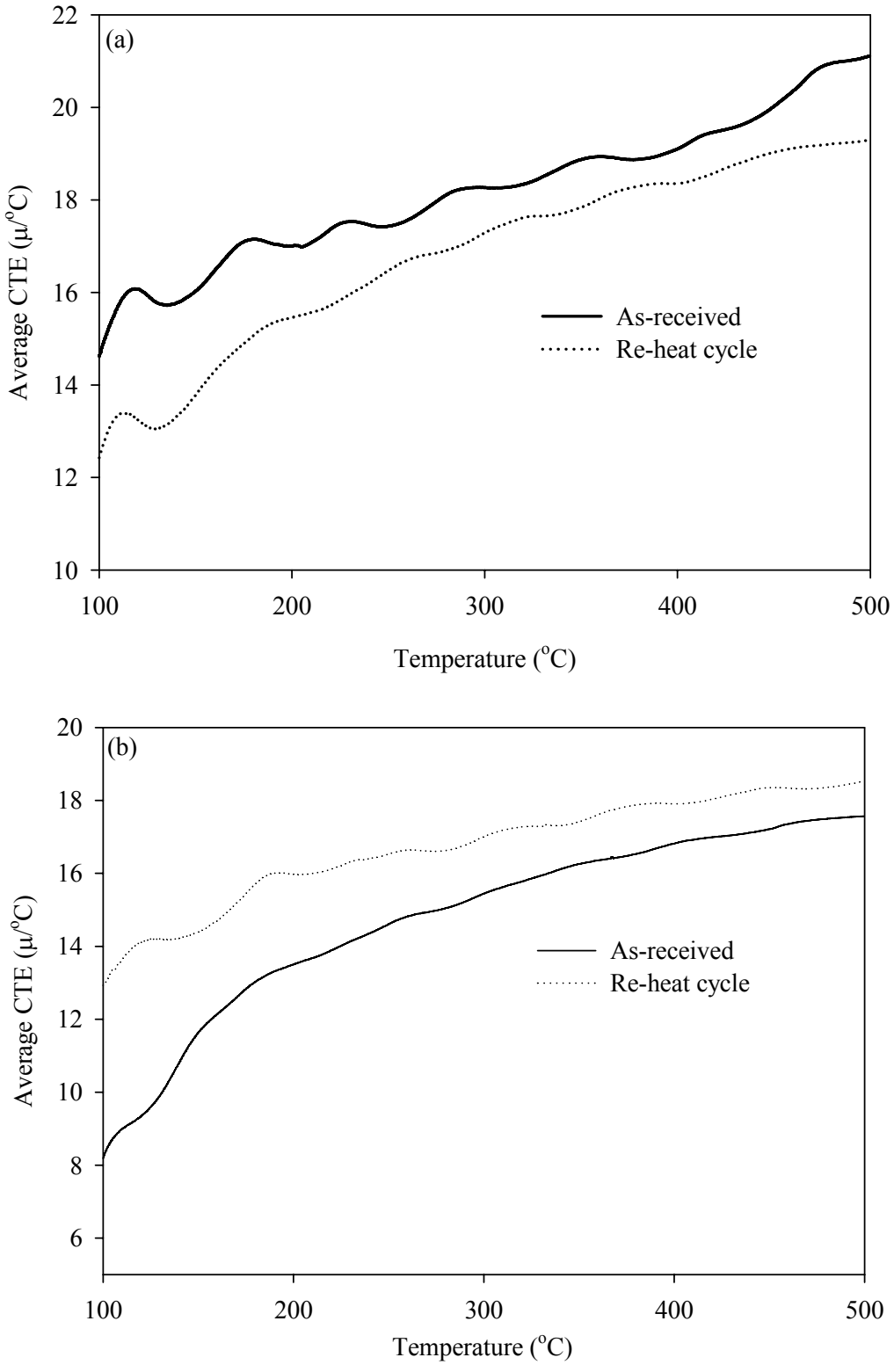

Figure 4.4. Effect of double heat treatment on the CTE of: (a) A535, (b) A535/Hybrid/10_p, (c) A535/Fly ash/10_p and (c) A535/Fly ash/15_p.

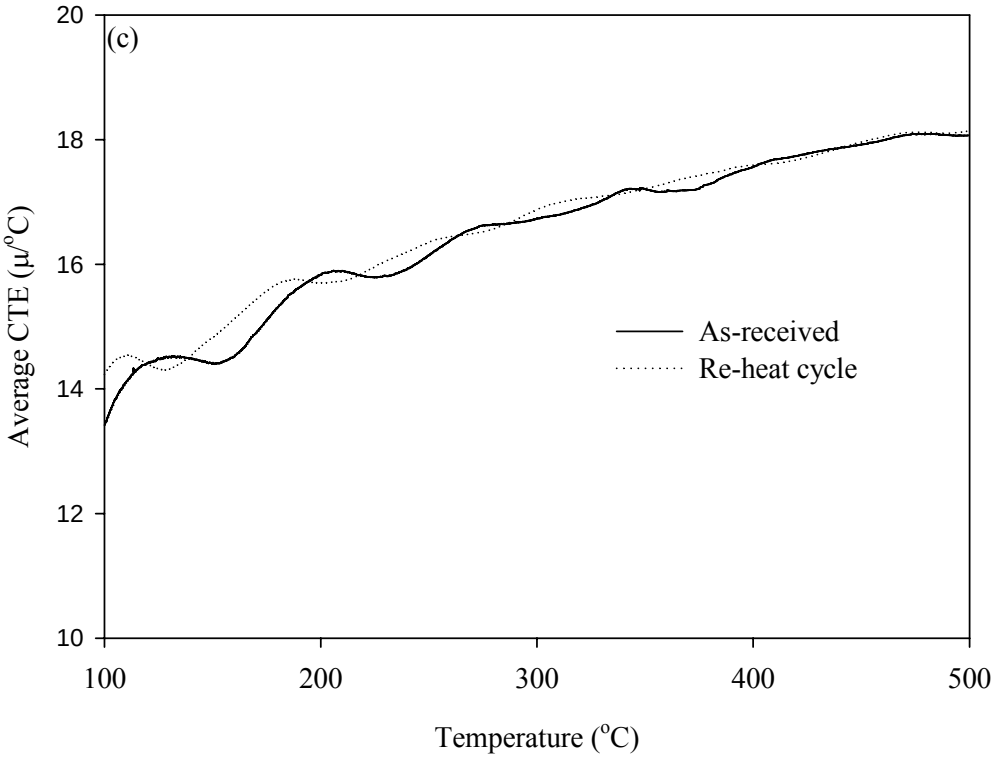

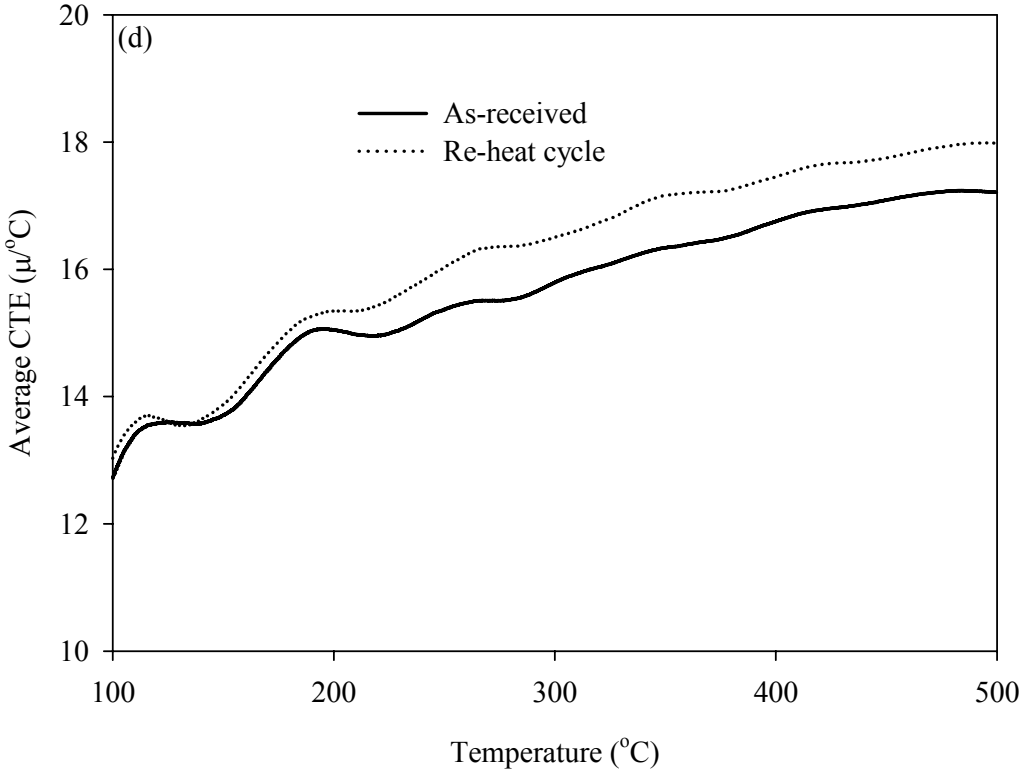

Figure 4.4 continues.

and maximum cycling temperature. Rohatgi *et al.* [55] reported that during thermal cycling the average CTEs of aluminium-fly ash cenosphere MMCs obtained during the second thermal cycle were slightly higher than those obtained for the as-received samples in the first cycle. They attributed this to the influence of internal stresses built around the reinforcement during the first cycle, which deformed the matrix plastically in the second cycle. In another thermal cycling study, the CTEs of Al-SiC MMCs during the second thermal cycle were found to be higher than those obtained in the first cycle [74].

The residual thermal stress induced in MMCs is usually due to the difference in the CTE of the ceramic and matrix materials [22, 55, 66, 67]. The reduced difference in the CTEs of the as-received and re-heated samples of A535/Fly ash/10_p composite (see Figures 4.4(c) and (d)) could be attributed to the presence of microvoids which were determined in reference [16] to be 5.3% and 9.2% in A535/Fly ash/10_p and A535/Fly ash/15_p, respectively. It is possible that these microvoids provided room for free expansion of the ceramic and matrix materials during heating. This expansion would annihilate some of the voids contained in the MMCs which, in turn, reduced the induced residual stress during the cooling cycle. This assessment is in agreement with the observation made by Balch *et al.* [76] for SiC foam-reinforced aluminium MMCs. They reported that at high temperatures, the CTE of aluminium-foam MMCs decreased due to the closure of pre-existing microvoids as the matrix deformed plastically within the region. The CTE obtained for A535/fly ash/15_p composite during the re-heat cycle increased when compared with the first heating cycle. This contradicts the observation made for A535/Fly ash/10_p. A possible reason for this behaviour is that the additional 5% increase in the weight percentage of fly ash present in the A535/Fly ash/15_p induced a net positive residual stress in it as it cools from the maximum cycling temperature despite the increase in the amount of voids.

Figure 4.5 shows the true (instantaneous) CTE of A535 and its composites as a function of temperature. As in the case of the average CTE results, it is seen that the true CTE of the test materials changed in an undulating manner as temperature increased, which

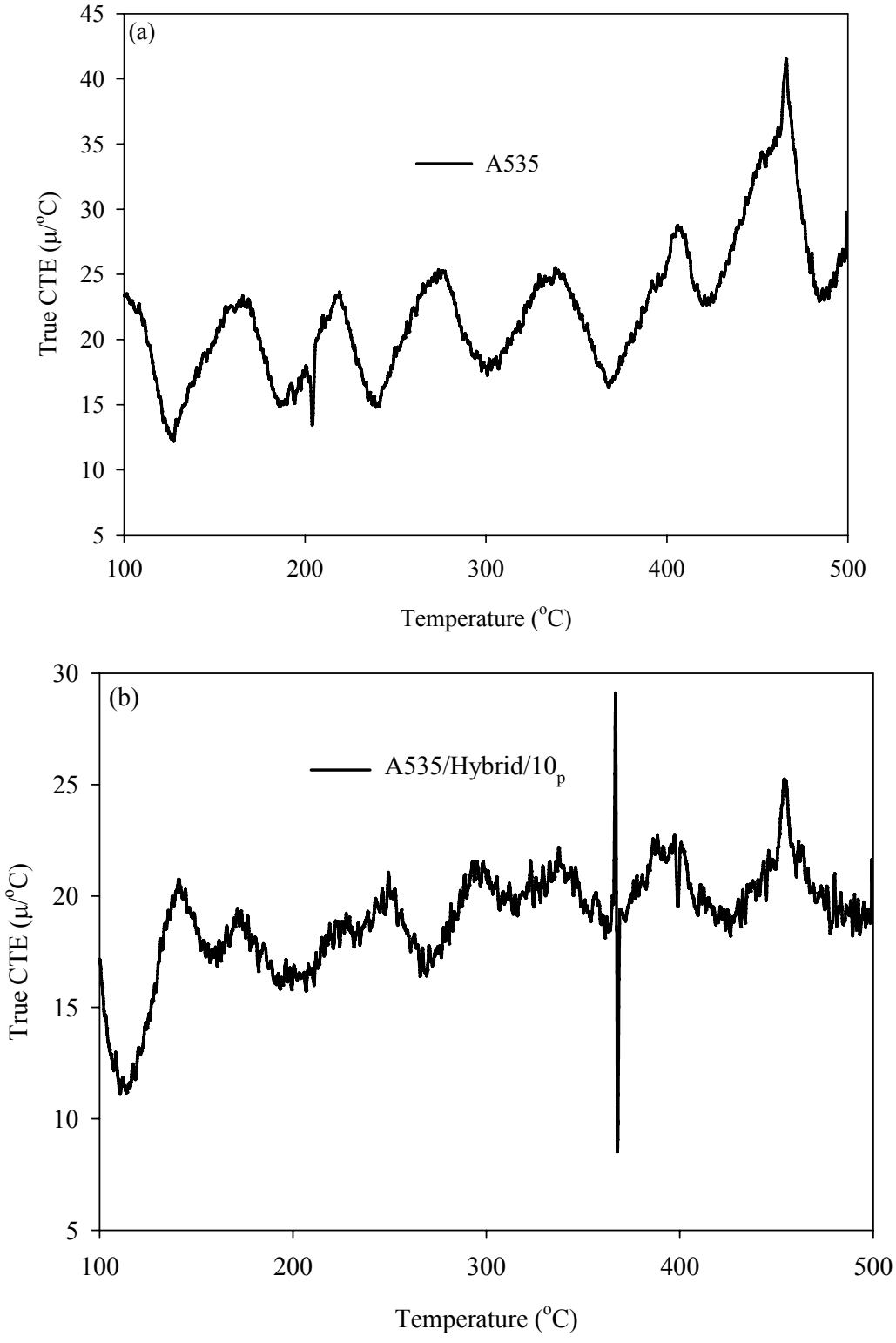

Figure 4.5. Variation of instantaneous/true CTE with temperature for: (a) A535, (b) A535/Hybrid/10_p, (c) A535/Fly ash/10_p, (d) A535/Fly ash/15_p and (e) all samples.

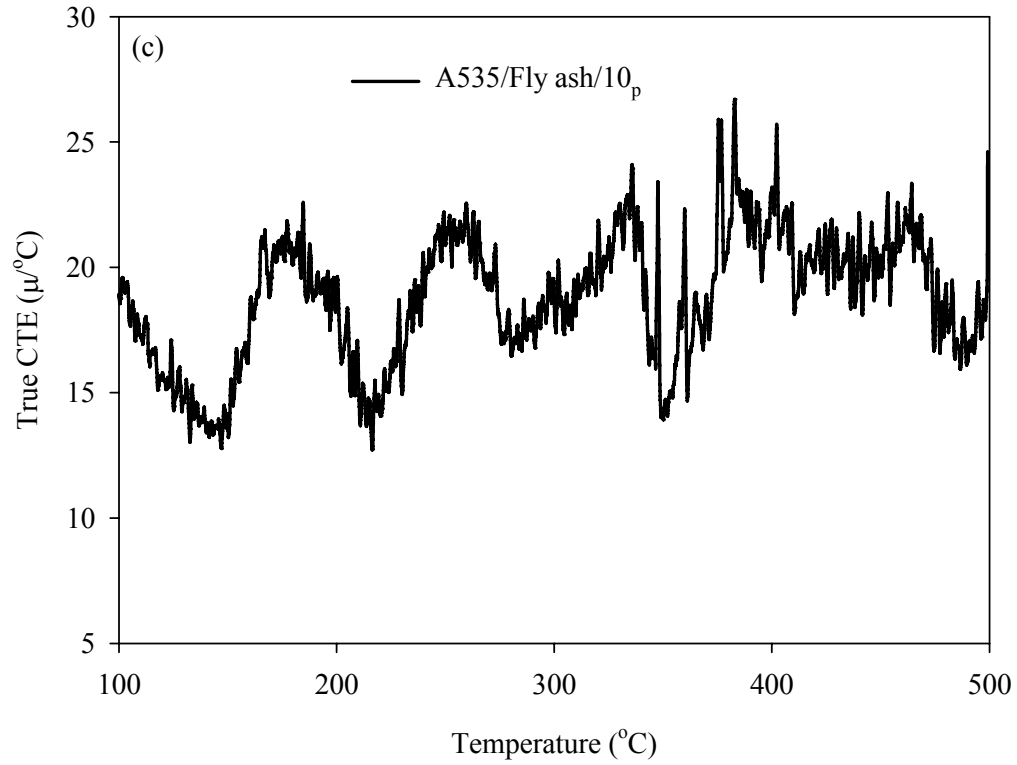

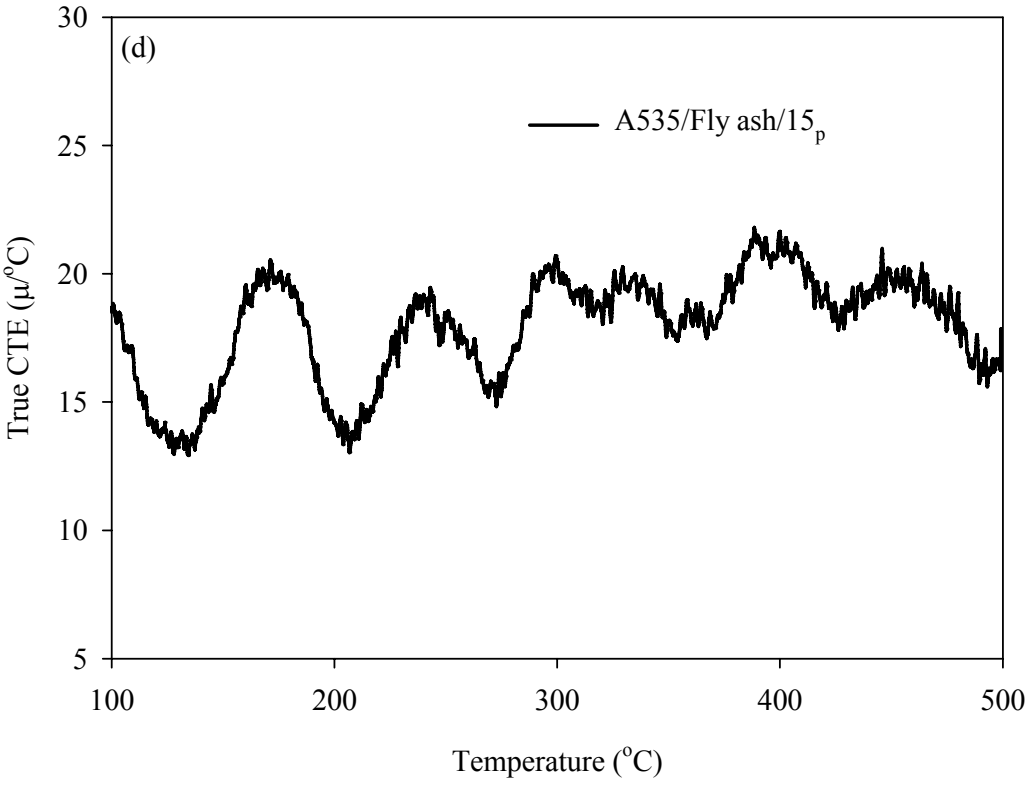

Figure 4.5 continues.

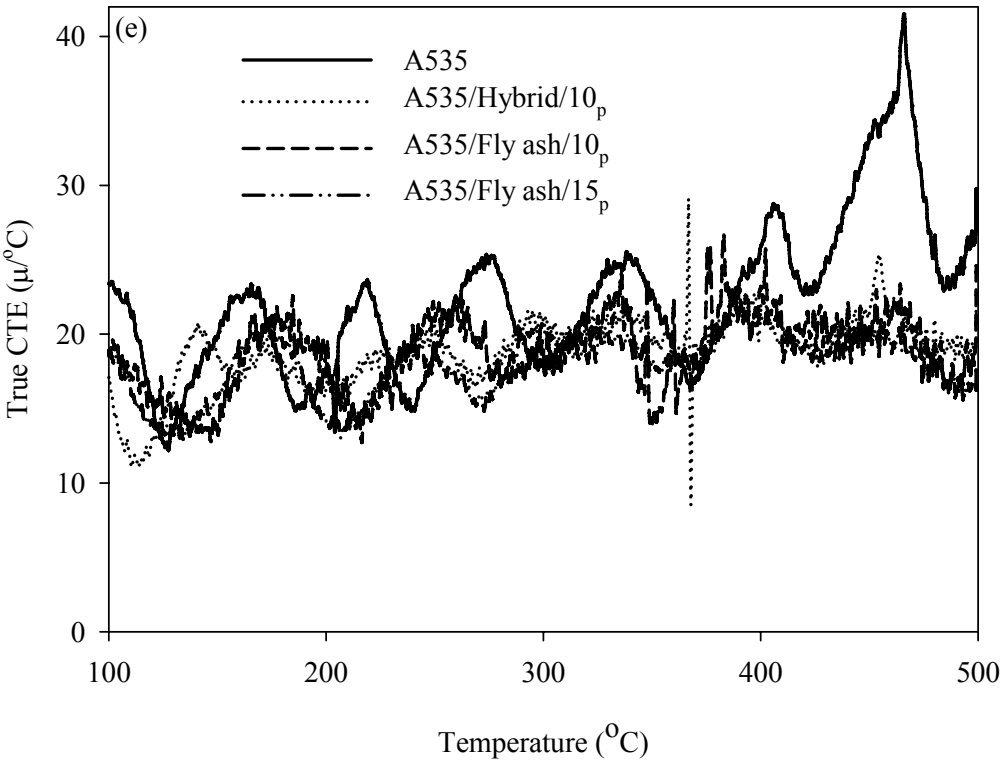

Figure 4.5 continues.

could be vibrations from the instrument or external source. Also it can be seen that the true CTE of the alloy is higher than those of the composites, showing that the addition of SiC and fly ash to A535 decreased their true CTE.

Table 4.1 shows the average CTEs determined for samples of A535 and the composites at 100 ^{o}C and those calculated using the rule of mixture (ROM) [22] and models proposed by Turner [78], Kerner [79], and Schapery [77]. The theoretical CTEs of the MMCs were calculated using the bulk and shear moduli, and CTEs of the main constituents of the composites shown in Tables 2.3 and B.1, respectively. The bulk and shear moduli of A535 as well as that of Fe_2O_3 in fly ash and its CTE were replaced with those of Al-5 wt.% Mg alloy and magnetite, respectively, due to unavailability of pertinent data in the open literature. The properties of Al-5 wt.% Mg alloy, silica, alumina and silicon carbide were adapted from reference [60], while the CTE and bulk modulus of magnetite were adapted from references [82] and [104], respectively.

Table 4.1. Average CTEs of the test materials obtained experimentally at 100 ^{o}C and those calculated using various models.

Materials	Average CTE ($\mu/^{o}C$)	ROM ($\mu/^{o}C$) [22]	Turner's Model ($\mu/^{o}C$) [78]	Kerner's Model ($\mu/^{o}C$) [79]	Schapery's Model* ($\mu/^{o}C$) [77]	
					L	U
A535	14.6	---	---	---	---	---
A535/Hybrid/10_p	8.2	24.8	17.2	22.8	24.5	25.1
A535/Fly ash/10_p	13.4	24.7	17.2	23.6	16.8	17.0
A535/Fly ash/15_p	12.7	23.8	15.1	22.1	14.6	15.4

*The letters L and U represent the upper and lower limits of the Schapery model, respectively. The numbers in square brackets are references.

Sample calculations are included in Appendix B.1. It can be seen that the average CTEs of A535 composites are lower than those predicted by the ROM and the models. The CTE of A535/Hybrid/10_p is 48% of that predicted by Turner's model, while those of A535/Fly ash/10_p and A535/Fly ash/15_p were 80 and 87% of those predicted by the lower limits of Schapery model, respectively. These differences could be attributed to the microstructure of the MMCs and the stress distribution in them, which differ from the assumptions made in the ROM and the other models.

4.1.2 Effect of Thermal Cycling on the Dimensional Stability of A535 and Its Composites

Figure 4.6 and 4.7 respectively show the displacement (change in length) and thermal cycling strain curves obtained for samples of A535 and the MMCs which cycled between 40 and 300 ^{o}C. It can be seen from the figures that hysteresis loops were induced in all the test materials during thermal cycling. The formation of hysteresis loops in MMCs subjected to thermal cycling has been reported by some researchers [58, 65-68]. Tjong *et al.* [66] reported that hysteresis loops were induced in Al MMCs reinforced with insitu Al_3Ti plate and Al_2O_3 particles during thermal cycling. They attributed these to induced thermal stress formed in the materials during cooling from the fabrication and maximum cycling temperatures.

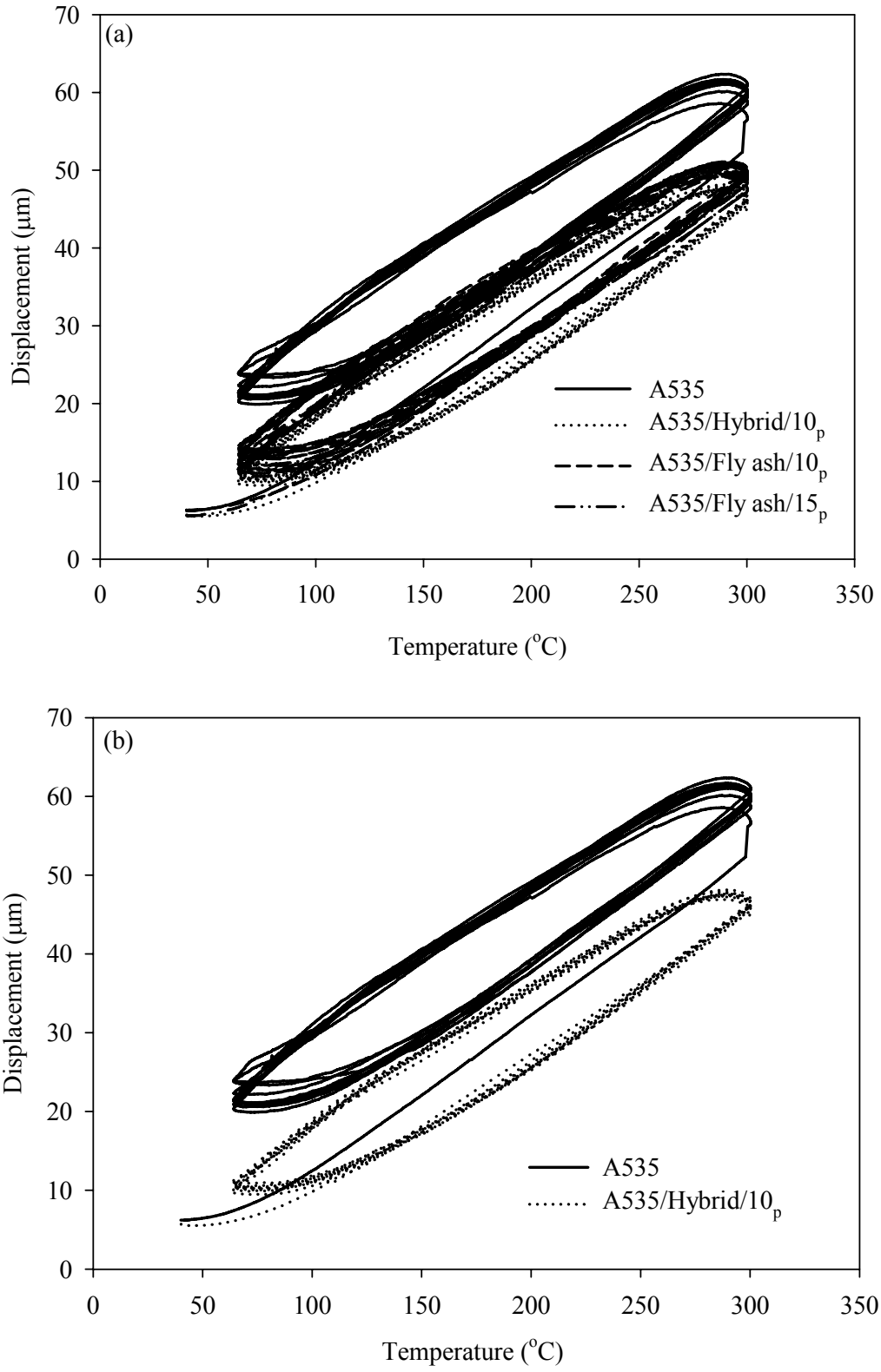

Figure 4.6. Thermal displacement versus temperature plots obtained for A535 and the composites during thermal cycling.

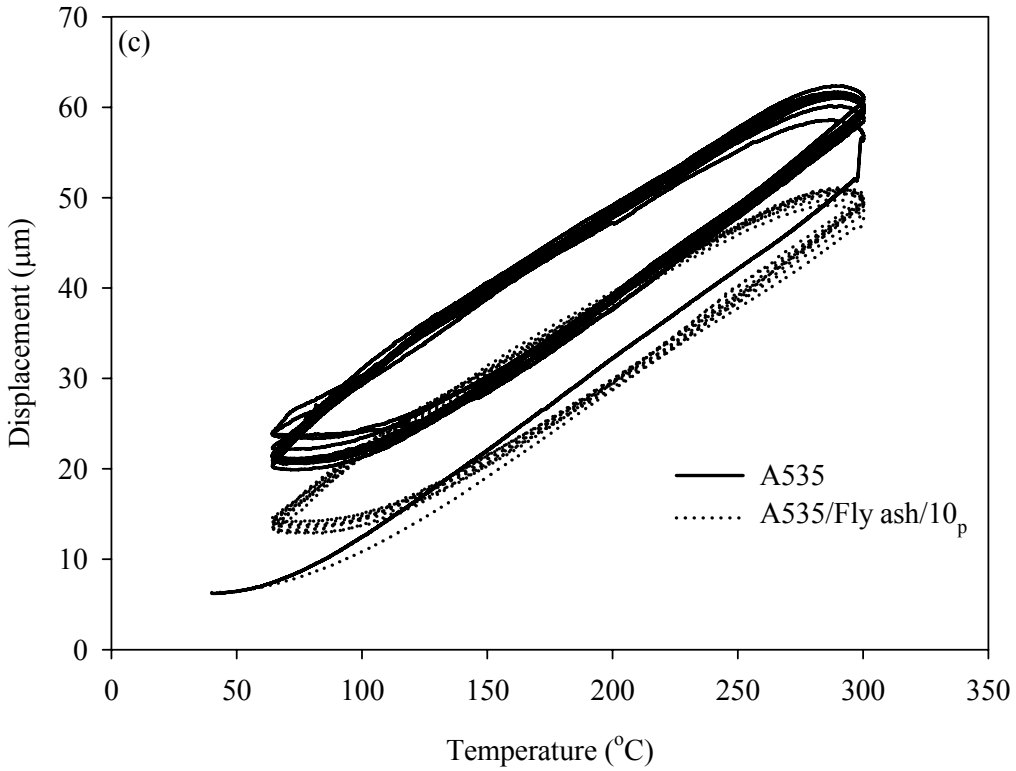

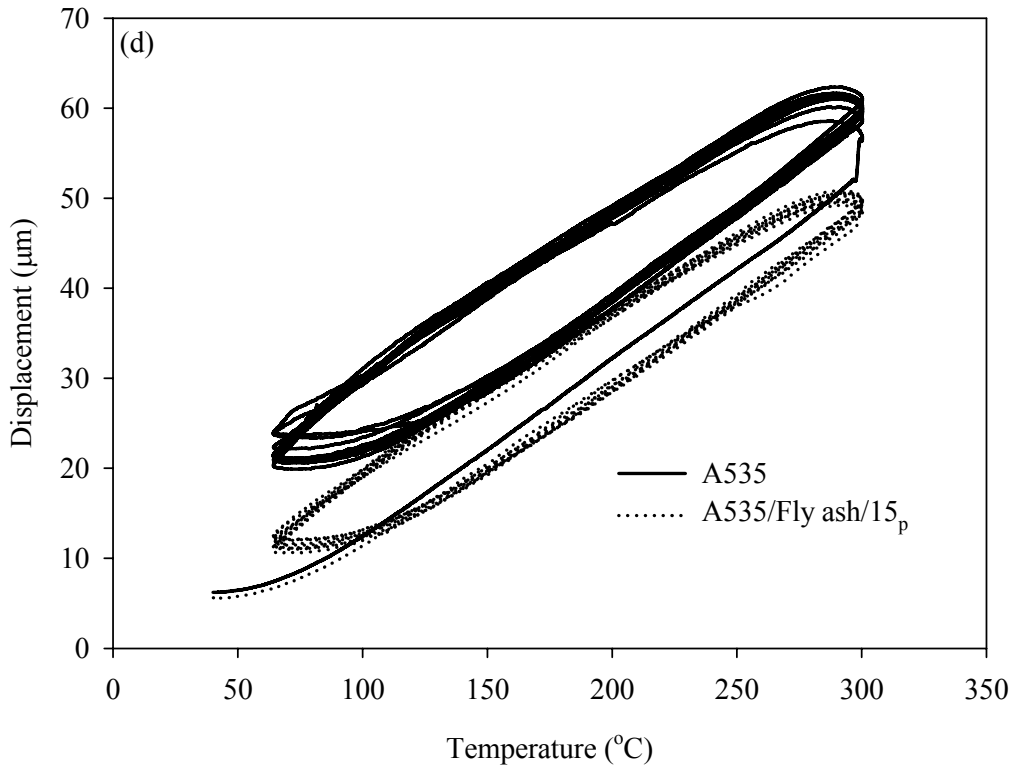

Figure 4.6 continues.

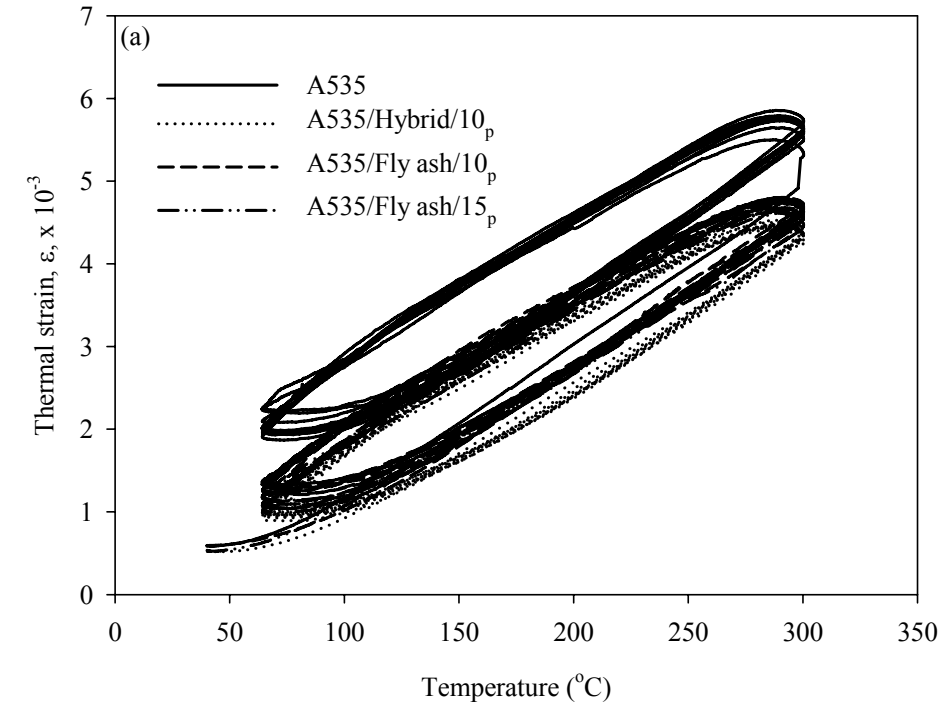

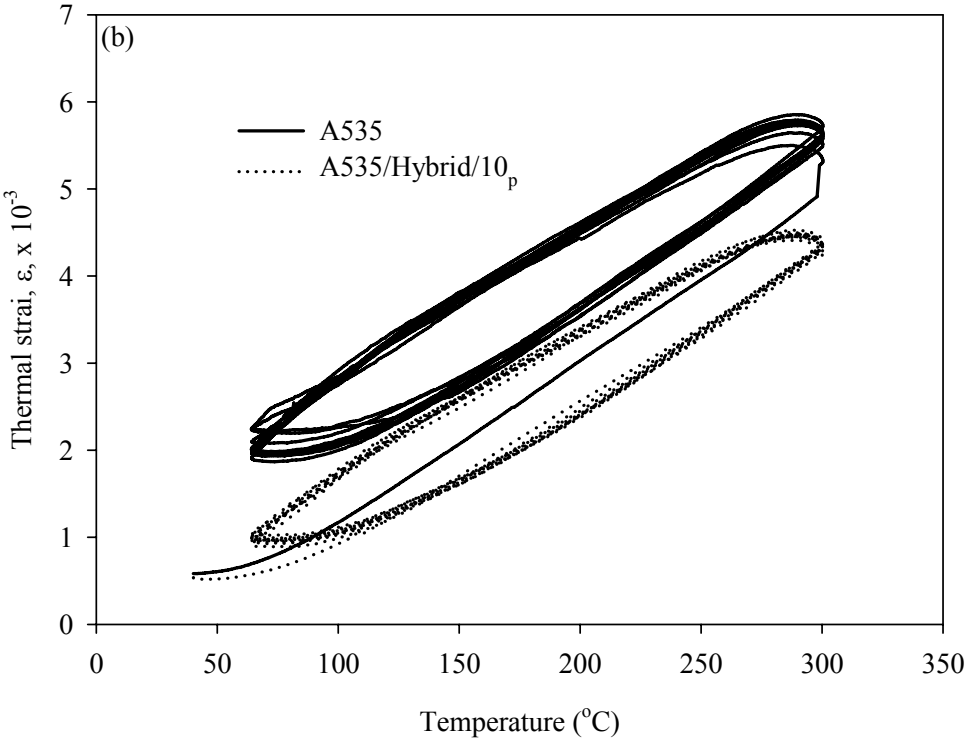

Figure 4.7. Thermal strain versus temperature plots obtained for A535 and the composites during thermal cycling.

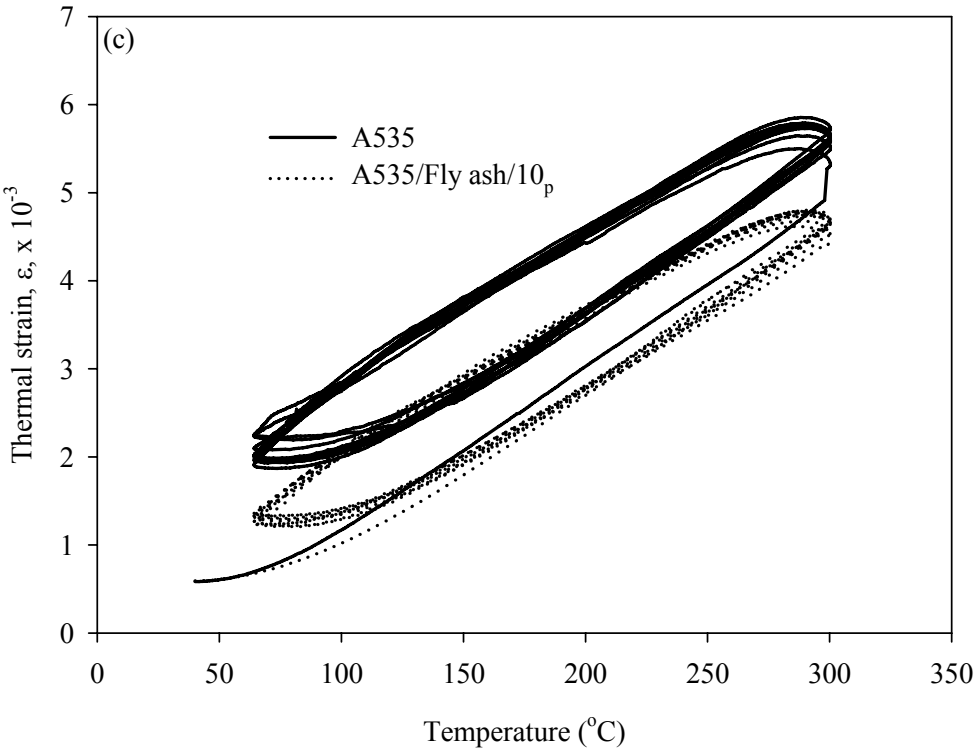

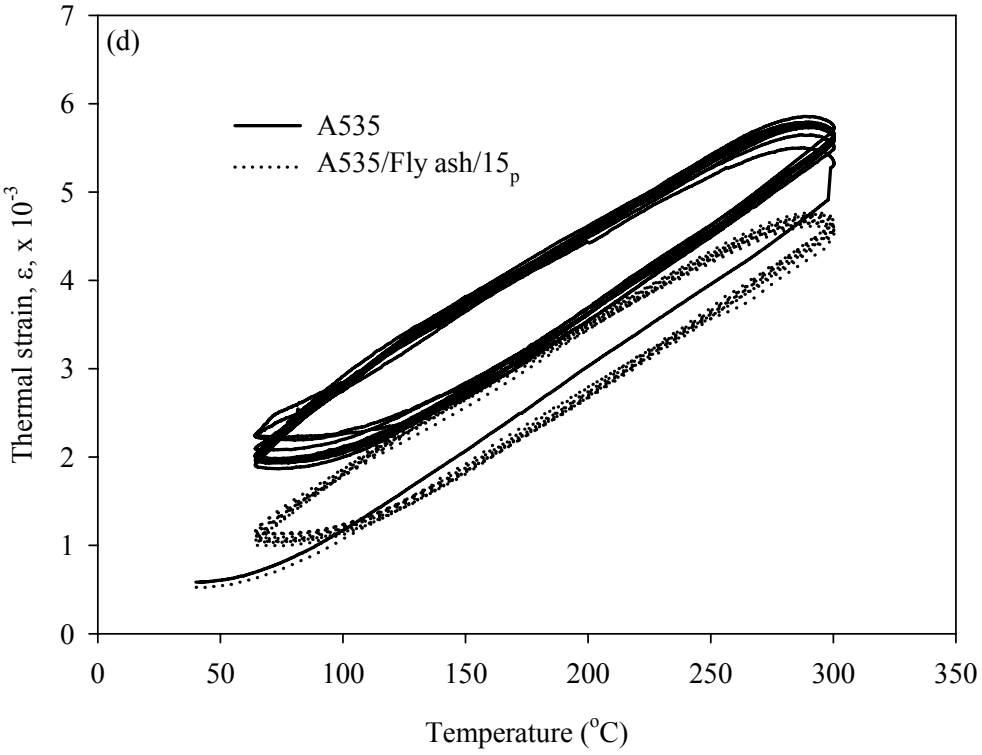

Figure 4.7 continues.

Figures 4.8 and 4.9 show the variation of strain parameters (i.e., ε_p, ε_T, ε_c and $\Delta\varepsilon$) obtained for the test materials with number of thermal cycles. The symbols ε_p, ε_T, ε_c and $\Delta\varepsilon$ represent the residual plastic strain, total strain, cyclic strain and strain height induced in the materials during thermal cycling. ε_p for the test materials was obtained using two methods, namely: (i) Dividing their minimum displacement at the end of each cycle with their original lengths (l_o) and (ii) extracting the strain at the end of each cycle from the strain data generated using the Setsoft software. Similarly, ε_T for the test materials was obtained using two methods, namely: (i) Dividing their maximum displacements in each cycle with their original lengths (l_o) and (ii) extracting the maximum strain in each end of each cycle from the strain data generated using the Setsoft software. In both methods, ε_c was determined from the difference between ε_T and ε_p. $\Delta\varepsilon$ was determined for each cycle from the maximum strain obtained from (i) the difference between the maximum and minimum displacement at each temperature in each cycle divided by the original length of the test materials and (ii) the difference between the maximum and minimum strains at each temperature. A more detailed discussion of these strain parameters is given in Chapter 2. The mathematical expressions used for computing ε_p, ε_T, $\Delta\varepsilon$ and ε_c are shown in equations (4.1)-(4.4), respectively.

$$\varepsilon_p = \frac{\text{Displacement at the end of each cycle}}{\text{original length } (l_o)} \tag{4.1}$$

$$\varepsilon_T = \frac{\text{Maximum displacement in each cycle}}{\text{original length } (l_o)} \tag{4.2}$$

$$\Delta\varepsilon = \frac{\left[(\text{Displacement during heating}) - (\text{Displacement during cooling})\right]_{\text{max.}}}{\text{original length } (l_o)} \text{ at } T^oC \tag{4.3}$$

$$\varepsilon_c = \varepsilon_T - \varepsilon_p \tag{4.4}$$

It can be seen from the figures that the strain parameters obtained from both methods are about the same. Based on this, the strain parameters obtained from the strains computed by Setsoft software (i.e., Figure 4.9) will be used in this work. Values of ε_p for temperatures below 64 ^oC were not determined because the thermal lag in the TMA

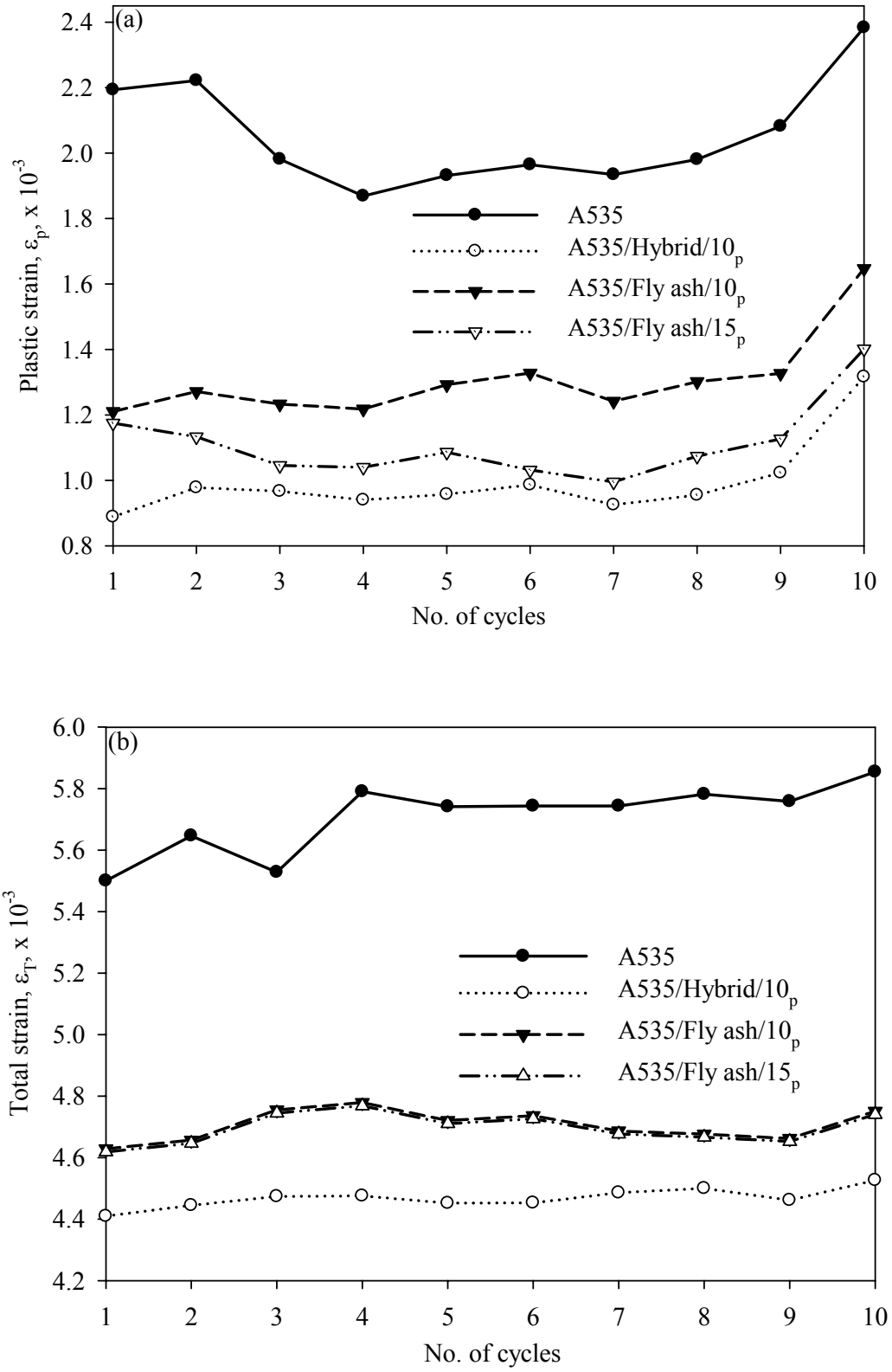

Figure 4.8. ε_p, ε_T, ε_c and $\Delta\varepsilon$ obtained for the test materials as a function of number of cycles.

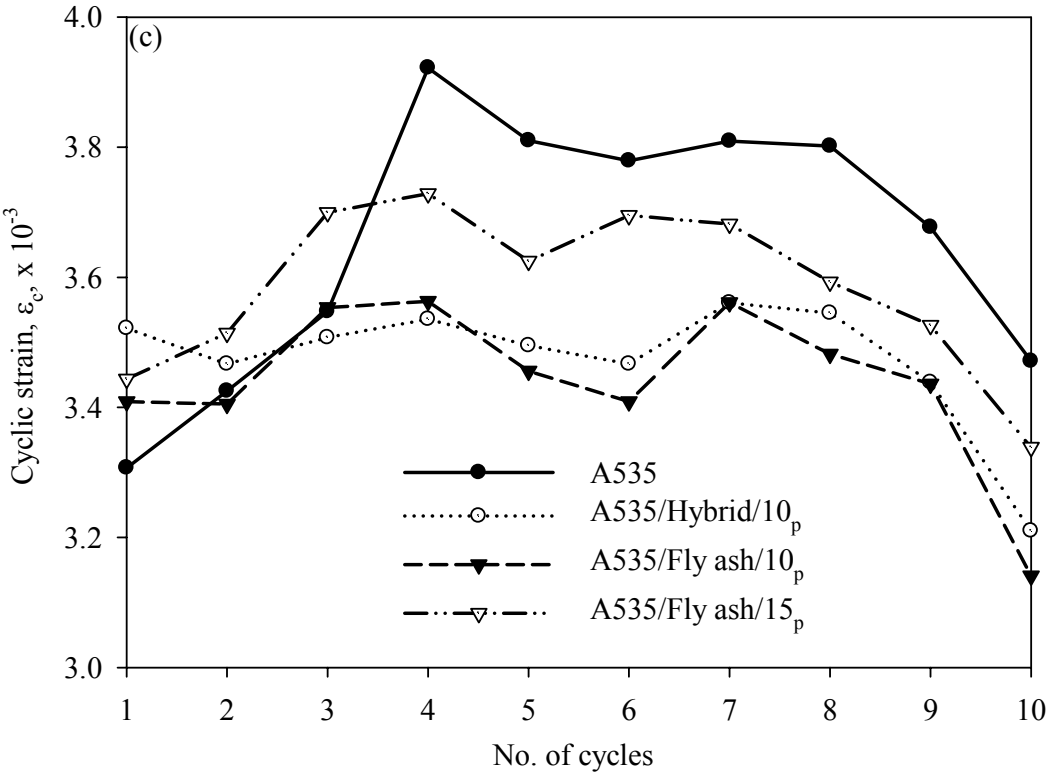

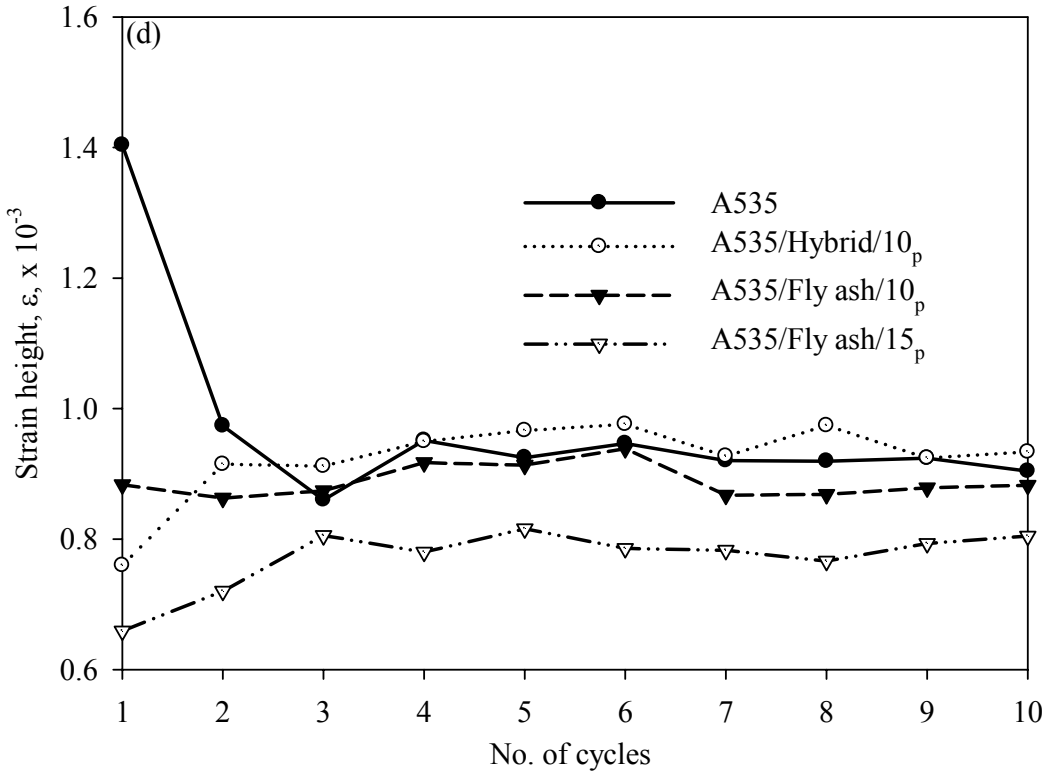

Figure 4.8 continues.

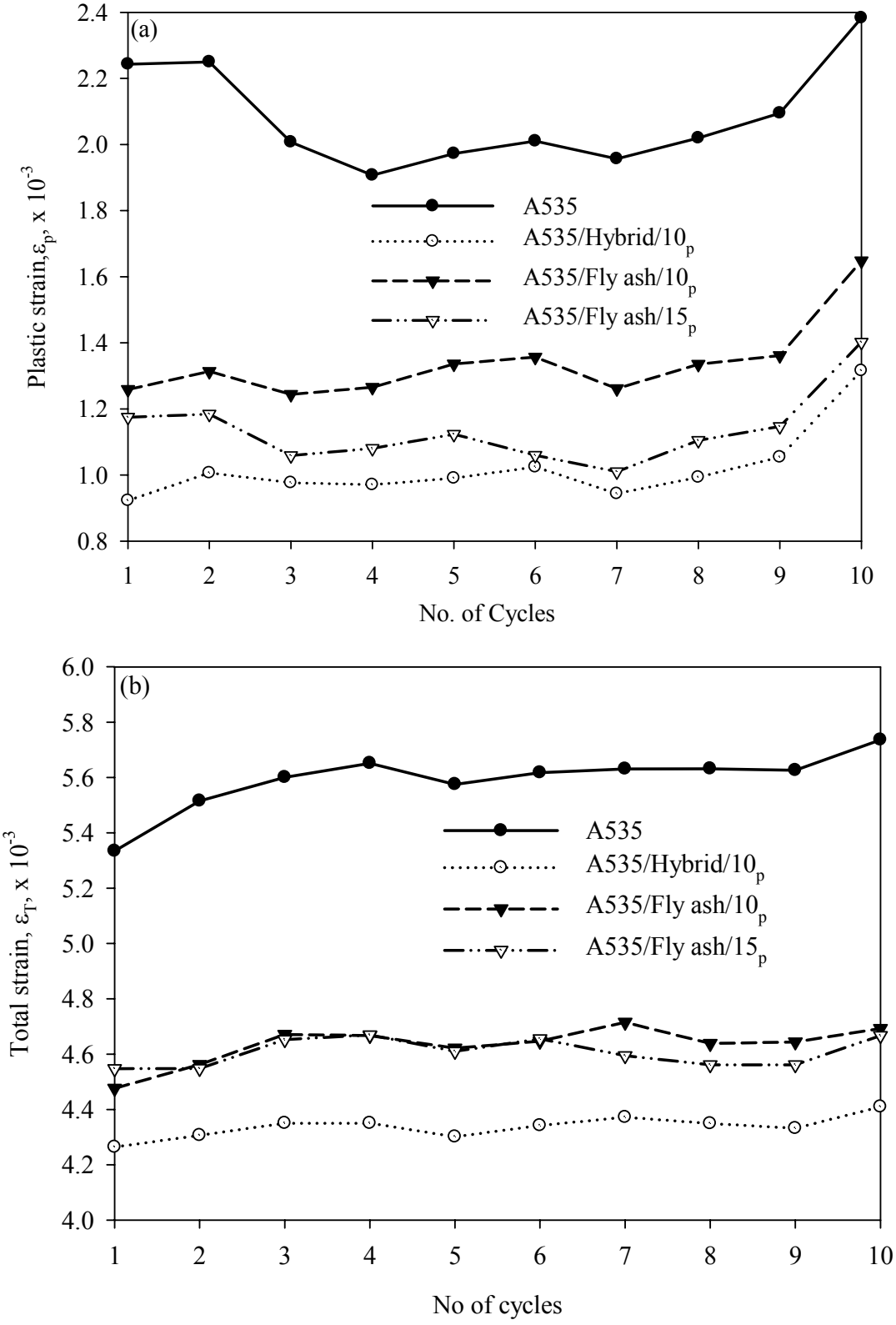

Figure 4.9. ε_p, ε_T, ε_c and $\Delta\varepsilon$ obtained for the test materials as a function of number of cycles obtained from the strains computed by Setsoft 2000 software.

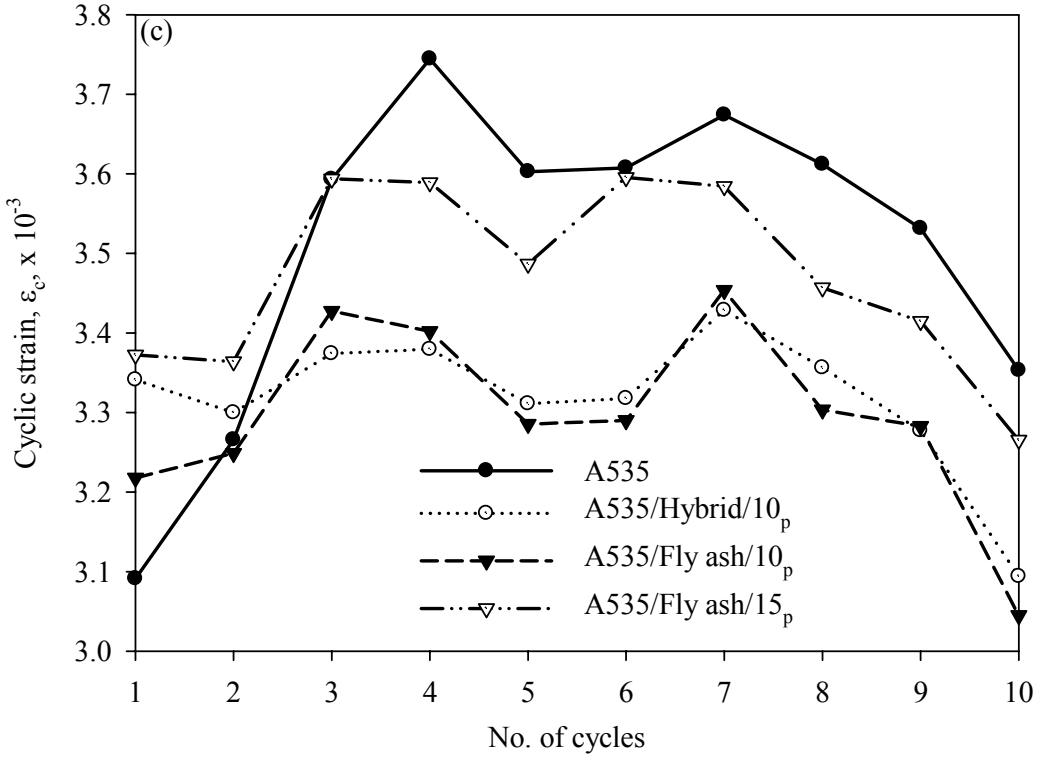

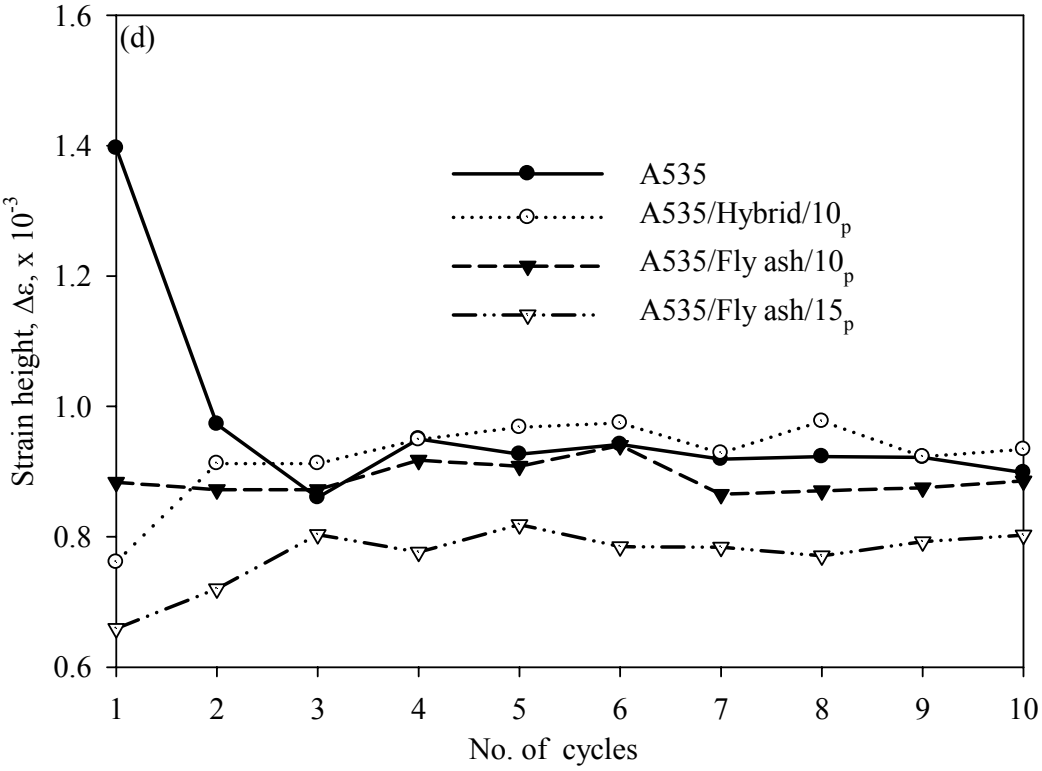

Figure 4.9 continues.

equipment made it difficult to acquire data below this temperature. This lag can be correct for by running the experiment with cooling water at about 50 ^{o}C. As shown in Figure 4.9(a) for the alloy, ε_p generally decreased between the first and fourth cycles, increased slowly between the fourth and ninth cycles and sharply after the ninth cycle. The initial decrease in ε_p for A535 alloy contradicts the results obtained by Zhang *et al.* [65] for an Al-Si alloy and that by Huang *et al.* [66] for an $AlSi_{12}CuMgNi$ alloy. The decrease in ε_p could be attributed to decrease in the induced thermal stress during cooling from maximum cycling temperature of the alloy after the first cycle. This effect was observed by Zhang *et al.* [65] in Al-Si alloy after the first few cycles. However, the accumulated thermal stress in A535 was enough to initiate plastic deformation of the matrix after the fourth cycle. For the MMCs, their ε_p was less than that of the alloy. It also remained virtually unchanged up to the ninth cycle when it increased sharply. This indicates that the addition of ceramic particles to A535 improved its dimensional stability. It can also be seen that the hybrid composite has the lowest ε_p, suggesting that SiC is more effective in improving the dimensional stability of the alloy than fly ash.

Figure 4.9(b) shows that ε_T of the alloy and the MMCs increased slowly up to the fourth thermal cycle and remained practically unchanged up to the tenth cycle. This can be attributed to the ε_c of these materials, which increased sharply in the first four cycles before decreasing in the subsequent cycles (see Figure 4.9(c)). In Figure 4.9(d), it can be seen that the $\Delta\varepsilon$ for A535 decreased in the first three cycles, but remained about the same in the subsequent cycles. This indicates a decrease in the size of hysteresis loops induced in the alloy which, in turn, points to relaxation of the thermal stresses induced in it. This rationalizes the observed decrease in its CTE during the re-heat cycle (see Figure 4.4(a)). Also, in Figure 4.9(d), it can be seen that $\Delta\varepsilon$ for A535/Hybrid/10_p and A535/Fly ash/15_p composites increased between the first and second cycles, while that for A535/Fly ash/10_p remained about the same. This indicates an increase in thermal stress induced in A535/Hybrid/10_p and A535/Fly ash/15_p composites and stress relief in A535/Fly ash/10_p between those cycles and, as such, agrees with the earlier reason for the observed CTE of the composites during the second thermal cycle (see Figures 4.4(b)-(d)).

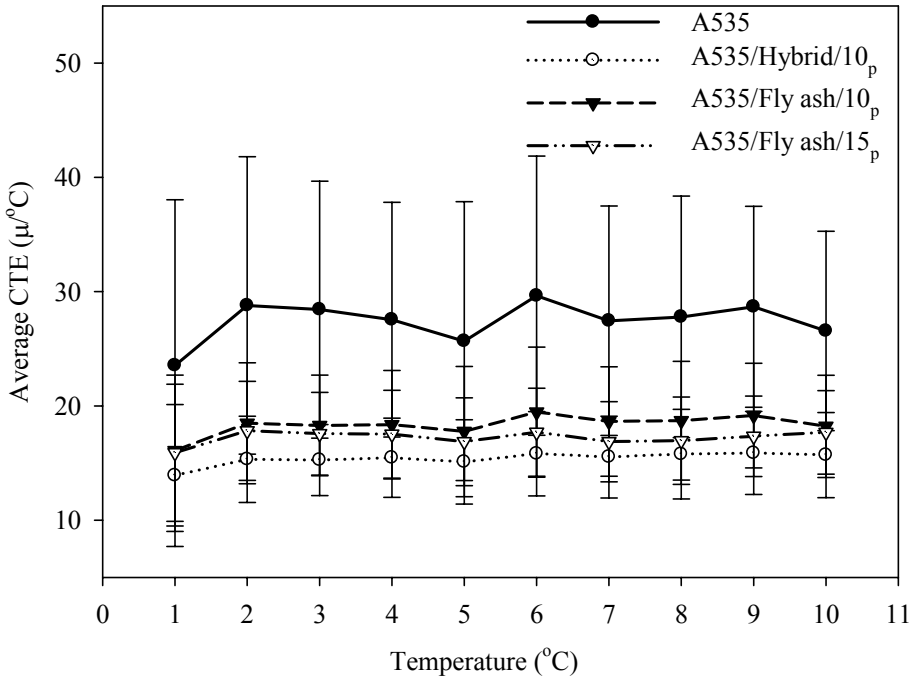

Figure 4.10. Average CTE versus number of thermal cycles obtained for A535 and the composites. The error bars are based on standard deviation.

Figure 4.10 shows the average CTE of A535 and its MMCs as a function of number of thermal cycles. The average CTEs were calculated by determining the average of the average CTEs of the test samples in each cycle as expressed in equation (4.5). It can be seen that the CTEs of the test materials increased within the first two cycles after which it remained virtually unchanged as the number of cycles increased. A similar trend was observed by Chen *et al.* [80] for Al-50 vol.% SiC MMCs. Also, it can be seen that the MMCs showed lower CTE than the alloy during the thermal cycles. This is a clearly shows that the addition of ceramic particles to A535 made it more dimensionally stable.

$$\overline{\text{CTE}} = \frac{\text{Sum of the average CTEs}}{\text{Total number of data points}} \tag{4.5}$$

Figure 4.11 shows the change in length (displacement) of A535 and the composites after CTE and thermal cycling measurements. The displacement was calculated from the difference between the initial and final lengths of the sample. The initial and final lengths were measured using micrometer screw gauge. It can be seen from

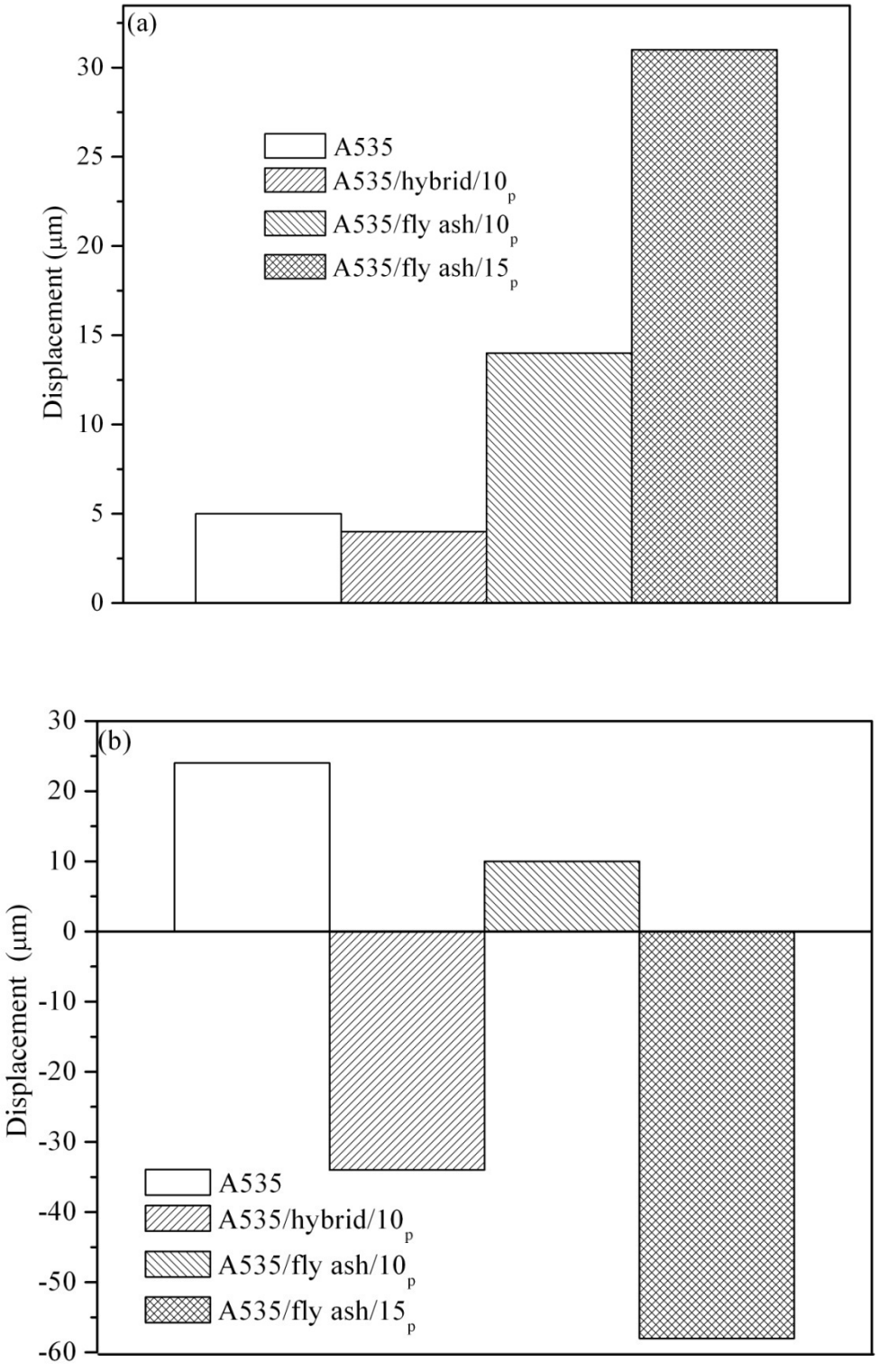

Figure 4.11. Thermal displacement obtained for A535 and its composites after (a) CTE and (b) thermal cycling experiments using the micrometer screw gauge.

Figure 4.11(a) that the length of A535 sample increased with the addition of ceramic reinforcement. Also, it can be seen from Figure 4.11(b) that after 10 cycles, A535 and A535/Fly ash/10_p showed a cumulative positive displacement, while cumulative displacement for A535/Hybrid/10_p and A535/Fly ash/15_p were negative.

4.2 Reactivity in A535 MMCs

The microstructural examination of A535 and Differential Scanning Calorimetry (DSC) study of A535 and its MMCs are presented in this section. The DSC study was also used to examine if the oscillations observed in the CTEs were due to phase transformation or stress relaxation.

4.2.1 Microstructural Examination of A535

Optical micrographs of A535 in the as-received and annealed conditions are shown in Figures 4.12 and 4.13, respectively. It can be seen that the microstructure of the alloy consists of various phases such as those labeled *a*, *b*, and *c*, which were formed when the alloy was fabricated. To further understand these phases, as-received and annealed samples of A535 were analyzed in an SEM equipped with an EDS system as explained in Chapter 3.

Figures 4.14 and 4.15 show respectively SEM micrographs and EDS spectra of the phases labeled *a*, *b*, and *c* in Figures 4.12 and 4.13. A summary of the elemental compositions of these phases are shown in Table 4.2. Si and Mn were not considered in determining the likely phases of phases *b* and *c* in that they are contributions from the surrounding materials. The likely phases were determined by calculating the relative atomic percentages of the elements present in the phases and comparing it with those in phases that has been reported in the open literature. The presence of phases *a* and *c* in A535 has been reported in reference [16]. Fasoyinu *et al.* [6] reported the presence of dark phases and interdentritic networks in A535, which they identified as $FeAl_3$ and Mg_2Al_3 phases, respectively.

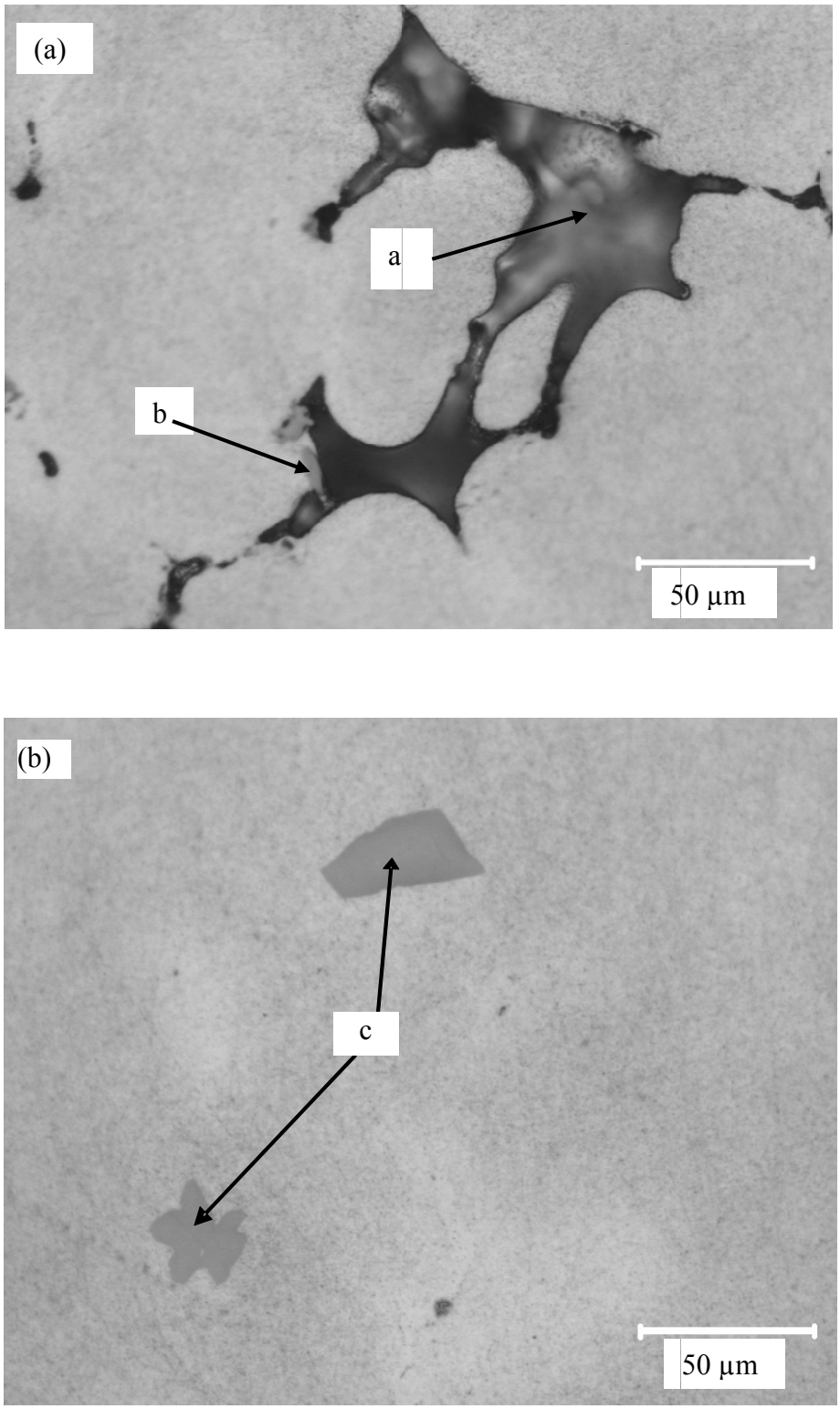

Figure 4.12. Typical optical micrographs of as-received A535 showing the various phases present in it.

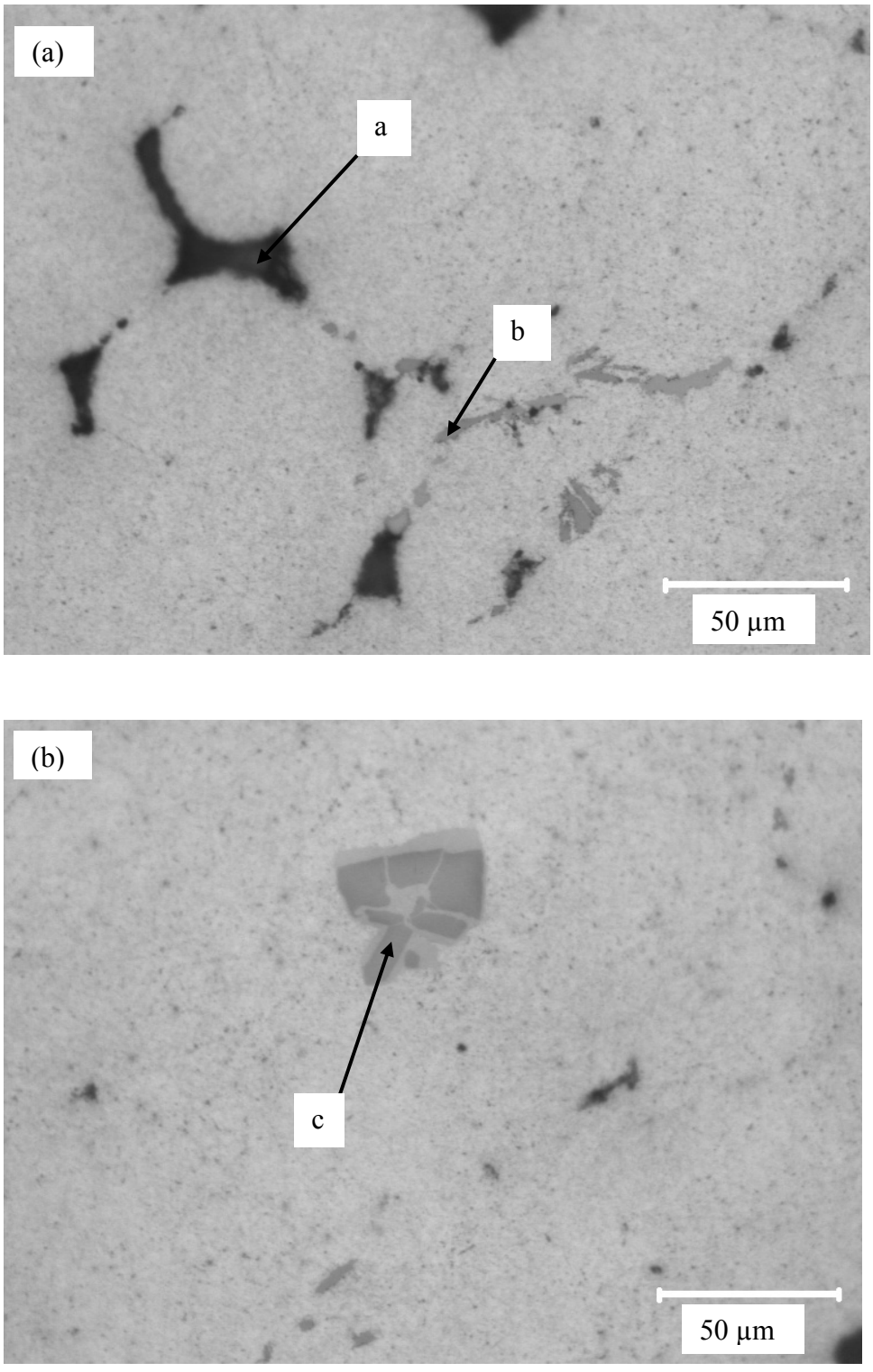

Figure 4.13. Typical optical micrograph of heat treated A535 showing the various phases present in it.

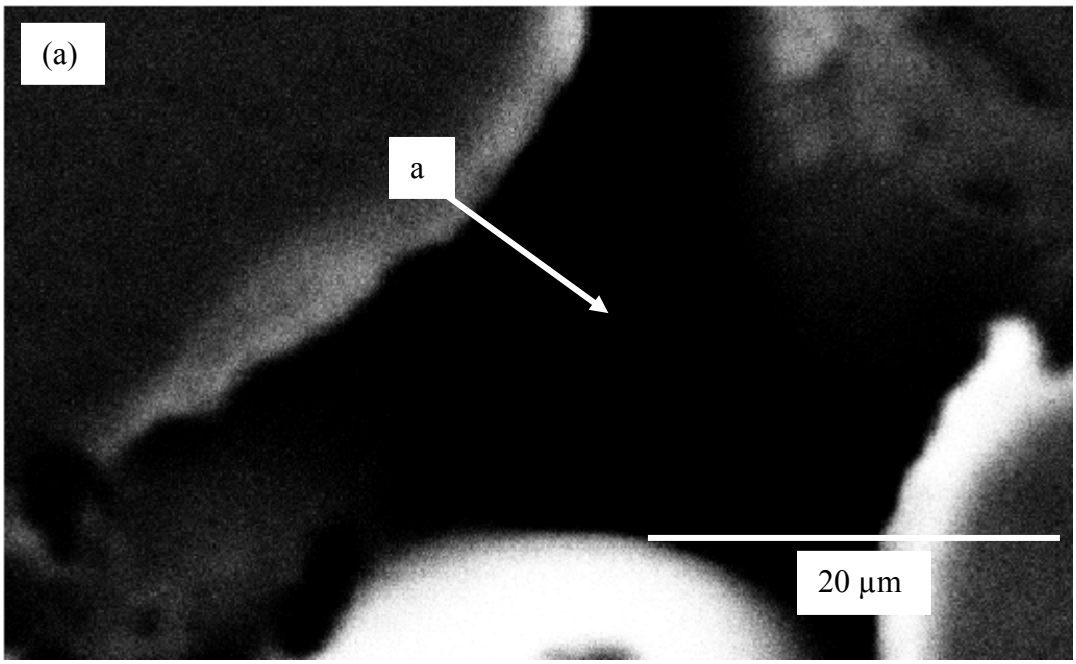

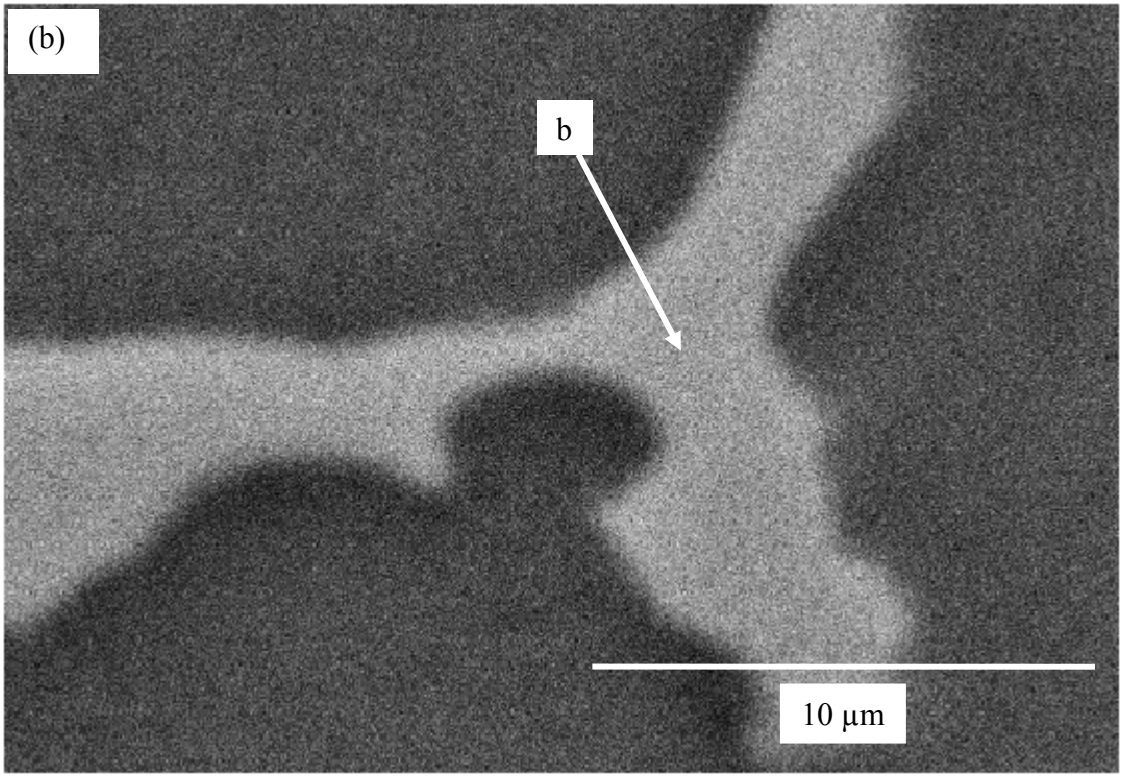

Figure 4.14. Typical SEM micrographs of the phases labeled a, b, and c in Figures 4.12 and 4.13.

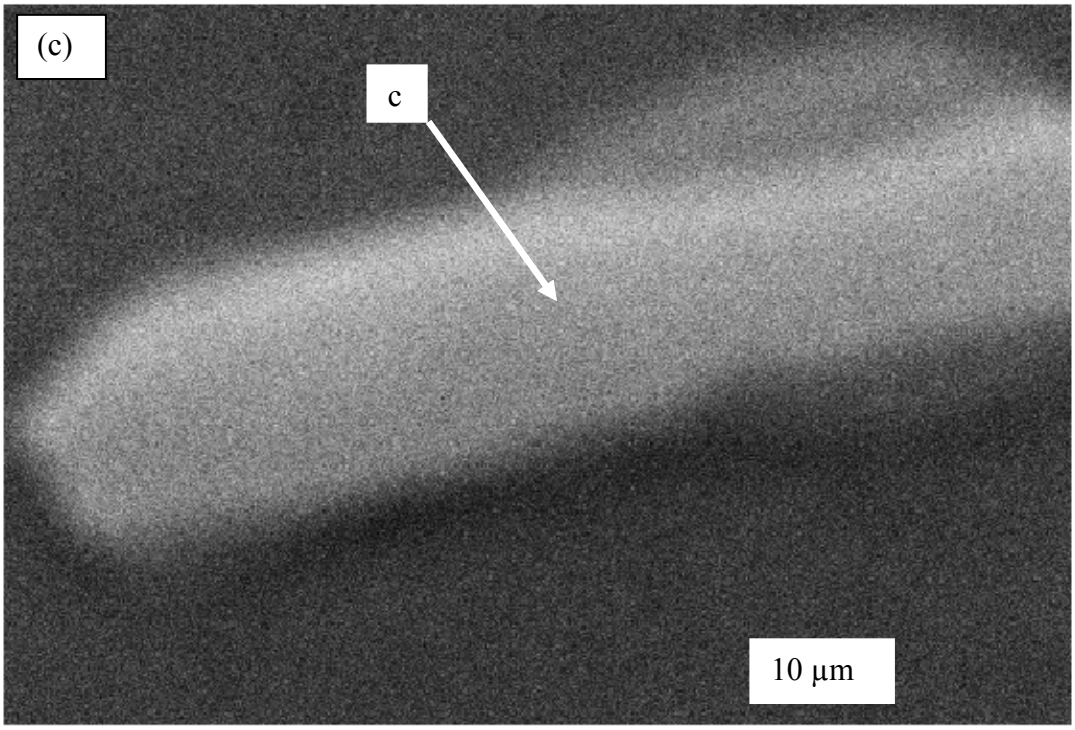

Figure 4.14 continues.

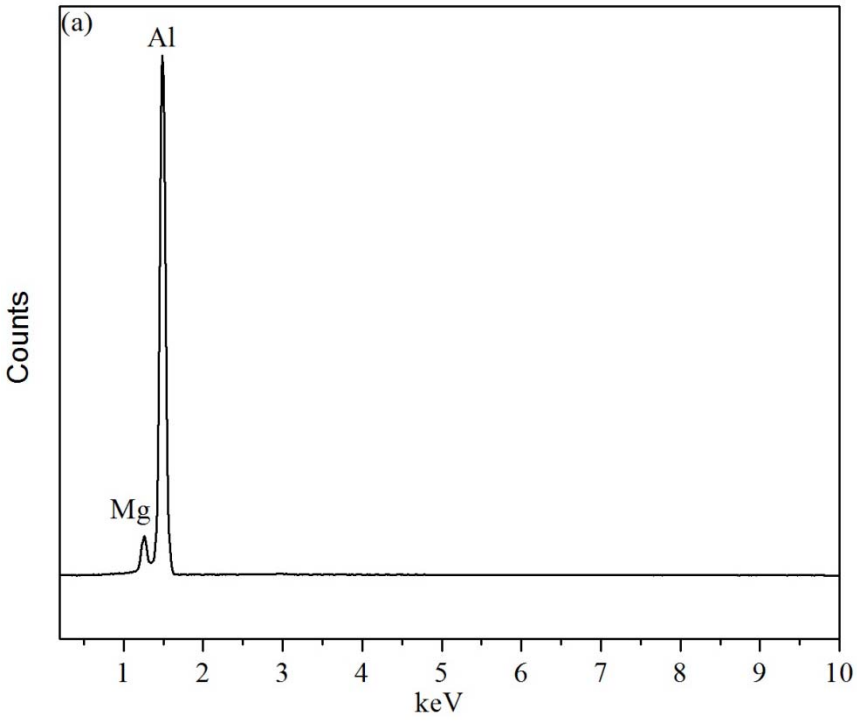

Figure 4.15. Typical EDS spectra obtained from the phases labeled *a*, *b*, and *c* in Figures 4.12 and 4.13.

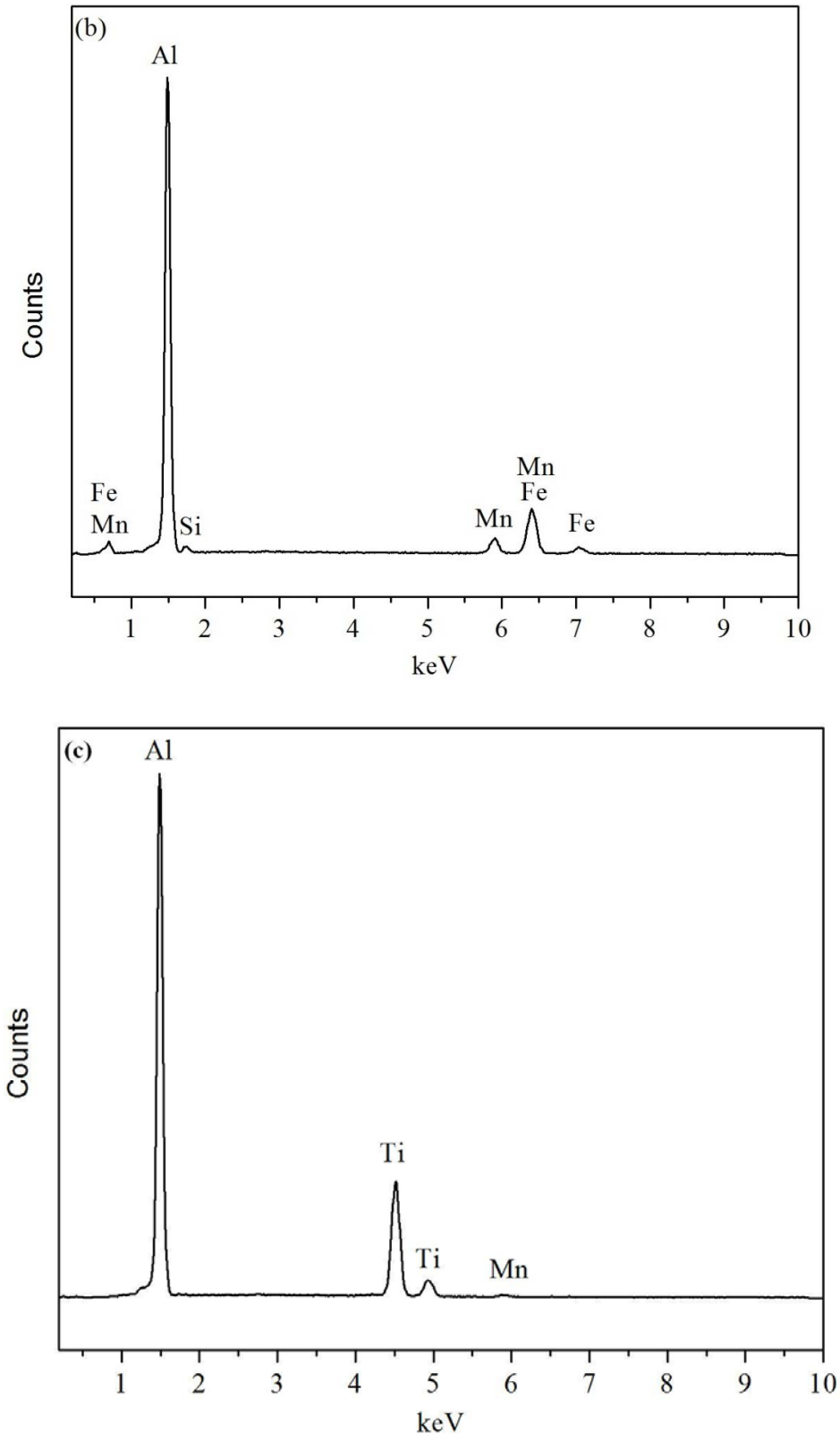

Figure 4.15 continues.

Table 4.2. Elemental compositions of the phases labeled *a*, *b*, and *c* in Figures 4.12 and 4.13.

Phase label	Elements (wt.%)						
	Al	Mg	Si	Mn	Fe	Ti	Likely phase
A	92.11	7.89	---	---	---	---	Mg_2Al_3
B	64.12	---	1.48	7.54	26.86	---	$Al_{8.3}Fe_{3.5}Mn$
C	59.24	---	---	0.75	---	40.01	Al_3Ti

4.2.2 DSC Study of reactivity in A535 and its MMCs

Figure 4.16(a) shows typical DSC thermograms obtained for A535, high-purity aluminium and magnesium in the temperature range 100 to 750 ^oC. The expanded views of the different sections of the thermograms are shown in Figures 4.16(b) and (c), while Table 4.3 summarizes the average peak temperature of the reactions labeled *a* and *b* in the materials. The data below 100 ^oC and above 750 ^oC were not presented because of thermal lag in the DSC equipment during measurements (see Chapter 3). As can be seen from Figure 4.16(b), the peak of the endothermic reaction labeled *a* occurred at about 464 ^oC in A535. The temperature range in which this endothermic process occurred is covers the temperature where β-phase (Mg_2Al_3) dissolves in binary Al-16 at.% Mg alloy [105]. The presence of β-phase was also reported in reference [6]. On the basics of these two literature results, it can be concluded that peak *a* is due to the dissolution of β-phase. It can also be seen from Figure 4.16(c) that another endothermic peak labeled *b* occurred in A535 at about 647 ^oC. This peak is due to melting of the alloy as it occurred within the same temperature range as those of high purity aluminium and magnesium (see Table 4.3), which are its main constituent elements.

Figure 4.17(a) shows typical DSC thermograms of A535 and its composites, while Figures 4.17(b) and (c) and (d) show the expanded views of the thermograms. Table 4.4 summarizes the average peak temperatures of reactions *b* and *c* as well as their enthalpies. Figure 4.17(b) shows peaks, with low enthalpies, in the thermograms.

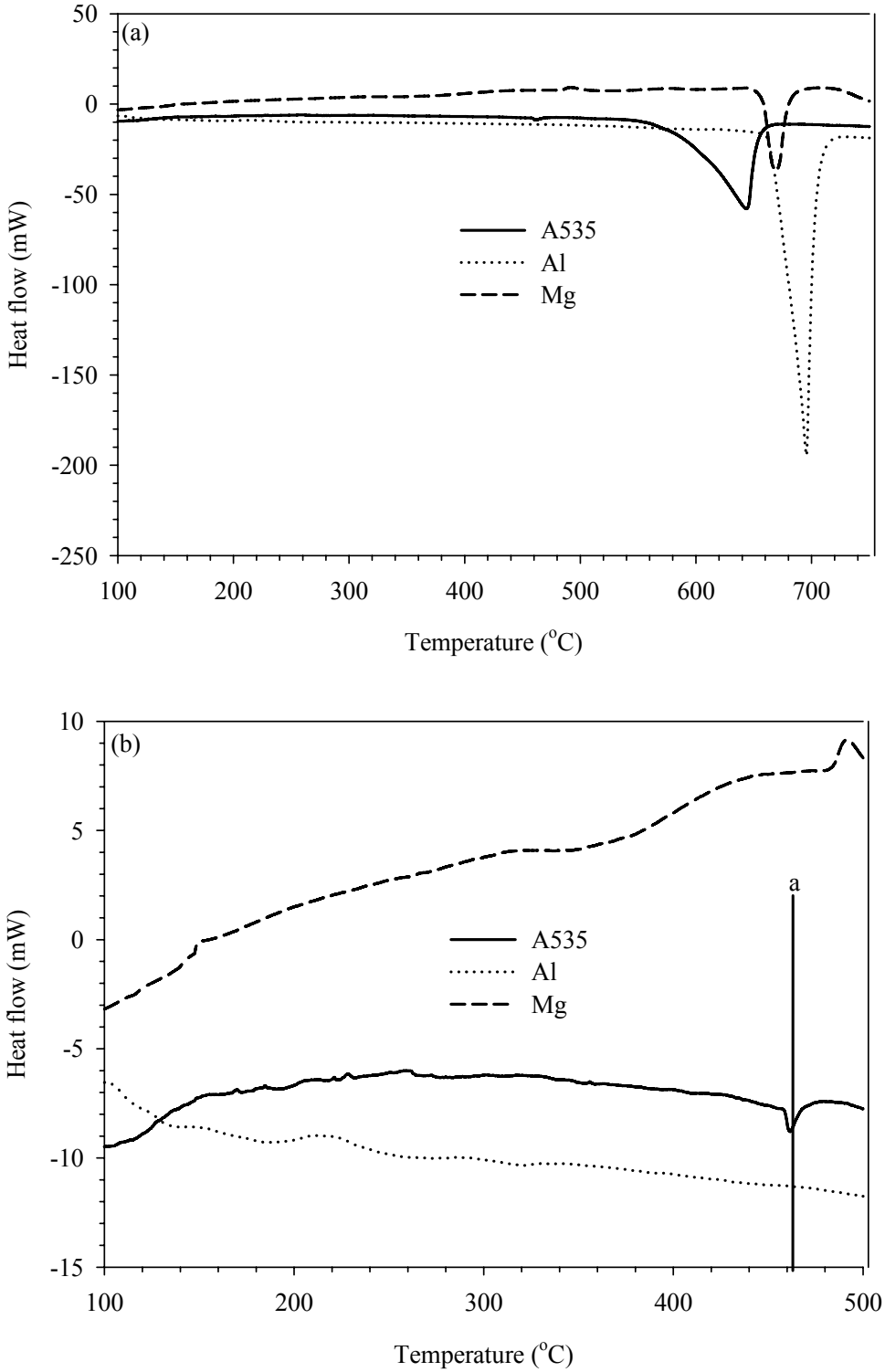

Figure 4.16. Typical DSC thermograms obtained for A535, Al and Mg on heating from 100 to 750 °C: The (a) complete thermographs, and its expanded views between (b) 100 and 500 °C and (c) 500 and 750 °C.

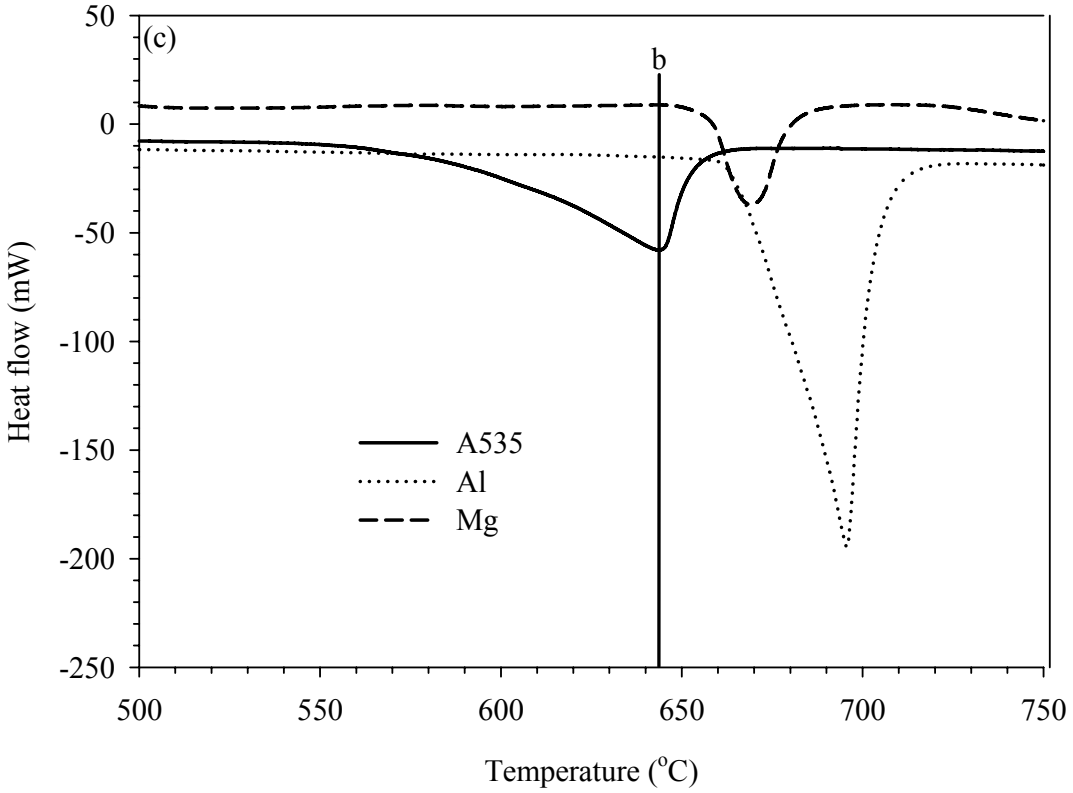

Figure 4.16 continues.

Table 4.3. Average peak reaction temperatures and enthalpies of peaks labeled *a* and *b* in Figure 4.16.

Materials	Peak *a* Peak temp (°C)	Peak *b* Peak temp. (°C)
A535	460.4±1.47	645.2±2.47
Mg	---	673.1±2.05
Al	---	692.3±2.68

*The accuracy of the temperature measurements is based on standard deviation.

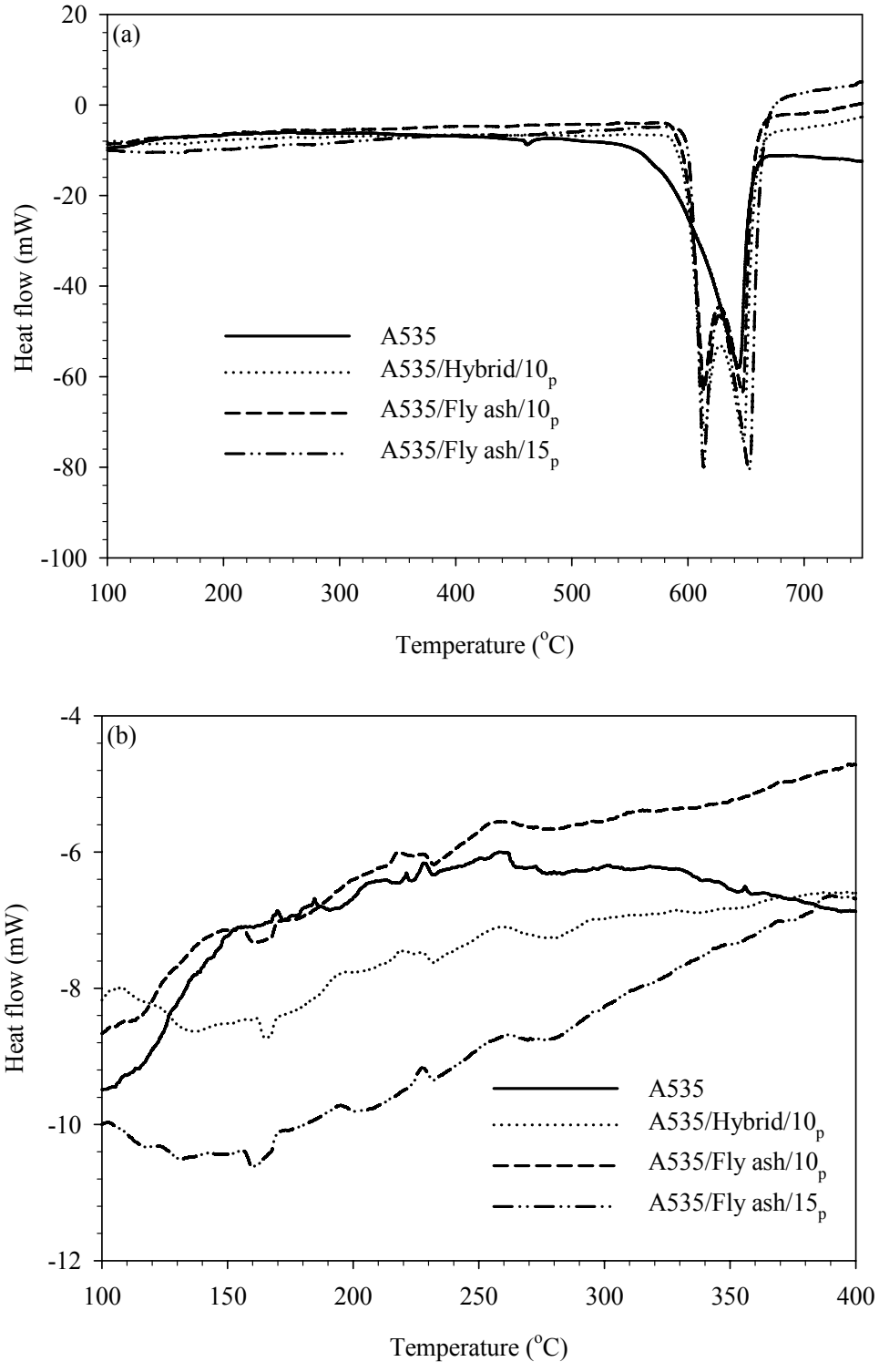

Figure 4.17. Typical DSC thermograms obtained for A535 and its composites on heating from 100 to 750 °C: The (a) complete thermograms, and its expanded views between (b) 100 and 400 °C, (c) 400 and 500 °C and (d) 500 and 750 °C.

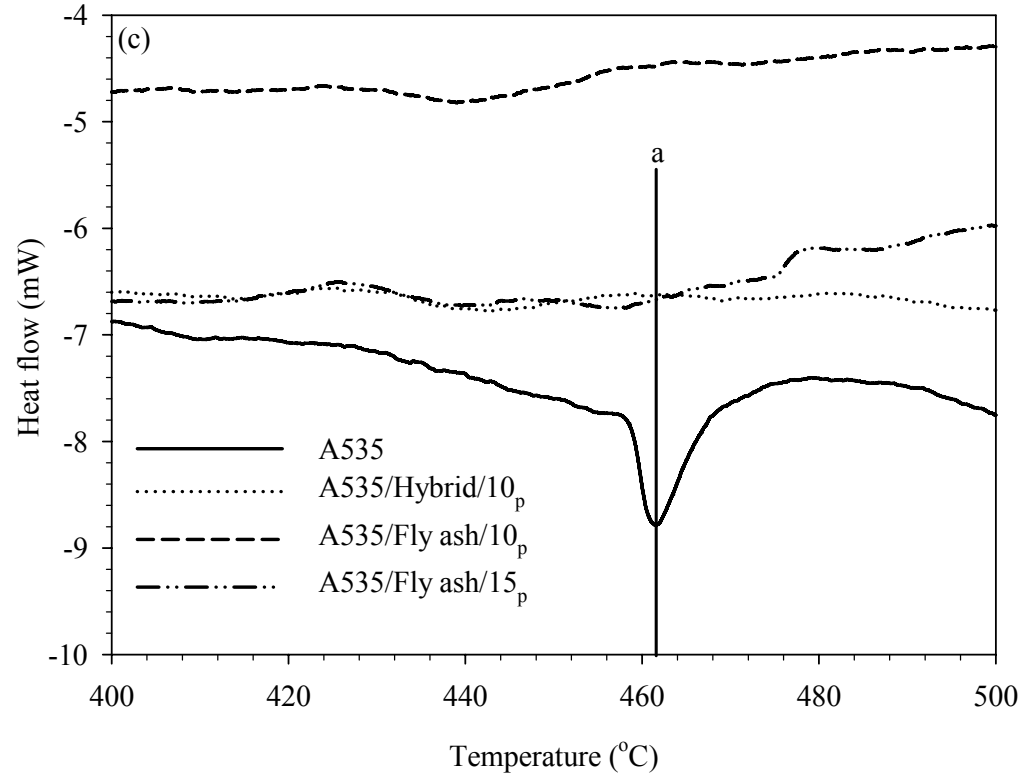

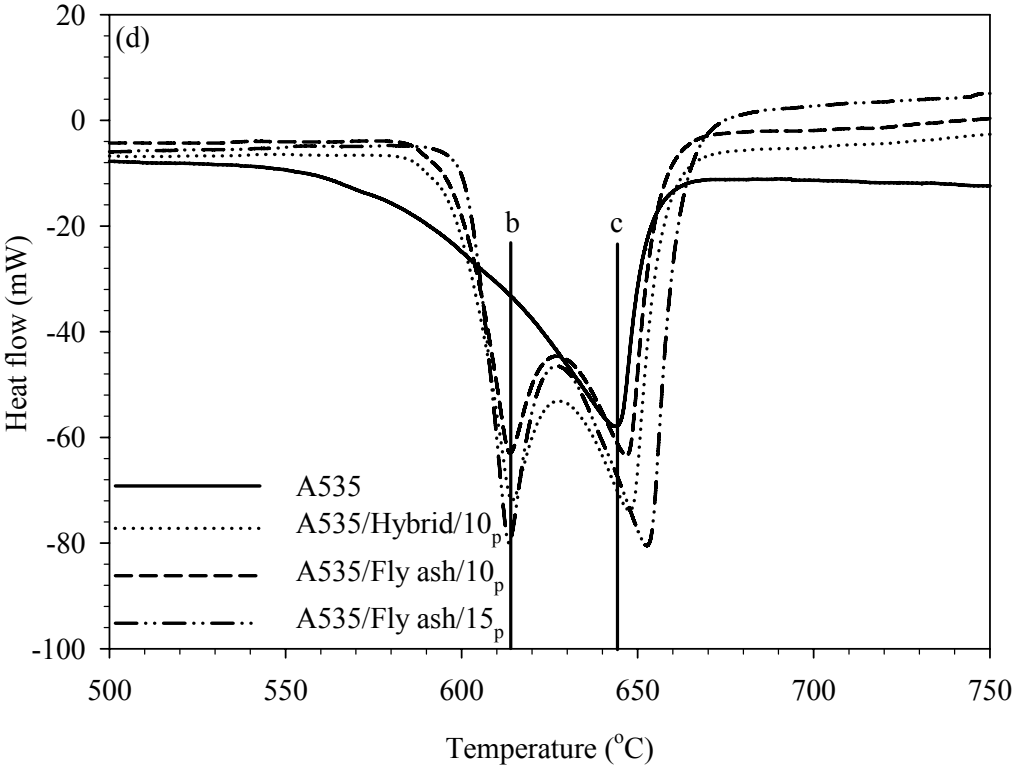

Figure 4.17 continues.

Table 4.4. Average peak reaction temperatures and enthalpies of reactions labeled *b* and *c* in Figure 4.17.

Materials	Peak *b* Peak temp. (^oC)	Enthalpy of peaks *b* (kJ/Kg)	Peak *c* Peak temp. (^oC)	Enthalpy of peak *c* (kJ/Kg)
A535	---	---	645.2±2.47	313.5±9.8
A535/Hybrid/10_p	613.6±0.57	19.0±2.90	647.0±1.13	37.5±9.12
A535/Fly ash/10_p	616.6±0.21	32.3±1.98	648.6±0.34	19.0±2.90
A535/Fly ash/15_p	613.6±0.49	562.2±4.95	652.9±0.14	63.2±3.82

*The accuracy of the temperature and enthalpy measurements is based on standard deviation.

The presence of these peaks in the thermograms suggests that either different phases formed and dissolved in the samples or stresses relaxed as temperature increased. It can be seen that the peak *a* did not occur in the composites, suggesting that fly ash inhibits the dissolution of *β*-phase in A535. In Figure 4.17(d), the endothermic reaction labeled *b* can be seen in the MMCs between 580 and 626.8 ^oC. This peak is most likely due to an endothermic dissolution reaction in the composites.

Figure 4.18(a) shows the DSC thermograms of A535 and the composites when cooled from 750 to 100 ^oC. The expanded views of different sections of the figure are shown in Figures 4.18(b) and (c). Table 4.5 shows the average peak reaction temperatures of reactions *b*' and *c*' as well as their formation enthalpies. It can be seen from Figure 4.18(b) that some of the phase changes that occurred during heating did not reoccur during cooling. This can be discerned from the absence of reactions such as "*a*" in Figures 4.16 and 4.17. In Figure 4.18(c), it can be seen that the samples solidified between 515 and 630 ^oC during cooling. These crystallization temperatures are less than the dissolution temperatures obtained during heating.

Figure 4.19(a) shows the DSC thermograms of A535 and the composites co-plotted with that of fly ash for samples heated from 100 to 750 ^oC, while Figures 4.19(b)-(d) show the expanded views of different sections of Figure 4.19(a). As can be seen, fly ash showed no detectable reaction peak in the temperature range studied. This suggests that reaction *b* is not from fly ash. Therefore, it can then be concluded that it is due to the

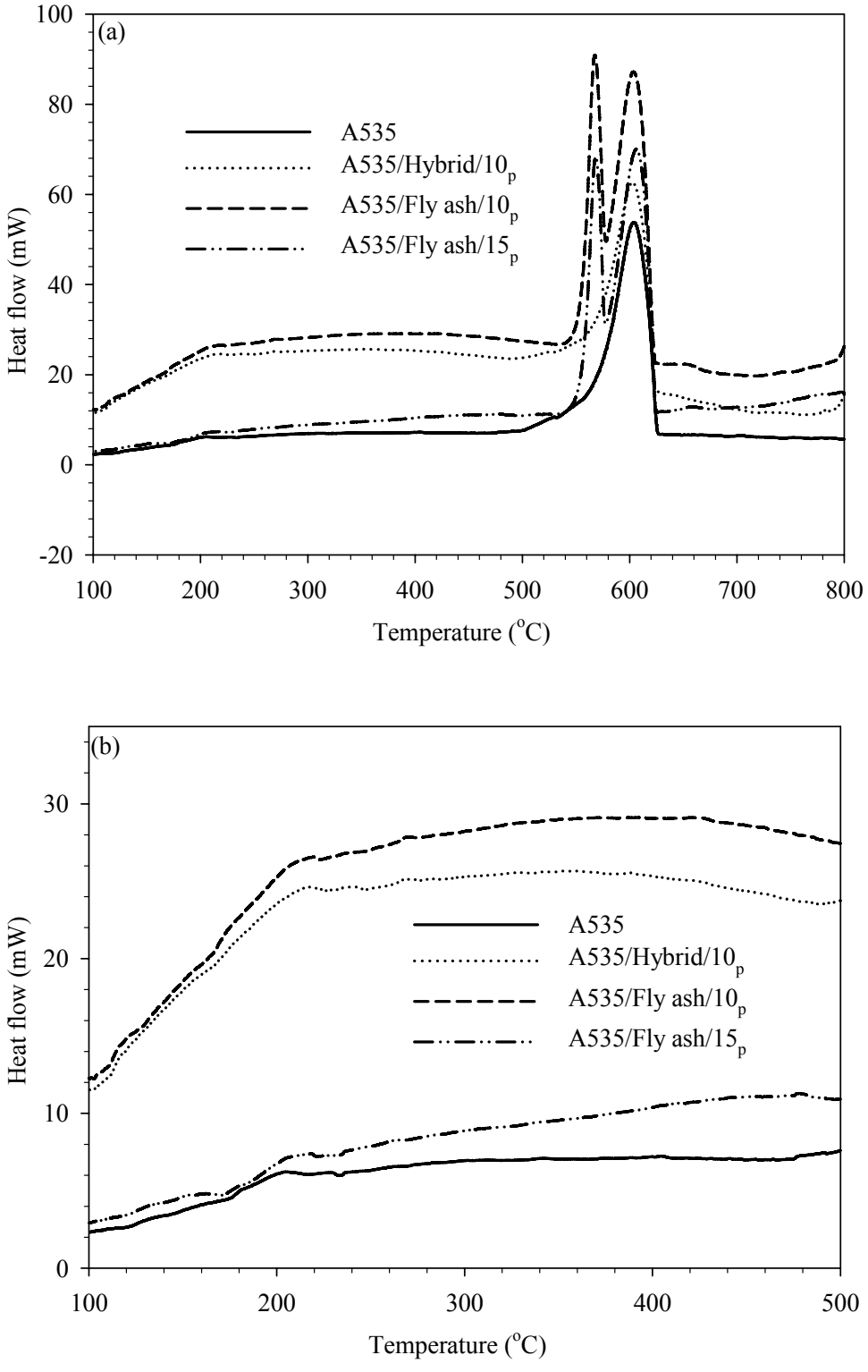

Figure 4.18. Typical DSC thermograms obtained for A535 and its MMCs on cooling from 750 to 100 °C: (a) The complete thermograms, and its expanded views between (b) 100 and 500 °C and (b) 500 and 750 °C.

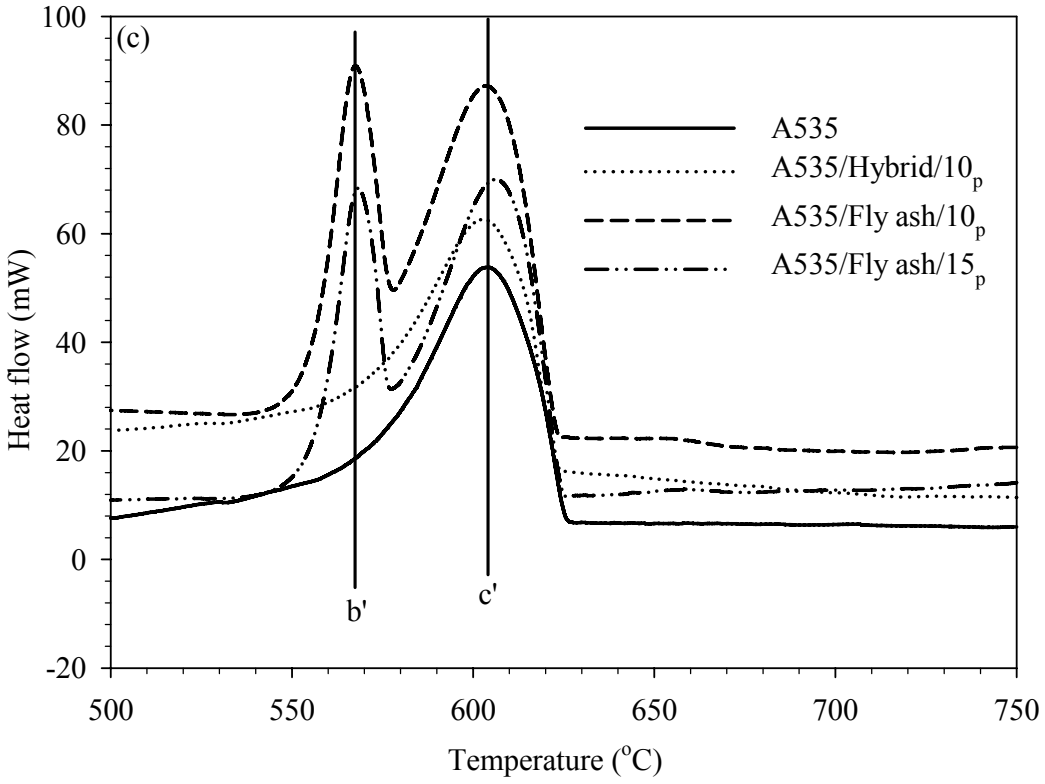

Figure 4.18 continues.

Table 4.5. Average peak reaction temperatures and enthalpies of the peaks labeled *b′* and *c′* in Figure 4.18.

Materials	Peak *b*' Peak temp. (°C)	Enthalpy of peaks *b*' (kJ/Kg)	Peak *c′* Peak temp. (°C)	Enthalpy of peaks *c*' (kJ/Kg)
A535	---	-	603.6±0.7	308.6±2.1
A535/Hybrid/10_p	---	---	606.8±2.5	135.8±2.0
A535/Fly ash/10_p	567.2±2.7	13.3±11.0	606.1±1.2	214.9±39.3
A535/Fly ash/15_p	562.2±5.0	23.05±0.9	606.5±0.0	178.5±1.3

*The accuracy of the measurements is based on standard deviation.

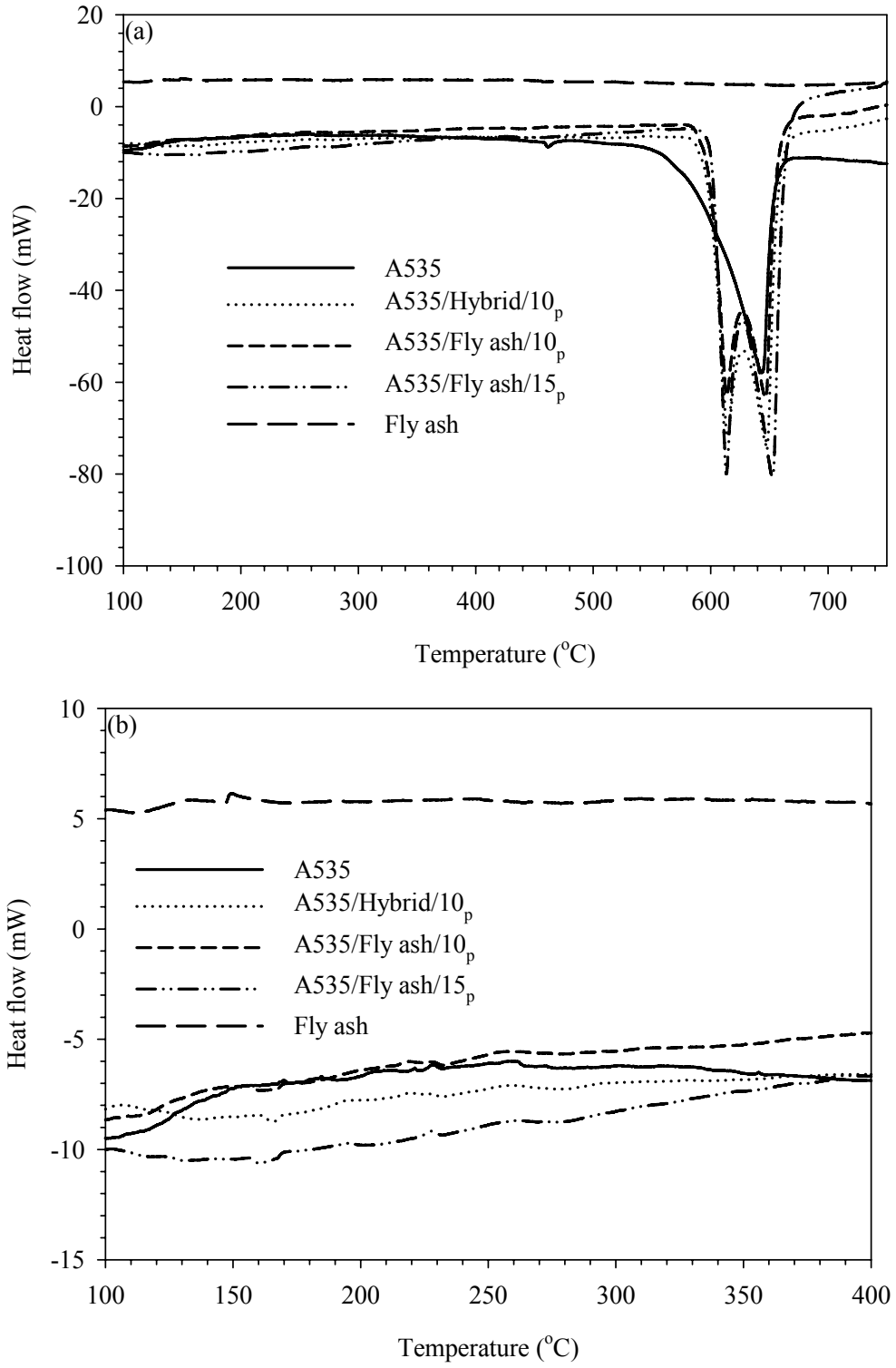

Figure 4.19. Typical DSC thermograms of A535 and its composites compared with that of fly ash on heating from 100 to 750 °C: (a) The complete thermograms, and its expanded views between (b) 100 and 400 °C, (c) 400 and 500 °C and (d) 500 and 750 °C.

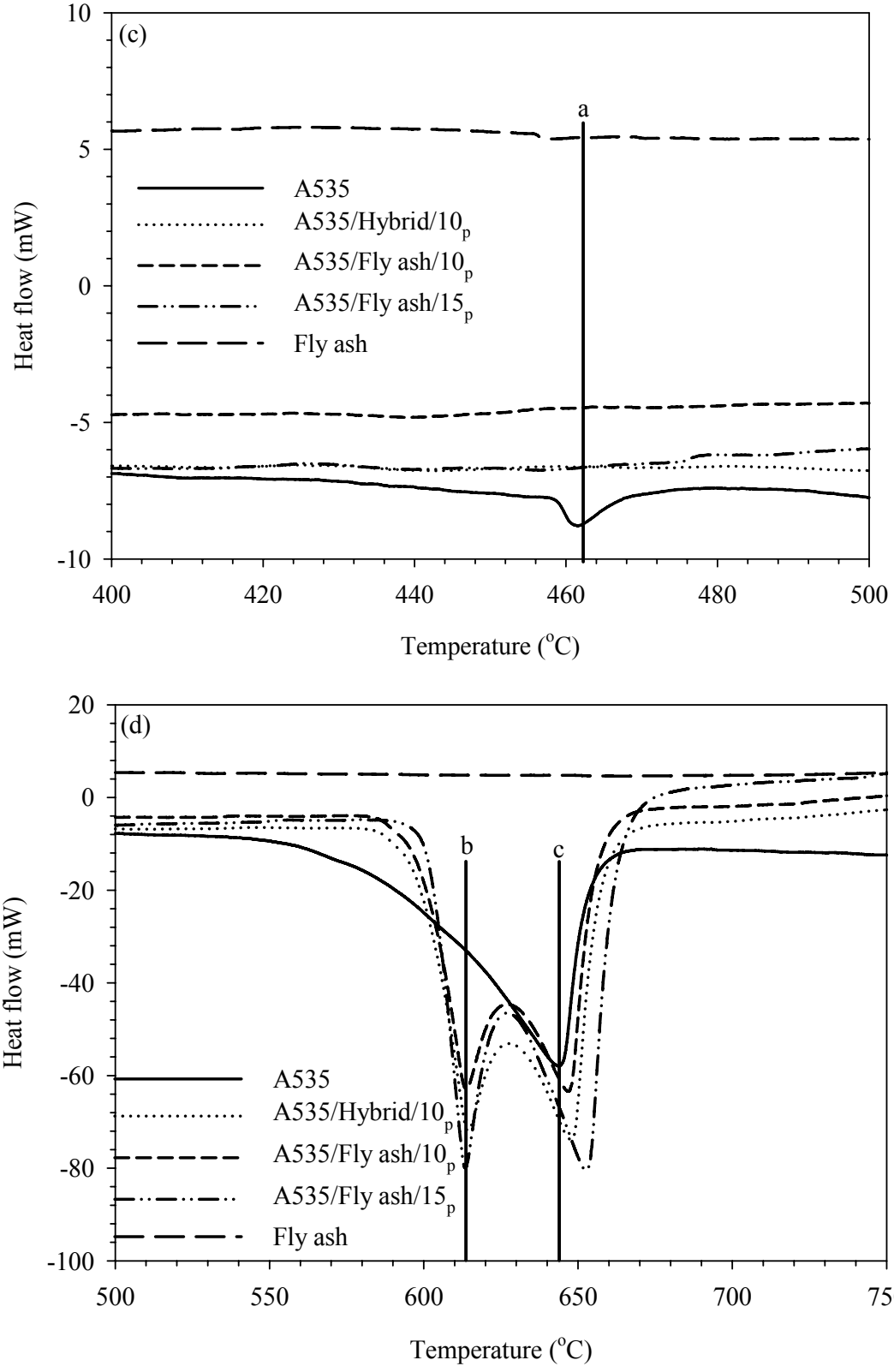

Figure 4.19 continues.

dissolution of the phase that formed between fly ash and A535 during fabrication.

Figure 4.20(a) shows the thermograms of A535 and the composites co-plotted with that of Al-Mg mixture, while the exploded views of the different sections of the figures are shown in Figures 4.20(b)-(d). It can be seen from Figures 4.20(b) and (c) that none of the peaks obtained between 100 and 500 ^{o}C for A535 and the composites matches those in the mixture. In Figure 4.20(d), the endothermic reaction between 612 and 665 ^{o}C in the mixture could be attributed to the melting of aluminium and magnesium as they have very close melting temperatures [7]. This peak does not match with peak *b* in the composites. Hence, it eliminates phase transformation in the Al-Mg mixture sample as its possible cause.

Figure 4.21(a) shows the thermograms of A535 and the composites co-plotted with that of Al-Mg-fly ash mixture on heating from 100 to 750 ^{o}C and Figures 4.21(b)-(d) show the exploded views of various sections of the figure. As can be seen in Figure 4.21, the thermogram of the mixture shows that an endothermic phase change occurred at 658 ^{o}C, which is about 15 ^{o}C more than the melting temperature of the A535 MMC reinforced with 15 wt.% fly ash. This peak is most likely due to melting of either aluminium or magnesium in the mixture and the differences observed between the peak positions of the mixture and A535 could be attributed to the presence of other alloying elements in A535. Another prominent endothermic reaction peak can be seen in the mixture at 607 ^{o}C, which is about 7 ^{o}C less than that of reaction peak *c* in the MMCs. This slight difference in the peak positions could be attributed to the presence of other elements in the alloy which are not in the mixture.

The thermograms of A535, its MMCs and Al-Mg-fly ash mixture on cooling from 750 to 100 ^{o}C are shown in Figure 4.22(a). The expanded views of the figure are shown in Figure 4.22 (b) and (c). It can be seen from the figures that exothermic reactions b' and c' occurred in the mixture at about 525 and 604 ^{o}C, respectively. The peak labeled c in the mixture is due to solidification of aluminium. The peak labeled b' at about 525 ^{o}C in the mixture shows that the reaction that occurred during heating (see Figure 4.21(c))

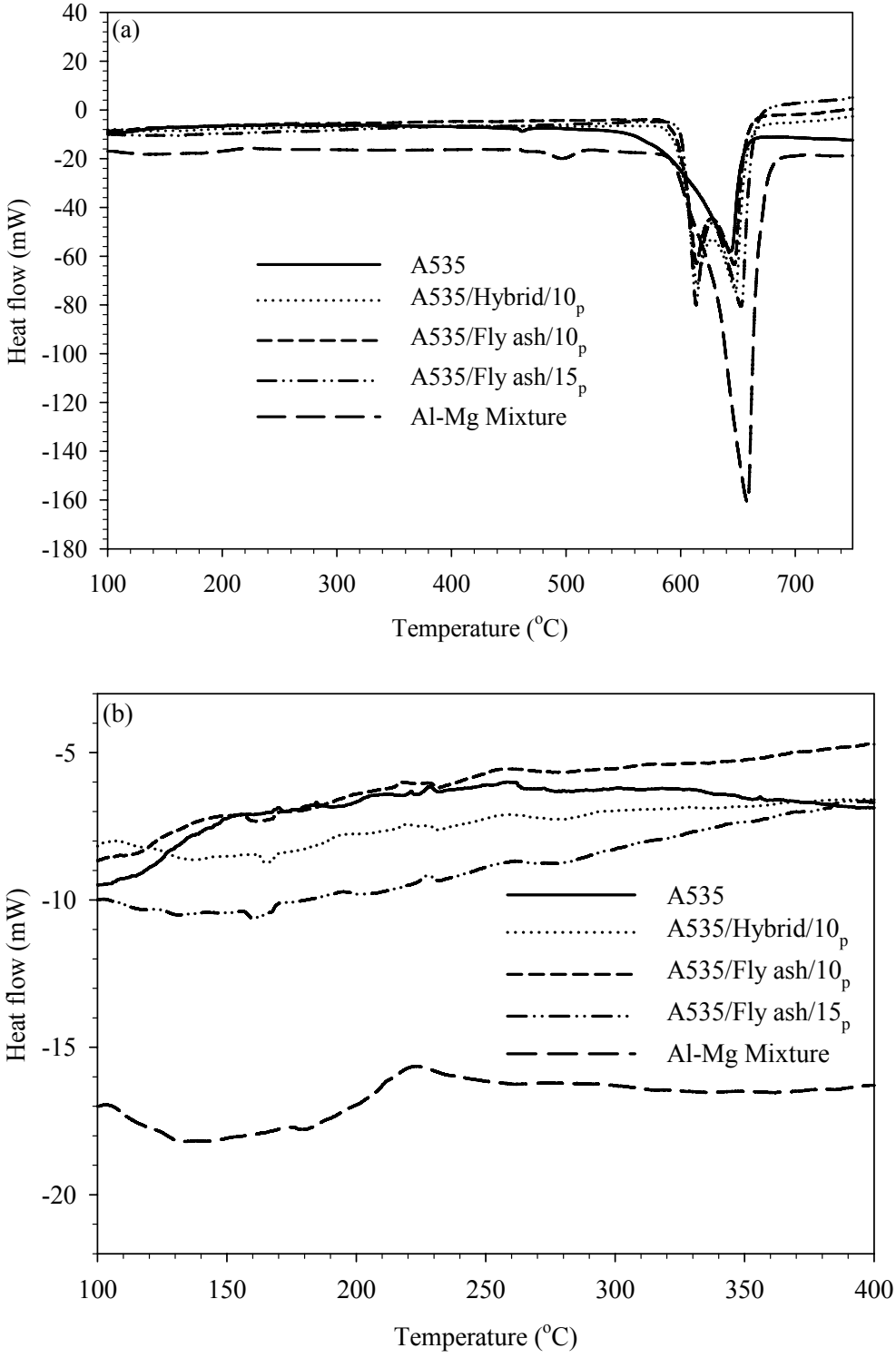

Figure 4.20. Typical DSC thermograms of A535 and its composites compared with that of Al-Mg mixture on heating from 100 to 750 °C: (a) The complete thermograms, and its expanded views between (b) 100 and 400 °C, (c) 400 and 500 °C and (d) 500 and 750 °C.

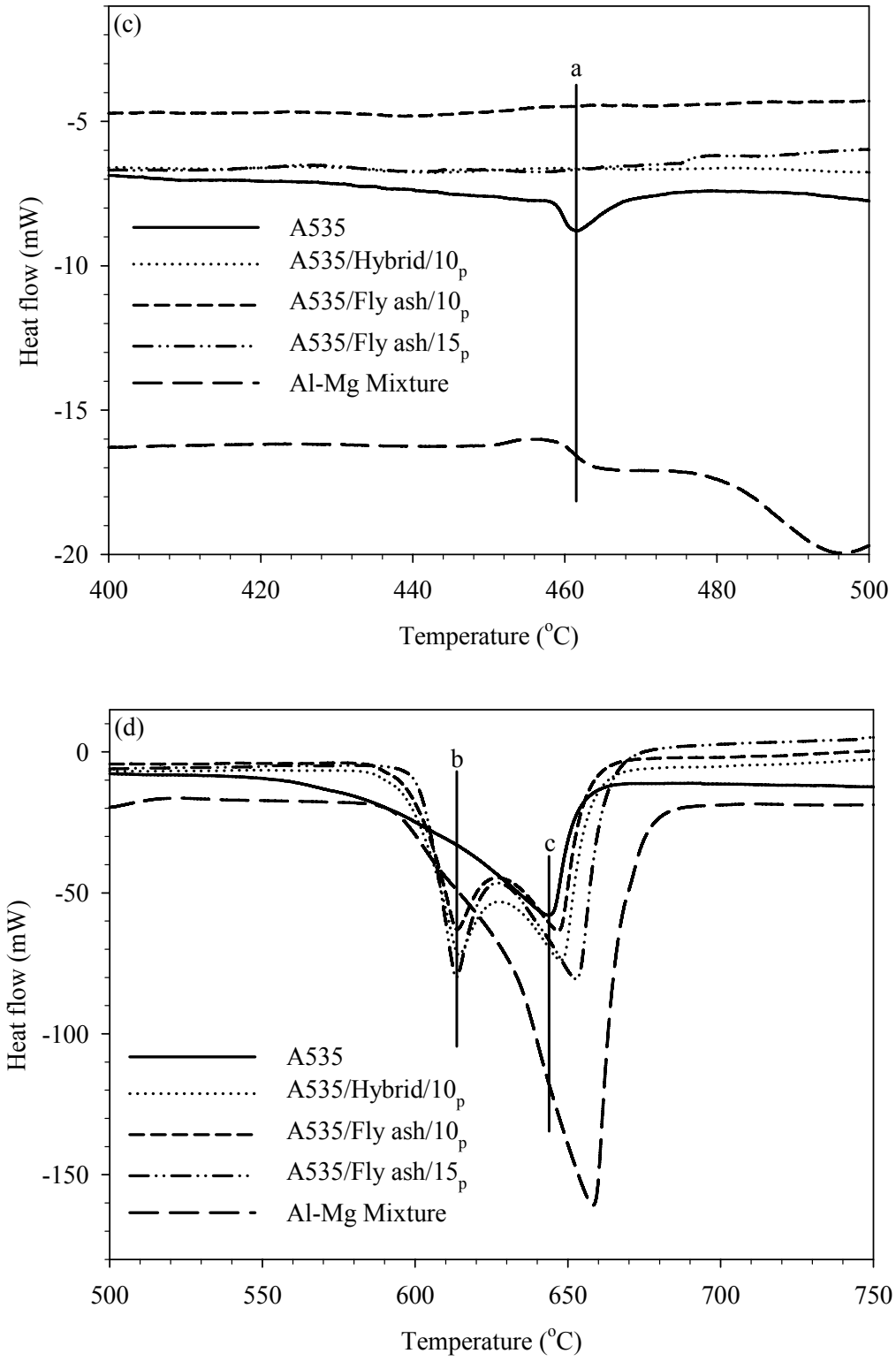

Figure 4.20 continues.

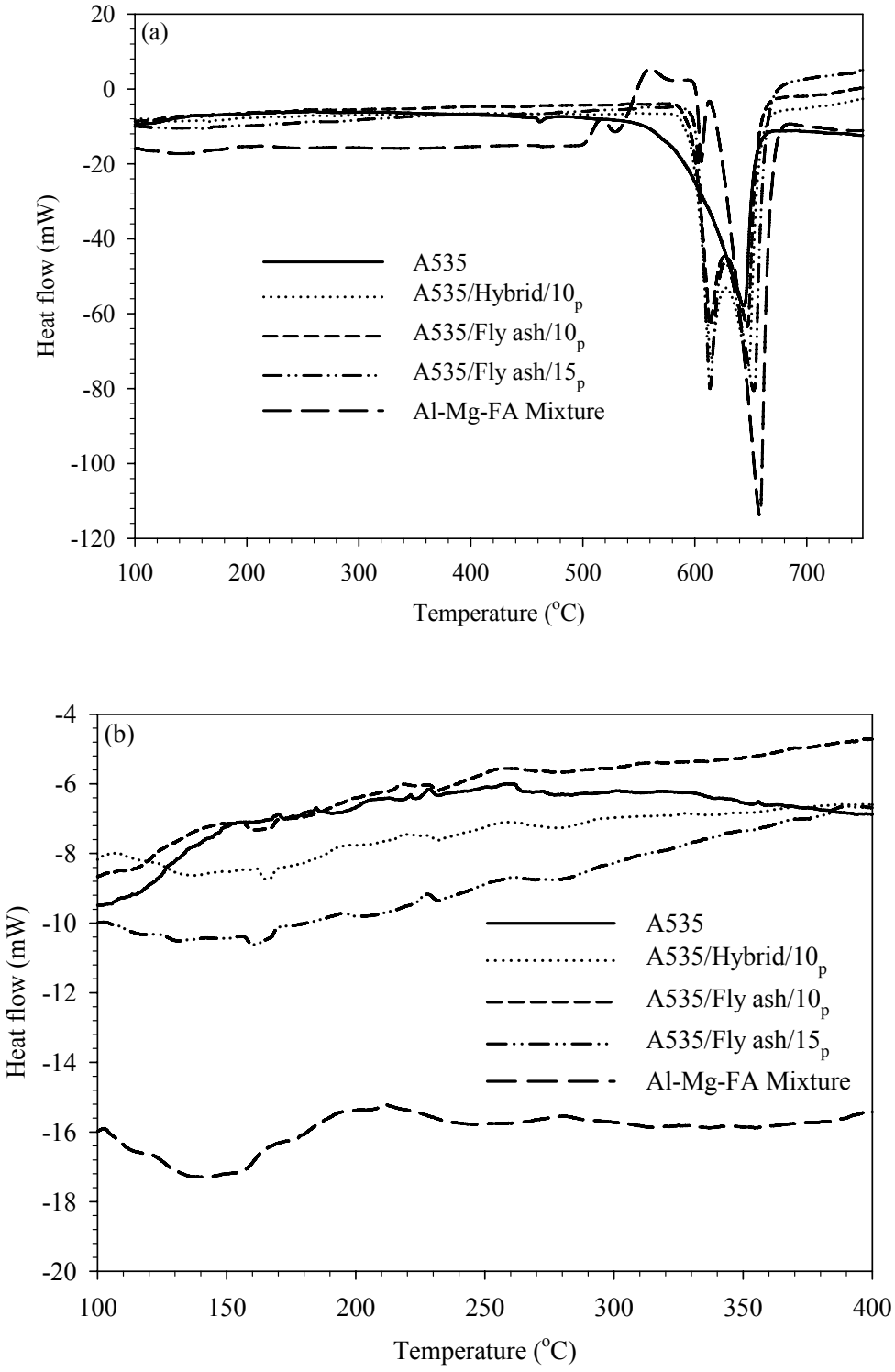

Figure 4.21. Typical DSC thermograms of A535 and its composites compared with that of Al-Mg-fly ash mixture on heating from 100 to 750 °C: (a) The complete thermogram, and its expanded views between (b) 100 and 400 °C, (c) 400 and 500 °C and (d) 500 and 750 °C.

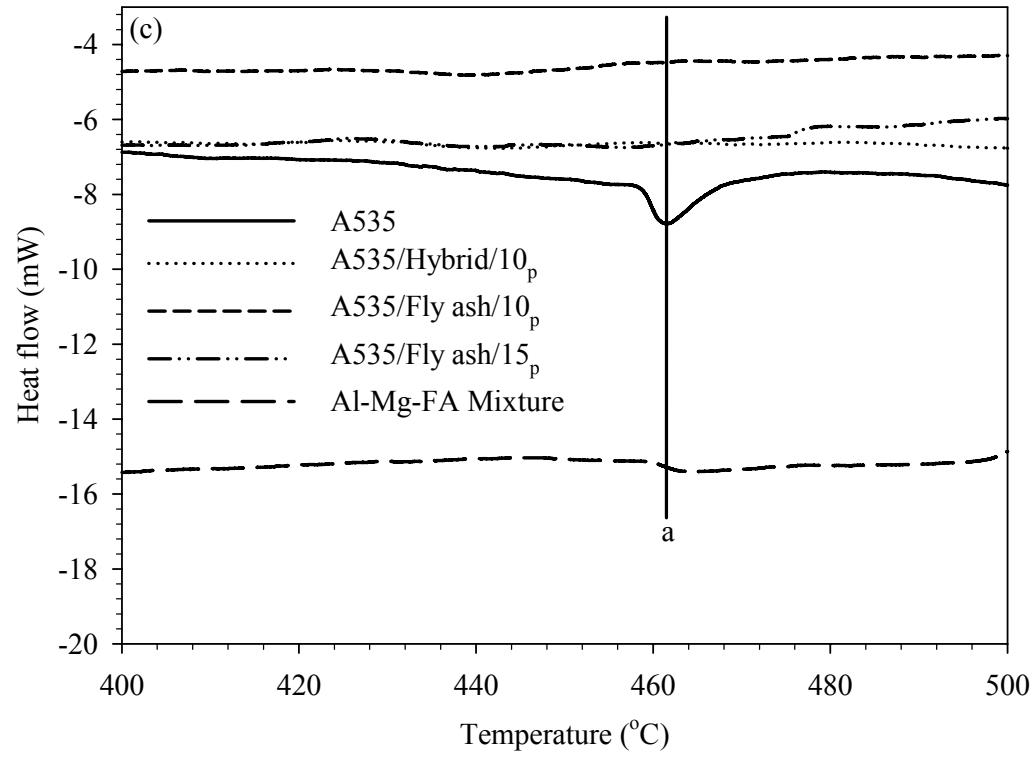

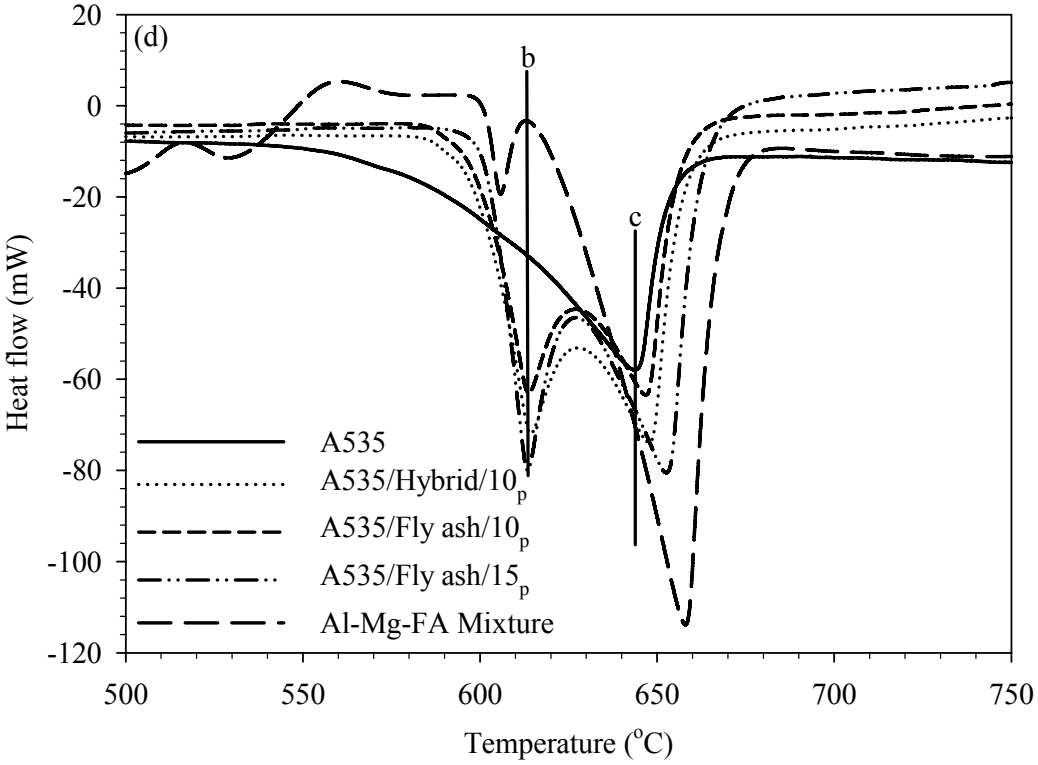

Figure 4.21 continues.

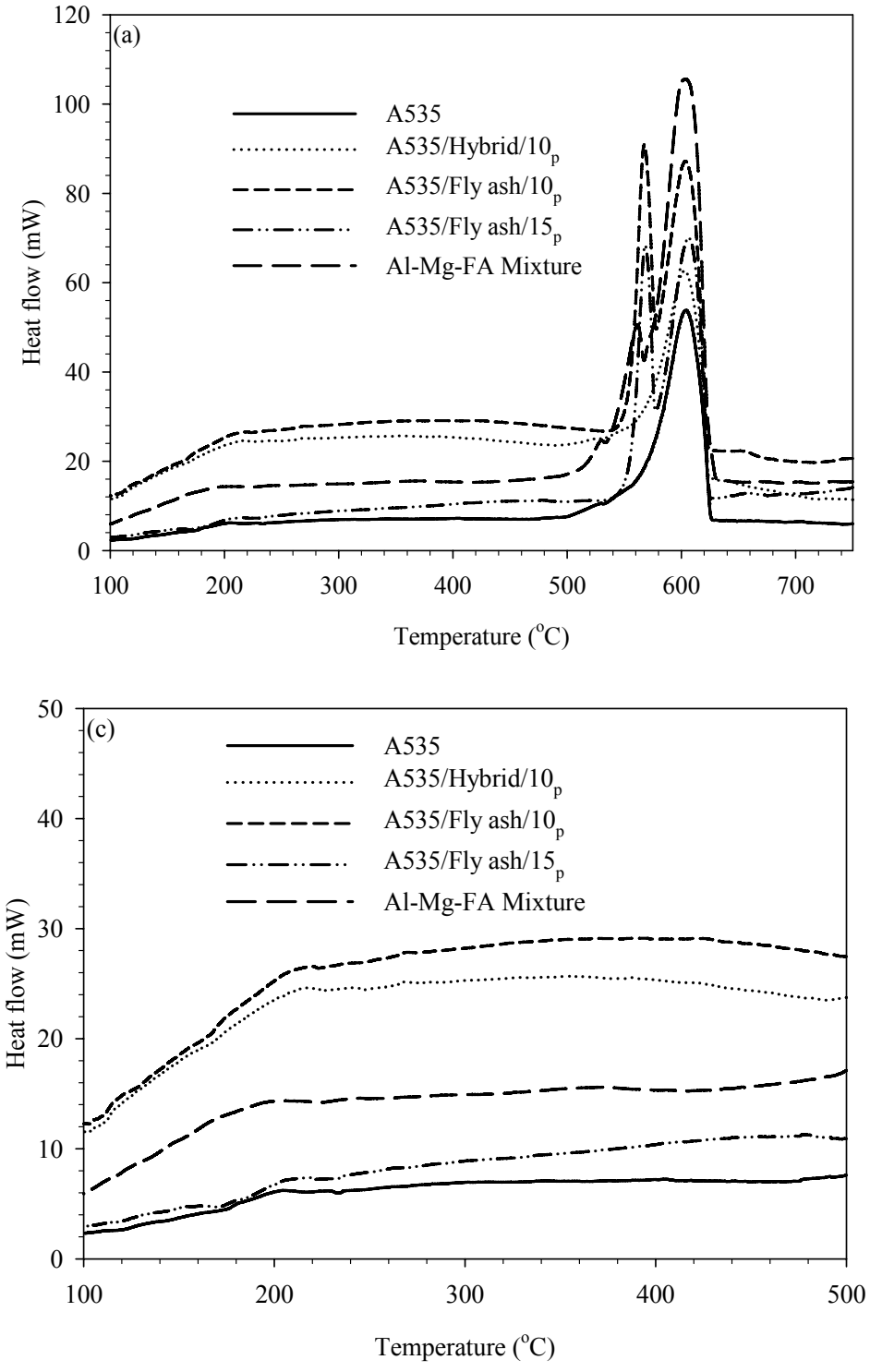

Figure 4.22. Typical DSC thermograms of A535 and its composites compared to that of Al-Mg-fly ash mixture on cooling from 750 to 100 °C: (a) The complete thermograms, and its expanded views between (b) 100 and 400 °C, (c) 400 and 500 °C and (d) 500 and 750 °C.

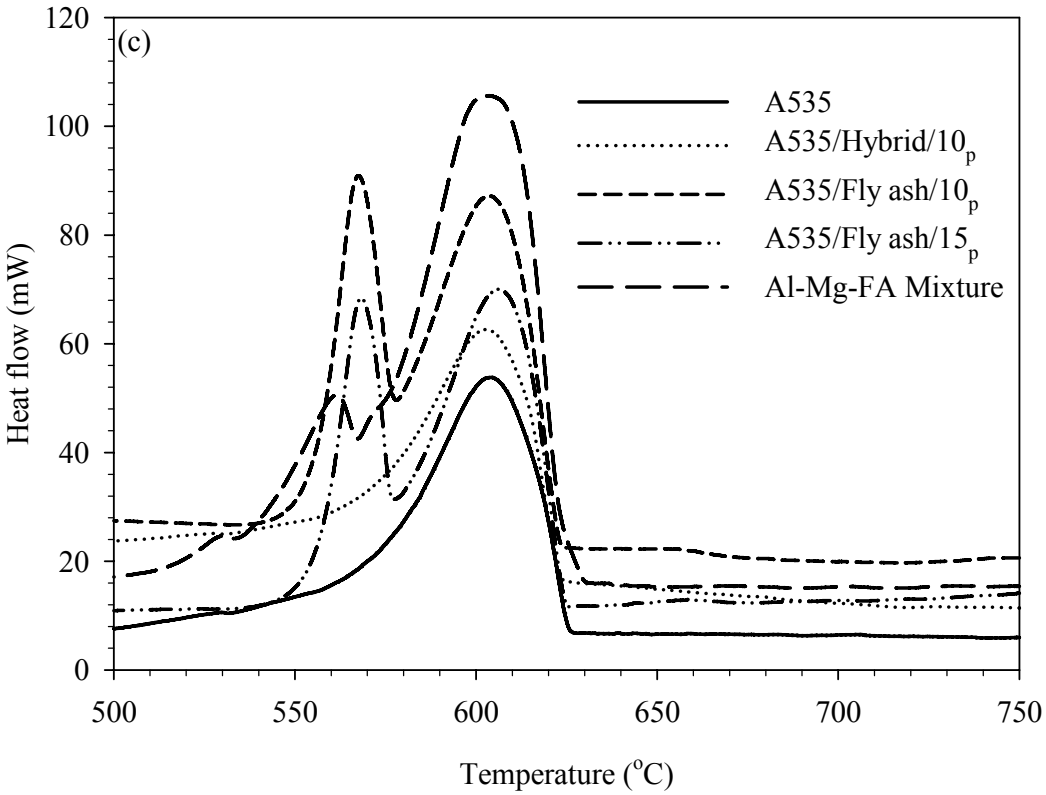

Figure 4.22 continues.

reversed during cooling. It can be seen that the positions of the exothermic peaks in Al-Mg-fly ash mixture occurred at about the same temperature as those of the test materials. This confirms that the endothermic peaks observed in the samples at about 614 ^{o}C were due to a reversible dissolution reaction in the MMCs.

4.3 X-ray Absorption Spectroscopy Study of Aluminium Alloys and Their MMCs

This section presents the results obtained from X-ray Absorption Spectroscopy (XAS) study of reactivity and charge transfer in aluminium alloy MMCs.

4.3.1 X-ray Absorption Spectroscopy Study of AA2618 and Its MMCs

The Al K- and L-edges spectra obtained from the XAS measurements of AA2618 and its MMCs are shown in Figures 4.23 and 4.24. The spectra were normalized with the nickel mesh current (I_o) to eliminate the contribution of edges arising from the interaction between the X-rays and the synchrotron machine components. The Al K- and L-edges of the samples were further analyzed after pre-edge background subtraction and post-edge normalization. The analyses of these normalized edges are discussed in the following paragraphs.

The normalized TEY and FLY Al K-edge ($1s \rightarrow 3p$ transitions) spectra for high-purity Al, AA2618 and its MMCs are shown respectively in Figures 4.25(a) and (b) and (c) and (d). The positions of the energy corresponding to the peaks in the spectra as well as the area under the peaks are shown in Table 4.6. It can be seen that the peaks labeled *a*, *b* and *c* in Figure 4.25(a) are common to both high-purity aluminium and AA2618. This is an indication that the reaction products which formed on the surfaces of the two materials are similar. However, the *p*-orbital population, which was determined from the area under the intensity peak of peaks *a*, *b* and *c*, increased by up to 56, 28, 12%, respectively, with the addition of 15 vol.% alumina particles into AA2618 (see Figure 4.25(b)). The implication of this is that the electrical conductivity of the material may be reduced due to the presence of Al_2O_3 particles. Kang *et al.* [106] observed a decrease in the electrical conductivity of copper with the addition of alumina particles. Zebarjad and Sajjadi [107] also reported that the magnitude of specific electrical resistivity of milled Al/Al_2O_3 composite was much higher than that of parent aluminum alloy.

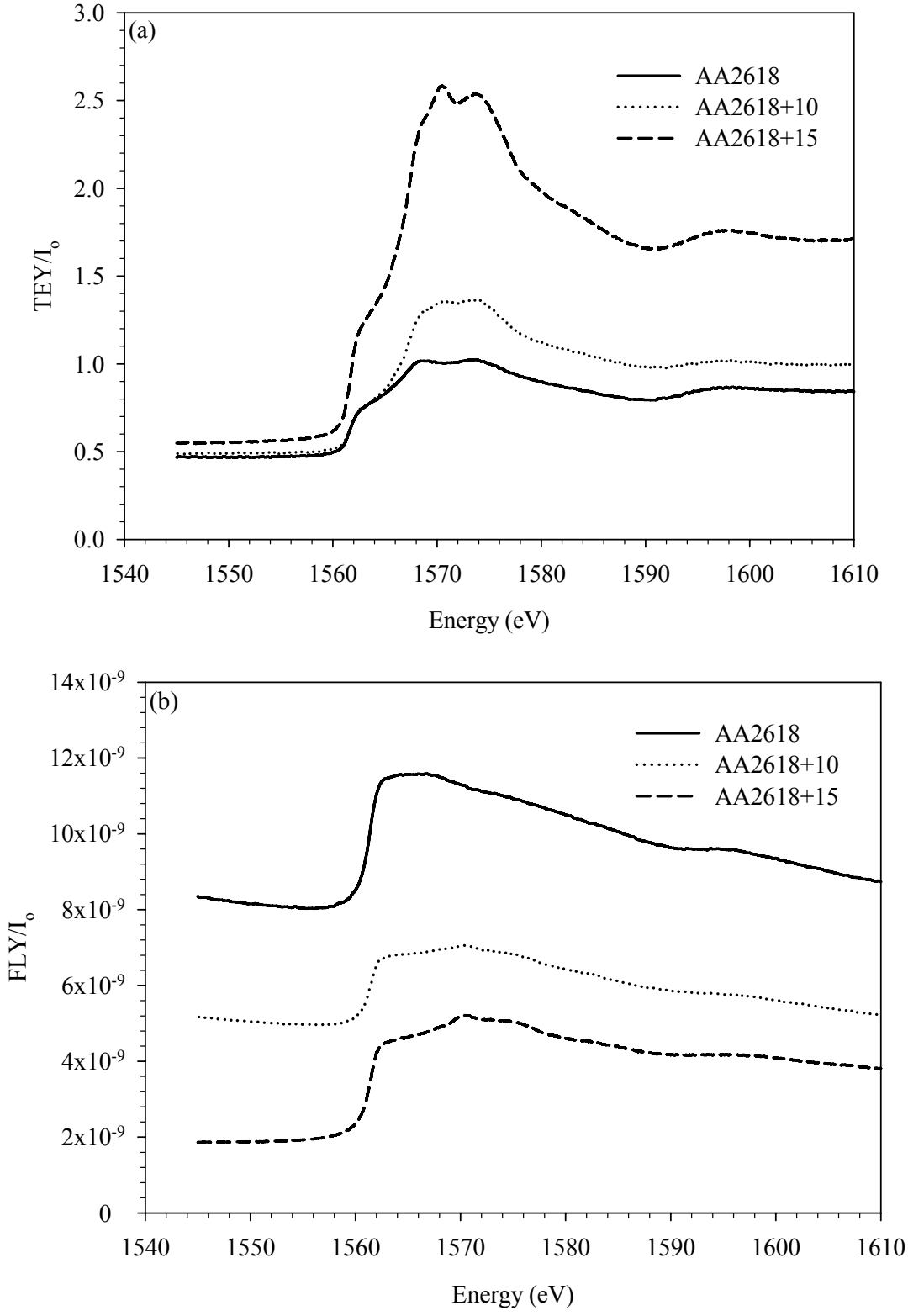

Figure 4.23. Typical Al K-edge spectra of AA2618 and its composites before pre-edge background subtraction and post-edge normalization. (a) TEY and (b) FLY.

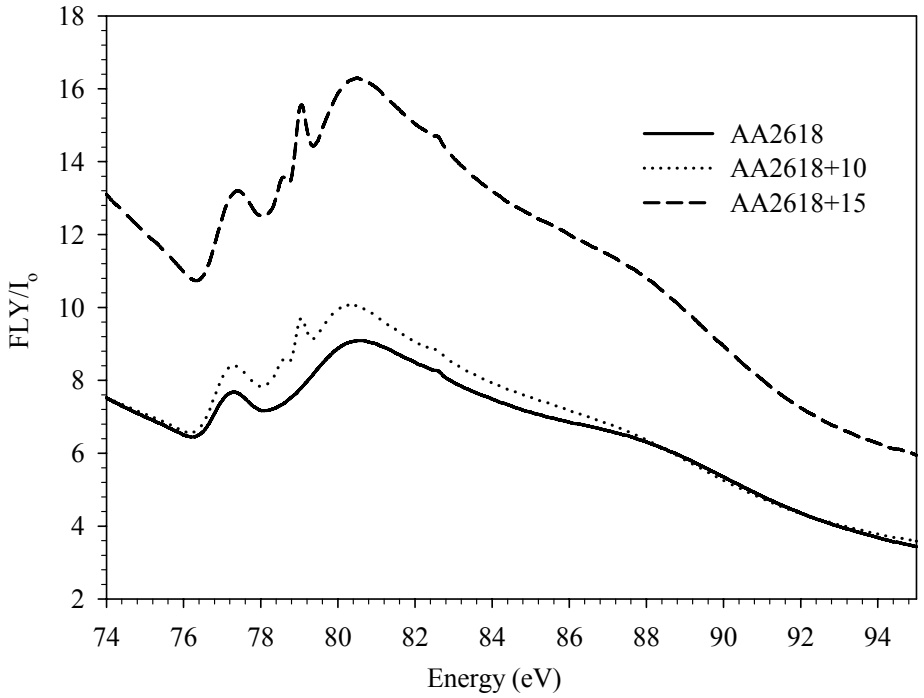

Figure 4.24. Typical Al L-edge FLY spectra of AA2618 and its composites before pre-edge background subtraction and post-edge normalization.

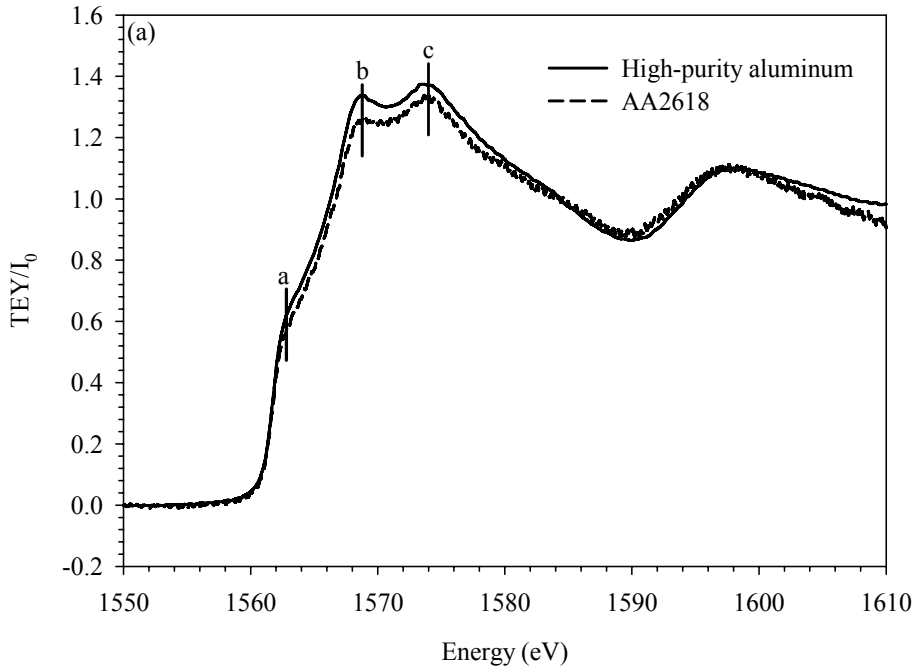

Figure 4.25. Normalized TEY and FLY Al K-edge spectra for high-purity Al, AA2618 and its MMCs: (a) TEY of high-purity Al and AA2618, (b) TEY of AA2618 and its MMCs, (c) FLY of high-purity Al and AA2618 and (d) FLY of AA2618 and its MMCs.

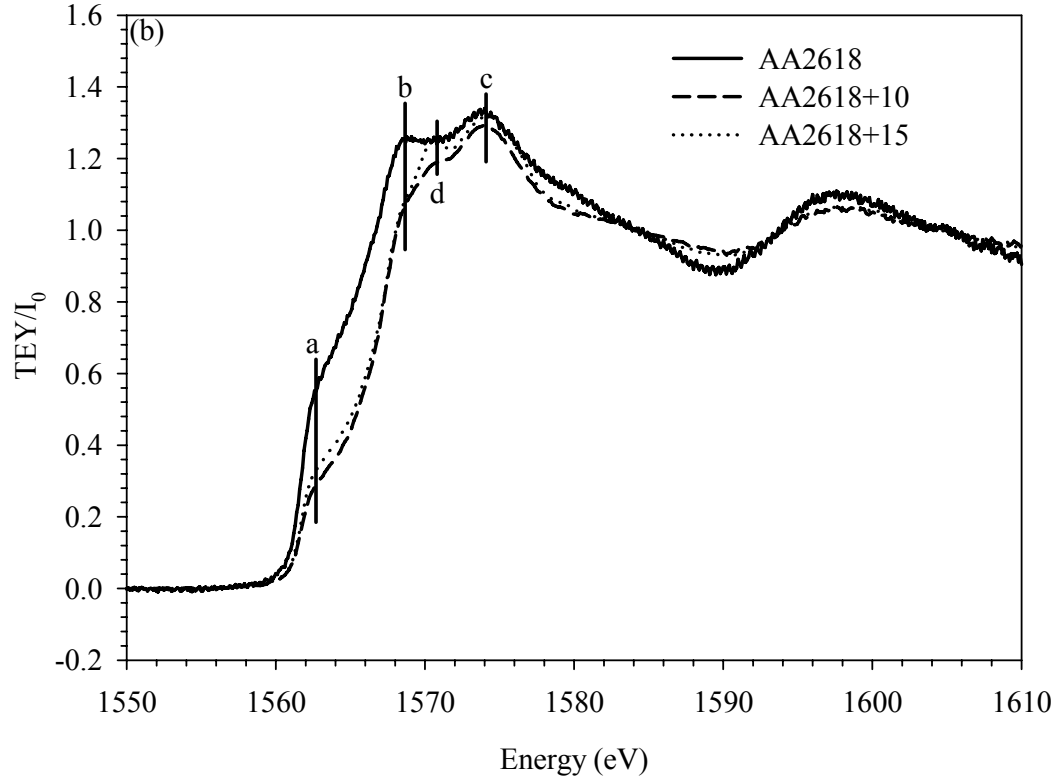

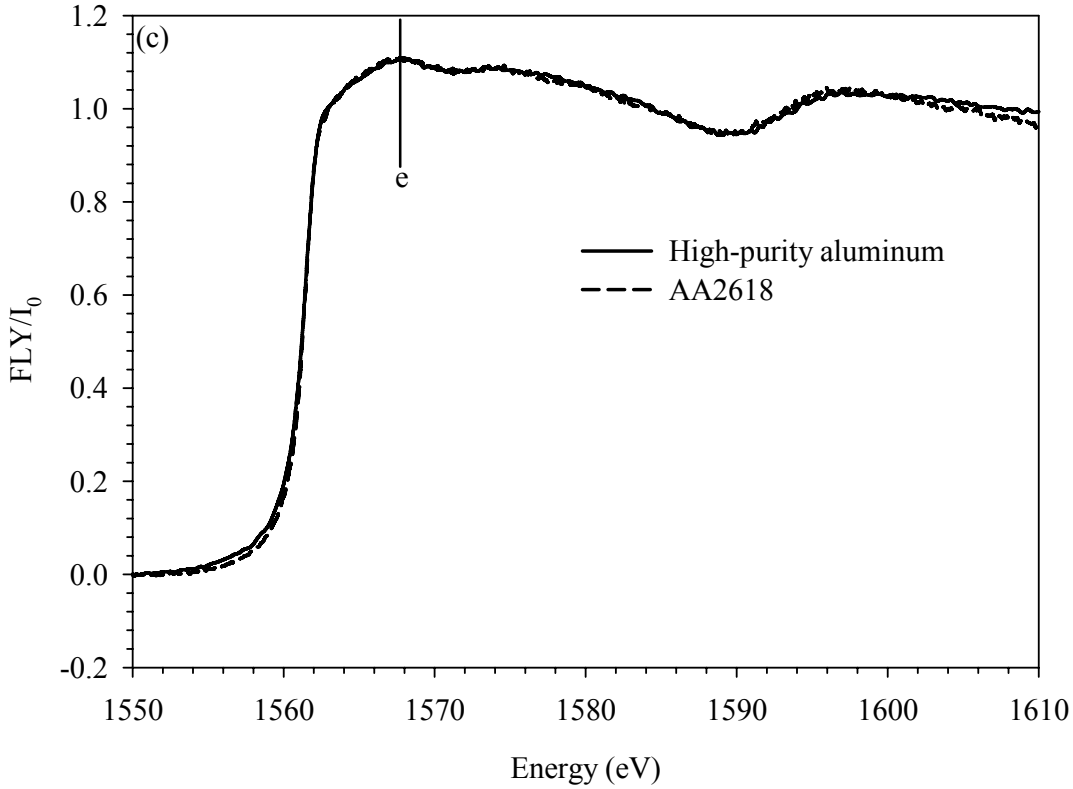

Figure 4.25 continues.

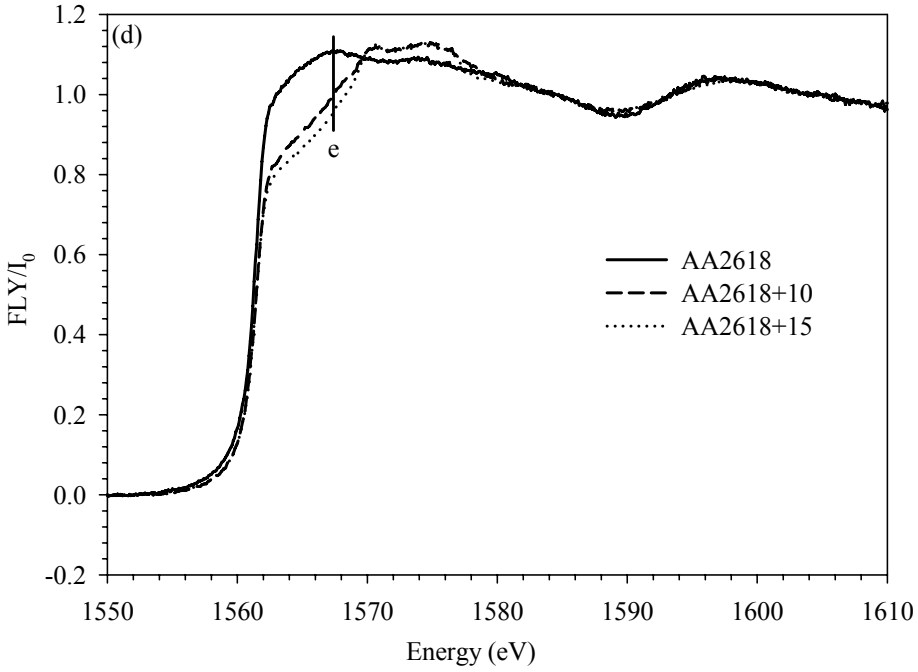

Figure 4.25 continues.

Table 4.6. Area under the peak in Al K-edge TEY spectra of AA2618 and its MMCs.

Materials	Peak *a* (~1563 eV)	Peak *b* (~1569 eV)	Peak *c* (~1574 eV)	Peak *d* (~1571 eV)
AA2618	1.8	9.4	20.4	---
AA2618+10	0.8	6.8	17.2	8.7
AA2618+15	0.9	6.8	18.1	9.8

Peak *d* in Figure 4.25(b) is common only to the composites, therefore suggesting that it is a contribution from alumina particles. Figure 4.25(c) shows that the bulk chemistry of AA2618 is practically the same as that of high-purity aluminium as the spectra of high-purity Al and AA2618 are practically indistinguishable. However, as can be seen in Figure 4.25(d), there is a shift in peak *e* for the composites which goes to show that there is a marked filling of the *p*-orbital population of aluminium in AA2618 with the addition of alumina. It can also be seen from Figure 4.25(d) that beyond 1580 eV the XAS spectra of AA2618 and the MMCs are virtually the same, thereby indicating that the coordination chemistry of aluminium in AA2618 did not change with the addition of alumina. However, when Figures 25(b) and (d) are compared, it becomes clear that this relatively stable coordination chemistry observed in the bulk (FLY) of the alloy changed

appreciably on its surface (TEY) with the addition of alumina particles.

The effect of alumina particles on the d-orbital population of aluminium in AA2618 is shown in Figure 4.26. The Al L-edge XAS spectra of high-purity Al, spinel and alumina are shown in Figure 4.26(a). The positions of the energies corresponding to the peaks in the normalized L-edge spectra as well as the area under the peaks are summarized in Table 4.7. Figure 4.26(c) shows that the area under the peak *f* is about the same with those of the composites, suggesting that the *d*-orbital population of Al in AA2618 and the composites is about the same. This indicates that the addition of alumina into AA2618 did not perturb the *d*-orbital population. In Figure 4.26(d), the positions of peaks *g* and *h* in the alumina spectrum match those in the composites. This shows that XAS can verify the presence of alumina in the composites. The Al L-edge in the spinel phase shows peaks *i*, *j* and *k* in Figures 4.26(a) and (e). It can be seen from Figure 4.26(e) that the peak labeled *i* does not exist in the XAS spectra of the composites examined as rectangular coupons. In order to further verify the presence of spinel in the composites, the extracted alumina was also examined and the results are presented in Figure 4.27.

Figure 4.27 shows the Al *L*-edge XAS spectrum of extracted alumina compared with those of spinel and high-purity alumina. In Figure 4.27(a), the positions of peaks *g* and *h* in the XAS spectrum of alumina are practically the same as in the extracted alumina. The kink at ~77.4 eV in the XAS spectrum of extracted alumina, which was not resolved by any of the peaks in high-purity alumina, can be seen in Figure 4.27(b) to match with the position of the peak labeled *i* in spinel. This then suggests that it is due to the presence of spinel in the extracted alumina. Thus, XAS can be used to identify the presence of the spinel phase in extracted alumina.

Figure 4.28 shows the XRD diffraction patterns obtained for extracted alumina, while Table 4.8 summarizes the relative amounts of the phases present in it. This is a good indication that spinel formed in the composites during fabrication, which is in agreement with the reactions shown in equations (2.12)-(2.14) and the results reported in [33].

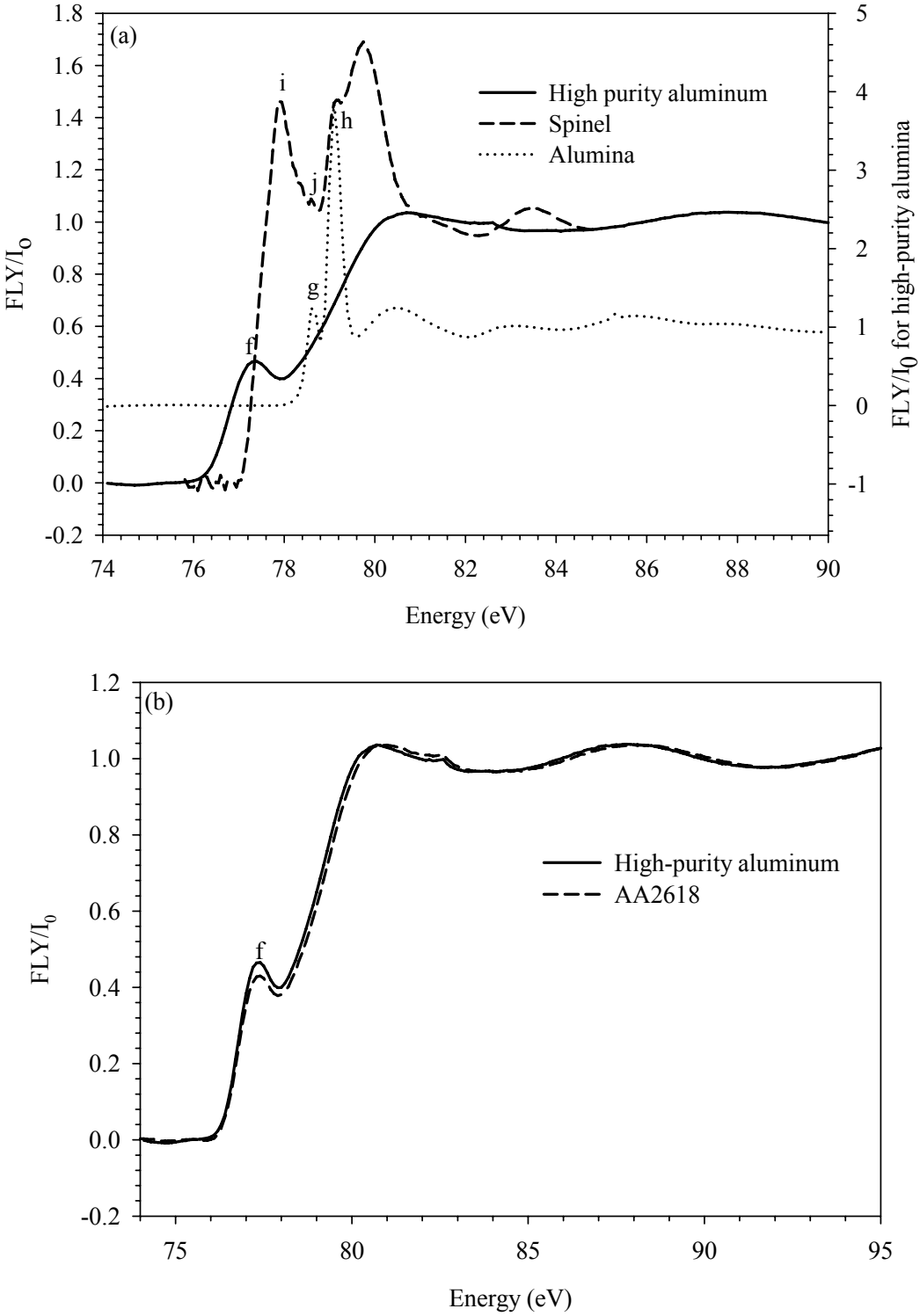

Figure 4.26. Normalized Al L-edge XAS spectra for high-purity Al, spinel, high-purity alumina, AA2618 and its MMCs: (a) High-purity aluminium, spinel and alumina, (b) high-purity aluminium and AA2618, (c) AA2618 and its MMCs and (d) AA2618 MMCs and high-purity alumina.

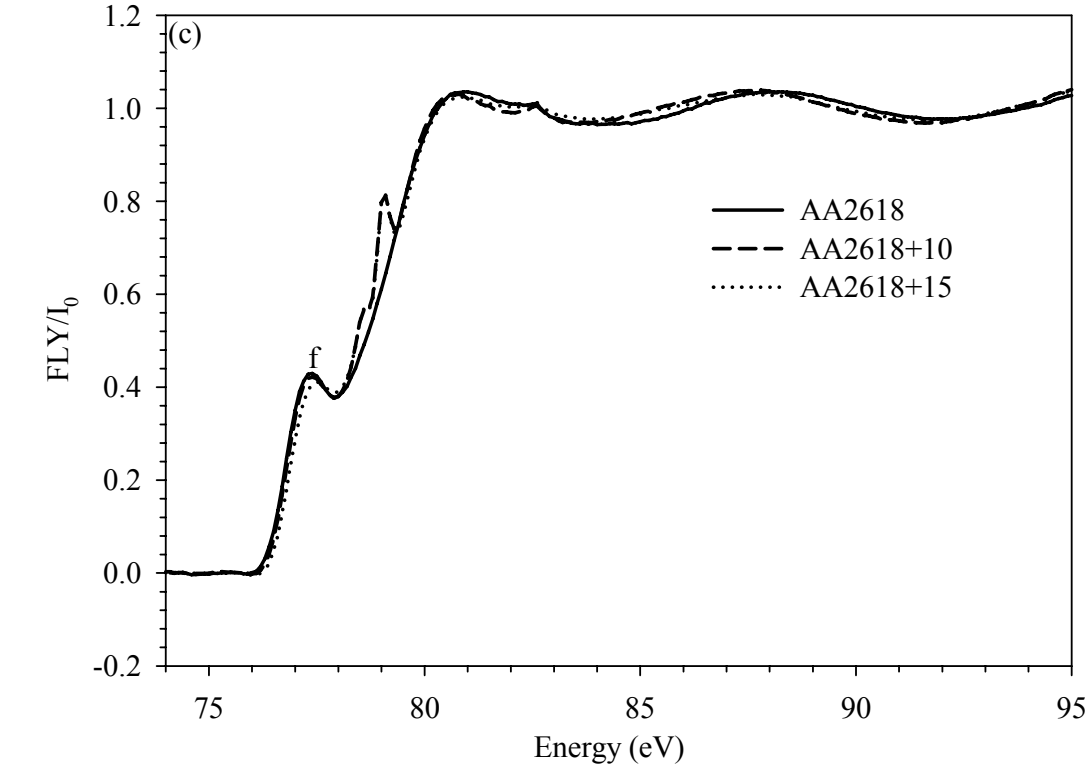

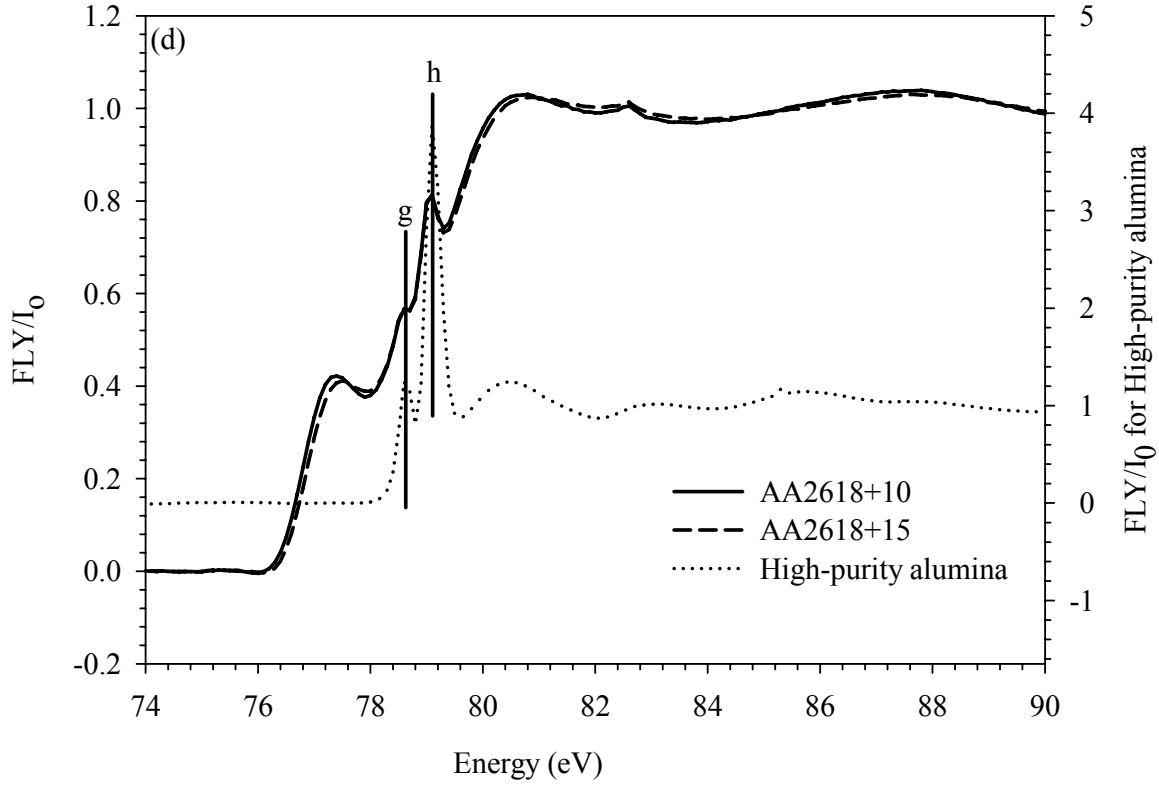

Figure 4.26 continues.

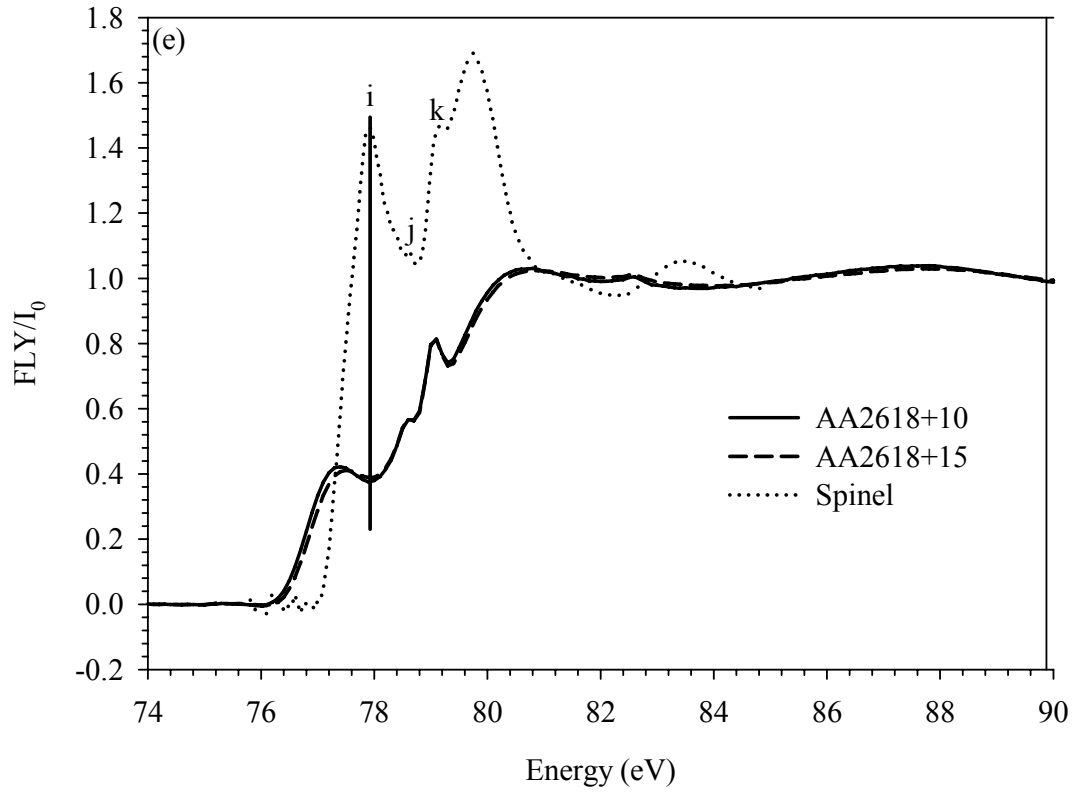

Figure 4.26 continues.

Table 4.7. Area under the peak in Al L-edge spectra of AA2618 and its MMCs.

Materials	Peak *f* (~77.4 eV)
AA2618	0.58
AA2618+10	0.57
AA2618+15	0.56

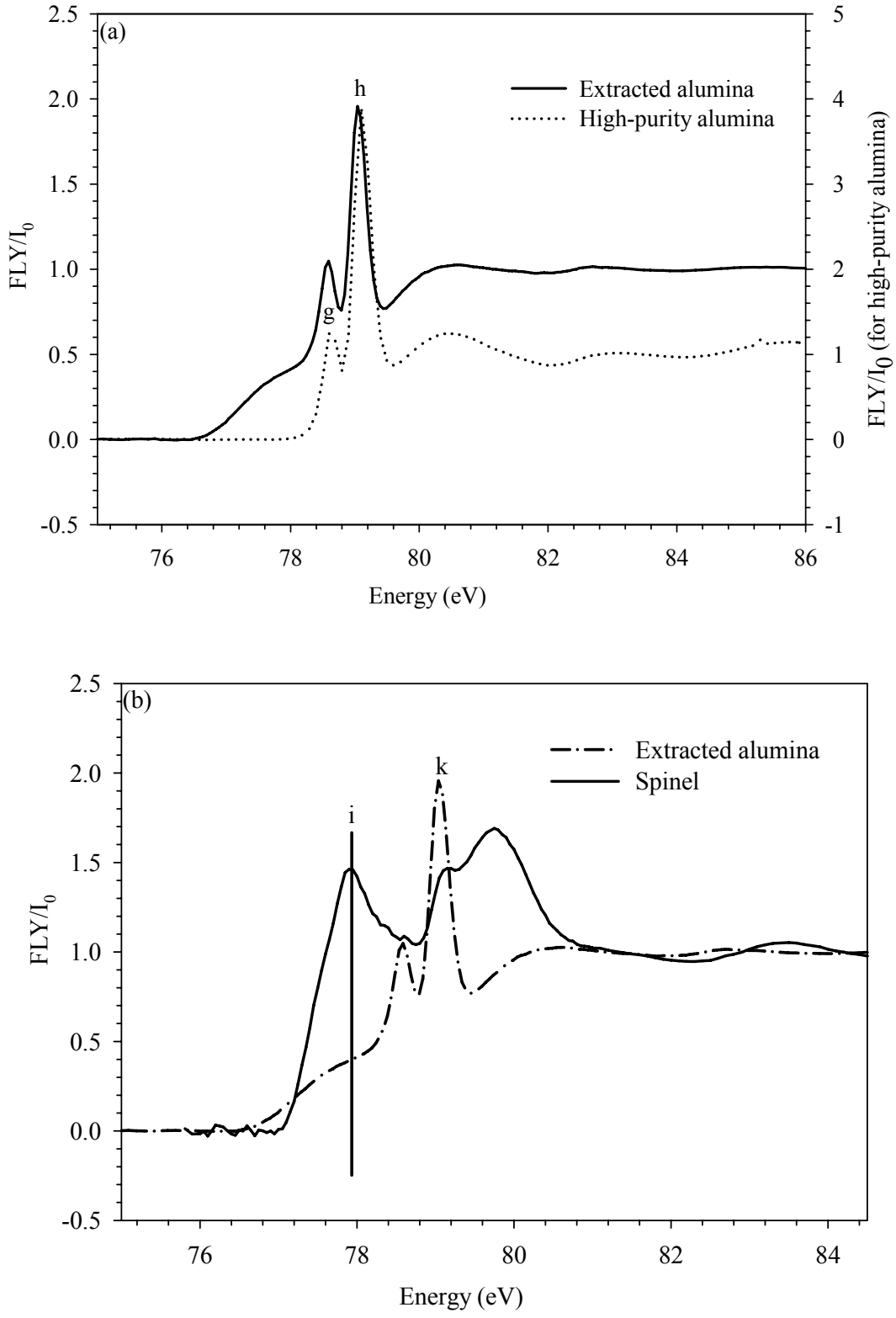

Figure 4.27. Normalized FLY Al L-edge spectra from (a) extracted alumina and high-purity alumina and (b) spinel and extracted alumina.

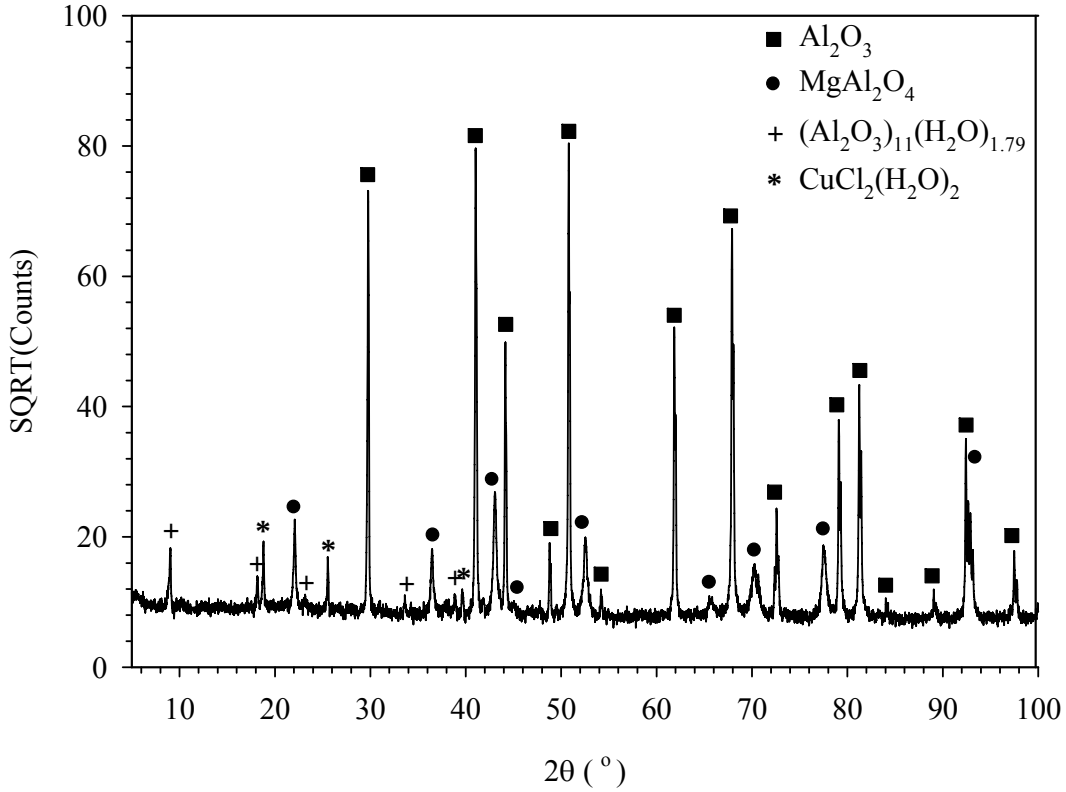

Figure 4.28. XRD diffraction patterns of extracted alumina.

Table 4.8. XRD analysis of extracted alumina.

Compound	Wt. %
Corundum. (Al_2O_3)	82.2
Spinel ($MgAl_2O_4$)	15.5
Beta-alumina hydrate $11Al_2O_3.1.79H_2O$	1.5
$CuCl_2.2H_2O$	0.9

4.3.2. X-ray Absorption Spectroscopy Study of Al-Mg Alloy A535 and Its MMCs Reinforced with Fly ash

Mg K-edge TEY and FLY spectra obtained from the extracted fly ash are shown in Figure 4.29, while those of industrial fly ash are shown in Figure 4.30. These spectra were not analyzed due to high signal to noise ratio, which made it difficult to carry out pre-edge background subtraction and normalization. The results obtained from XAS measurement of Al and Si K-edges of industrial and extracted fly ash are shown in Figures 4.31 to 4.32. These spectra were further analyzed after pre-edge background subtraction and post-edge normalization.

Figure 4.33(a) compares the normalized Al K-edge TEY of industrial fly ash and alumina, while Figure 4.33(b) compares those of industrial fly ash, alumina and spinel. The peaks observed in the figures are transitions from 1*s* (occupied) to 3*p*-dominant unoccupied states in Al, which satisfy the dipole-selection rule [69]. It can be seen that the peaks labeled *a* and *b* in Figure 4.33(a), and *c* and *d* in Figure 4.33(b), occurred at roughly the same binding energies as those of alumina. Thus, XAS can be used to identify the presence of alumina in industrial fly ash. The post-edge of the XAS spectrum of the industrial fly ash (i.e., beyond 1578 eV) slightly differs from that of alumina and this can be attributed to the difference in the chemical environment of alumina in fly ash and that in pure alumina. This is in good agreement with the interpretation for XAS spectra of Al and Si K-edges of glasses, aluminosilicate and ferric silicate gels in [108] and for Al K-edge near extended X-ray fine structure (NEXAFS) spectra of zeolite in [97].

Figures 4.34(a) and (b) show respectively the normalized FLY and TEY of Si K-edge of industrial fly ash, silicon oxide, and graphite tape. It can be seen from both figures that the position of the peak at 1847 eV in fly ash is resolved by that in SiO_2. This is an indication that XAS technique is capable of identifying the presence of SiO_2 in industrial fly ash.

Figures 4.35(a) and (b) show respectively the normalized Al K-edge TEY and FLY

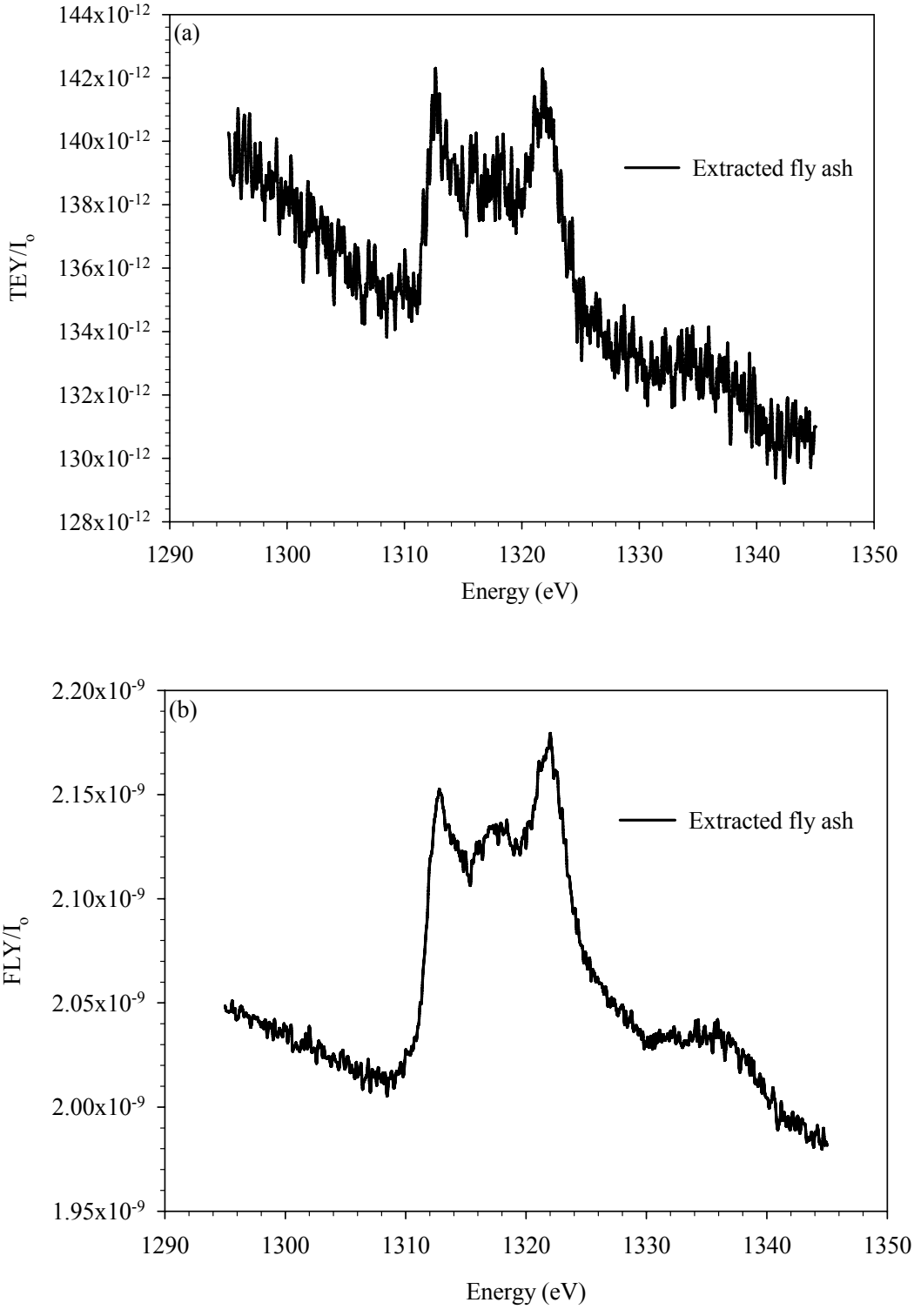

Figure 4.29. Typical Mg K-edge spectra of industrial fly ash before pre-edge background subtraction and post-edge normalization: (a) TEY and (b) FLY.

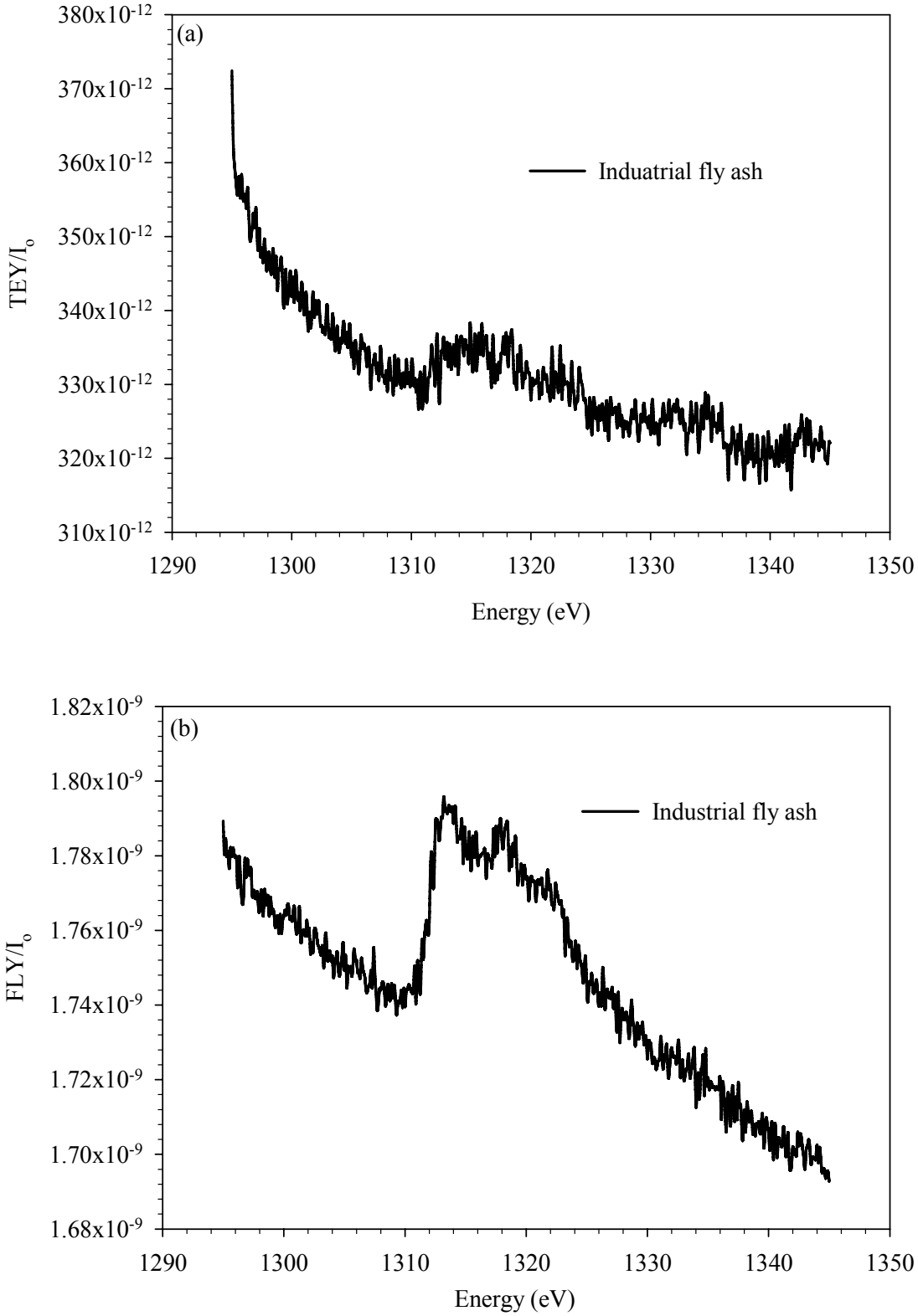

Figure 4.30. Typical Mg K-edge spectra of extracted fly ash before pre-edge background subtraction and post-edge normalization: (a) TEY and (b) FLY.

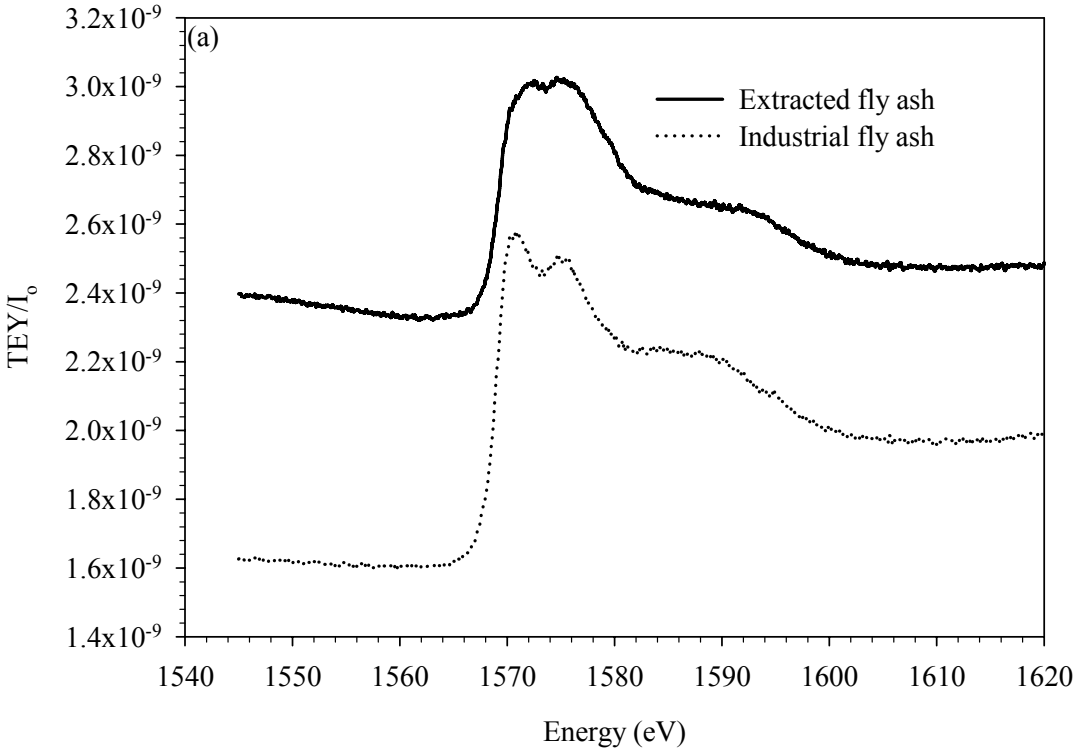

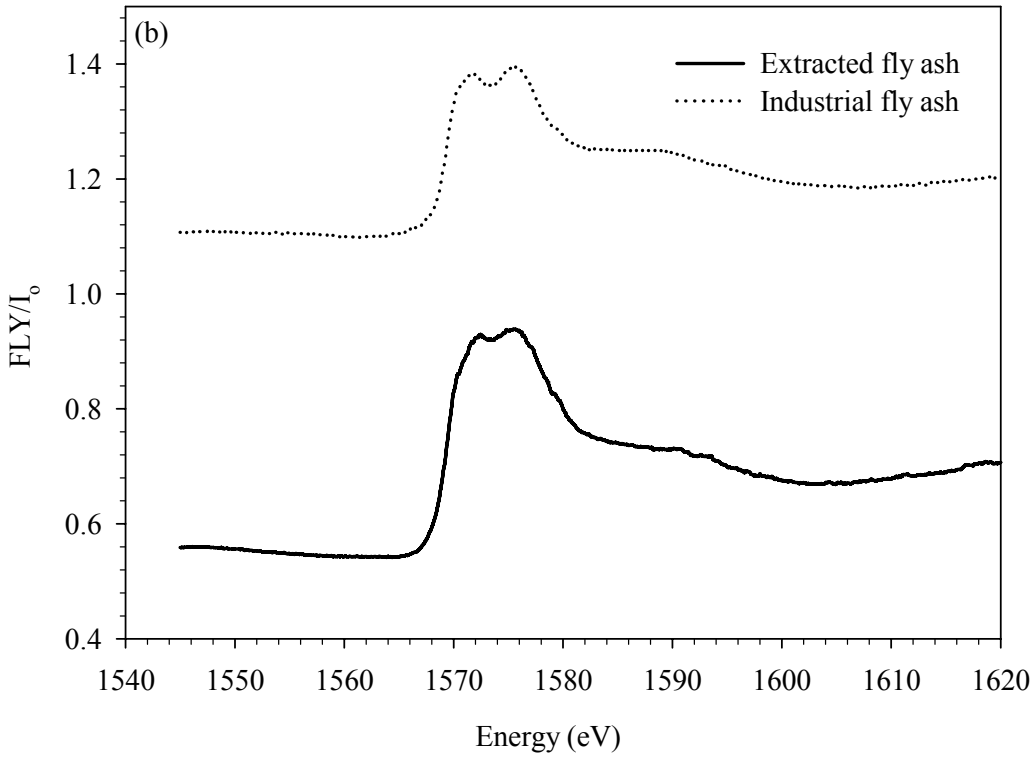

Figure 4.31. Typical Al K-edge spectra of extracted fly ash and fly ash before pre-edge background subtraction and post-edge normalization: (a) TEY and (b) FLY.

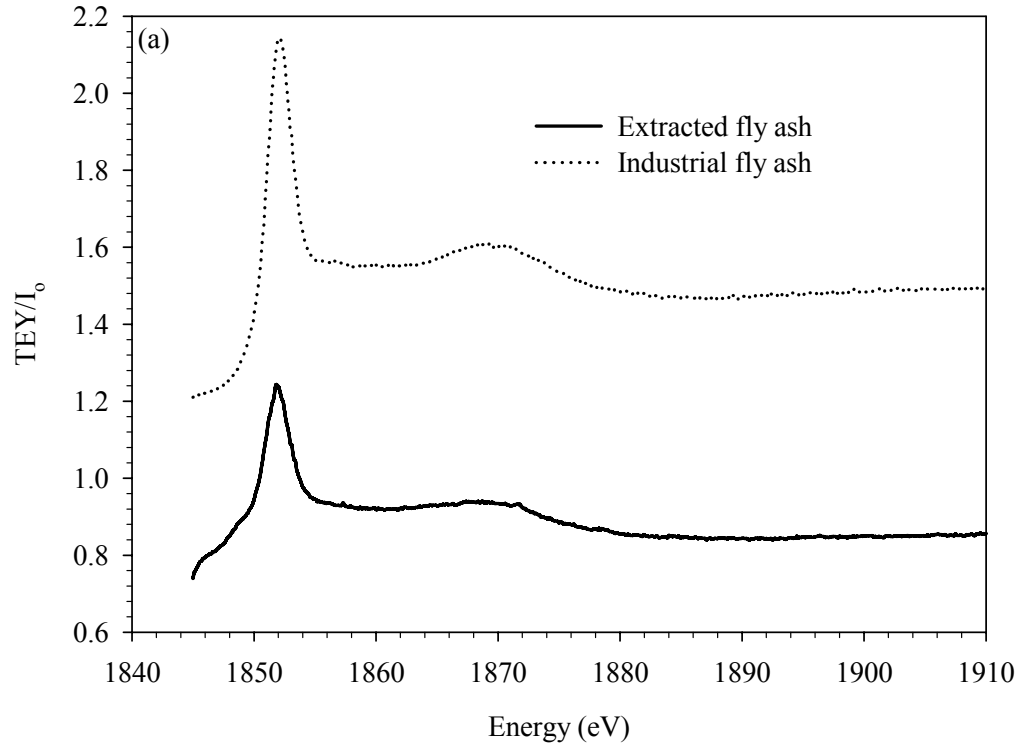

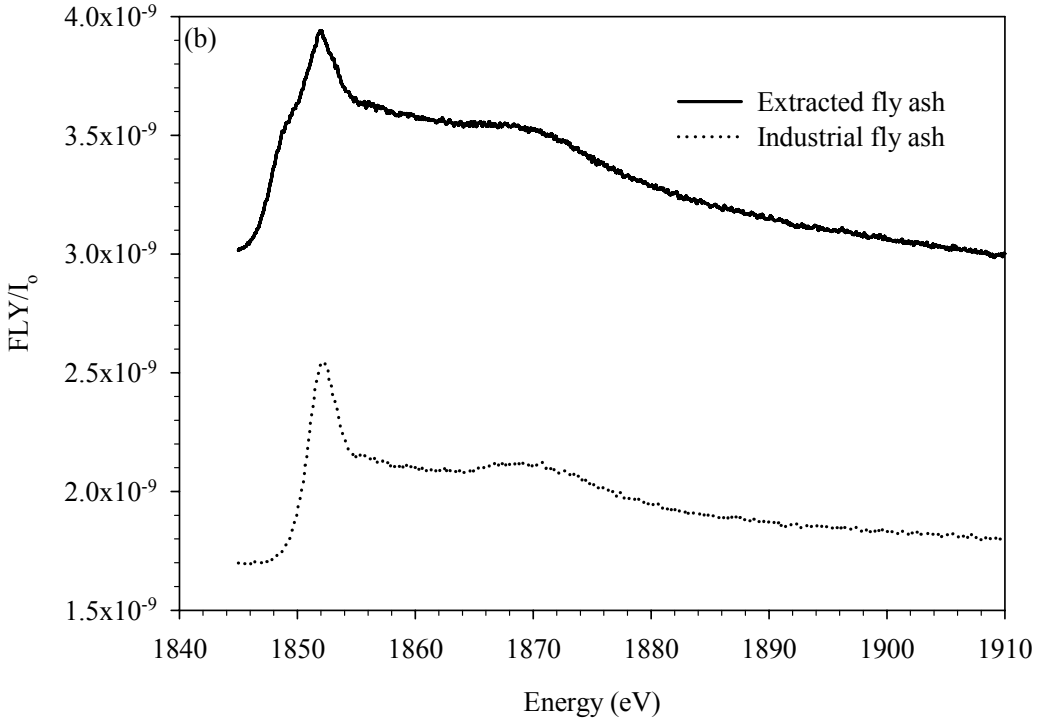

Figure 4.32. Typical Si K-edge spectra of extracted and industrial fly ash before pre-edge background subtraction and post-edge normalization: (a) TEY and (b) FLY.

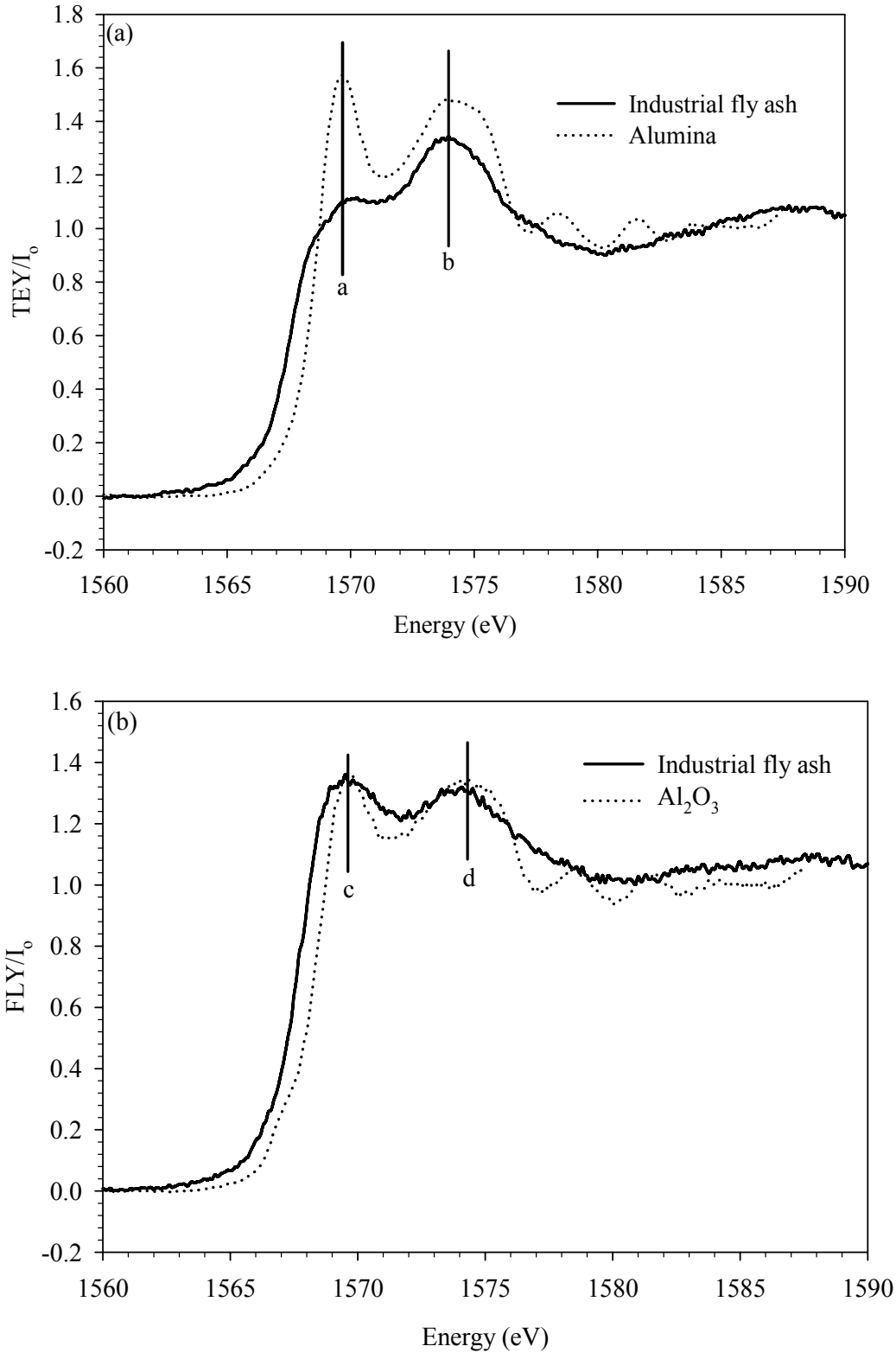

Figure 4.33. Normalized TEY and FLY Al K-edge spectra of industrial fly ash and Al_2O_3 and spinel: (a) TEY and (b) FLY.

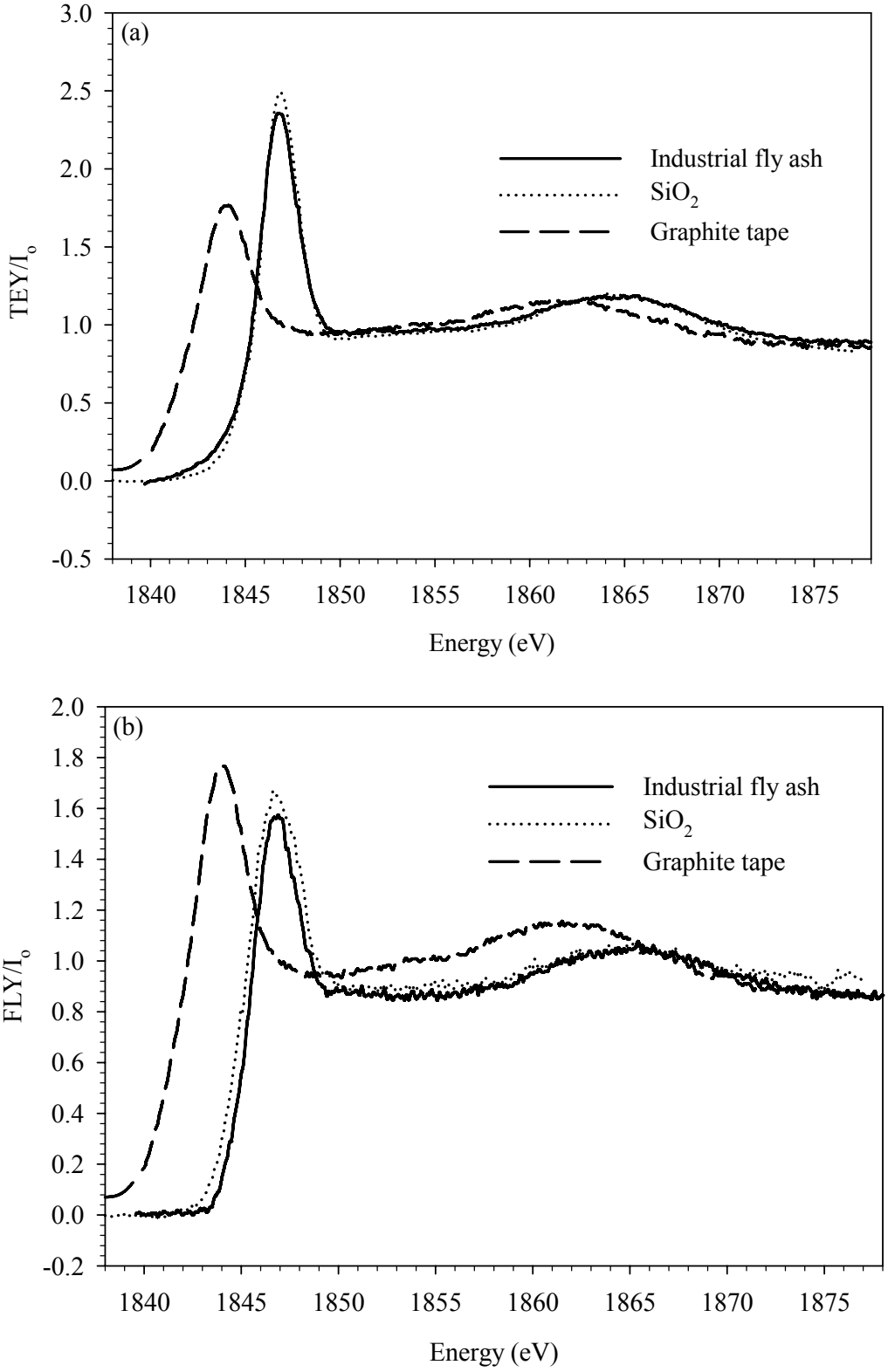

Figure 4.34. Normalized TEY and FLY Si K-edge spectra of industrial fly ash, SiO_2, and graphite tape: (a) TEY and (b) FLY.

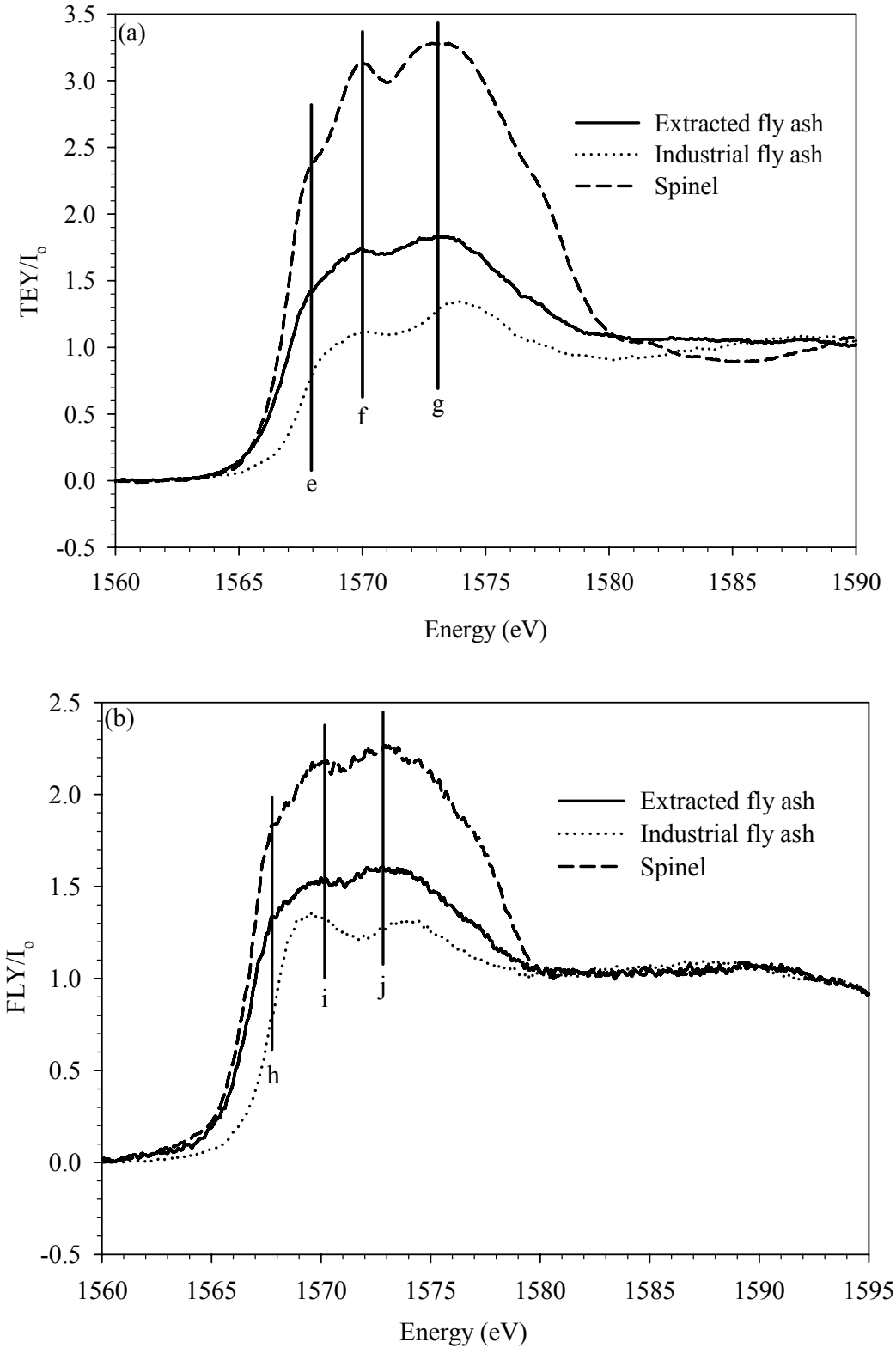

Figure 4.35. Normalized TEY and FLY of Al K-edge of extracted fly ash, industrial fly ash and spinel.

spectra of extracted fly ash, industrial fly ash and spinel. It can be seen that the positions of peaks labelled *e*, *f* and *g* in the XAS spectrum of spinel (Figure 4.35(a)) match those of the extracted fly ash. Similarly, peaks *h*, *i* and *j* in the normalized FLY shown in Figure 4.35(b) match those of spinel. This is a strong indication that spinel formed in the extracted fly ash, which is in agreement with the reaction schemes shown in equations (2.14) - (2.16) and the results reported in [16, 28, 33, 48].

Figure 4.36(a) and (b) show respectively the normalized FLY and TEY spectra of Si K-edge of extracted fly ash, industrial fly ash, silicon oxide, and graphite tape. The XAS spectrum of graphite tape was obtained to identify the its contributions in those of extracted fly ash, industrial fly ash, and silicon oxide. Table 4.9 summarizes the area under the peak of the Si K-edge for extracted fly ash and industrial fly ash. The decrease in the amount of SiO_2 in the extracted fly ash relative to industrial fly ash was determined by dividing the difference in the Gaussian peak areas of SiO_2 in the extracted and industrial fly ash with the total of all the Gaussian peak areas. It can be seen from Figure 4.36 that the position of the peak at 1852 eV in industrial and extracted fly ash matches that of SiO_2. However, Table 4.9 shows that the area under the Si K-edge peaks in the TEY and FLY spectra of extracted fly ash are about 12 and 31% smaller than those of industrial fly ash, respectively. This may be due to the reduction of SiO_2 by molten magnesium (see equations (2.18)) or aluminium during the fabrication of the composites. The excess free silicon played a role in the formation of silicon-containing phases such as magnesium siliside, mullite and aluminosilicate glass which has been verified using XRD in reference [39]. The increased amount of Mg_2Si in the MMCs was reported to deplete the solid solution magnesium atoms, which, in turn, degraded their mechanical properties [16]. The peak labeled *c* in Figure 4.36(b) could be a contribution from the graphite tape or Si-rich phases in the A535 MMC. This should be further investigated by acquiring XAS spectra of magnesium silicide, mullite, and aluminosilcates.

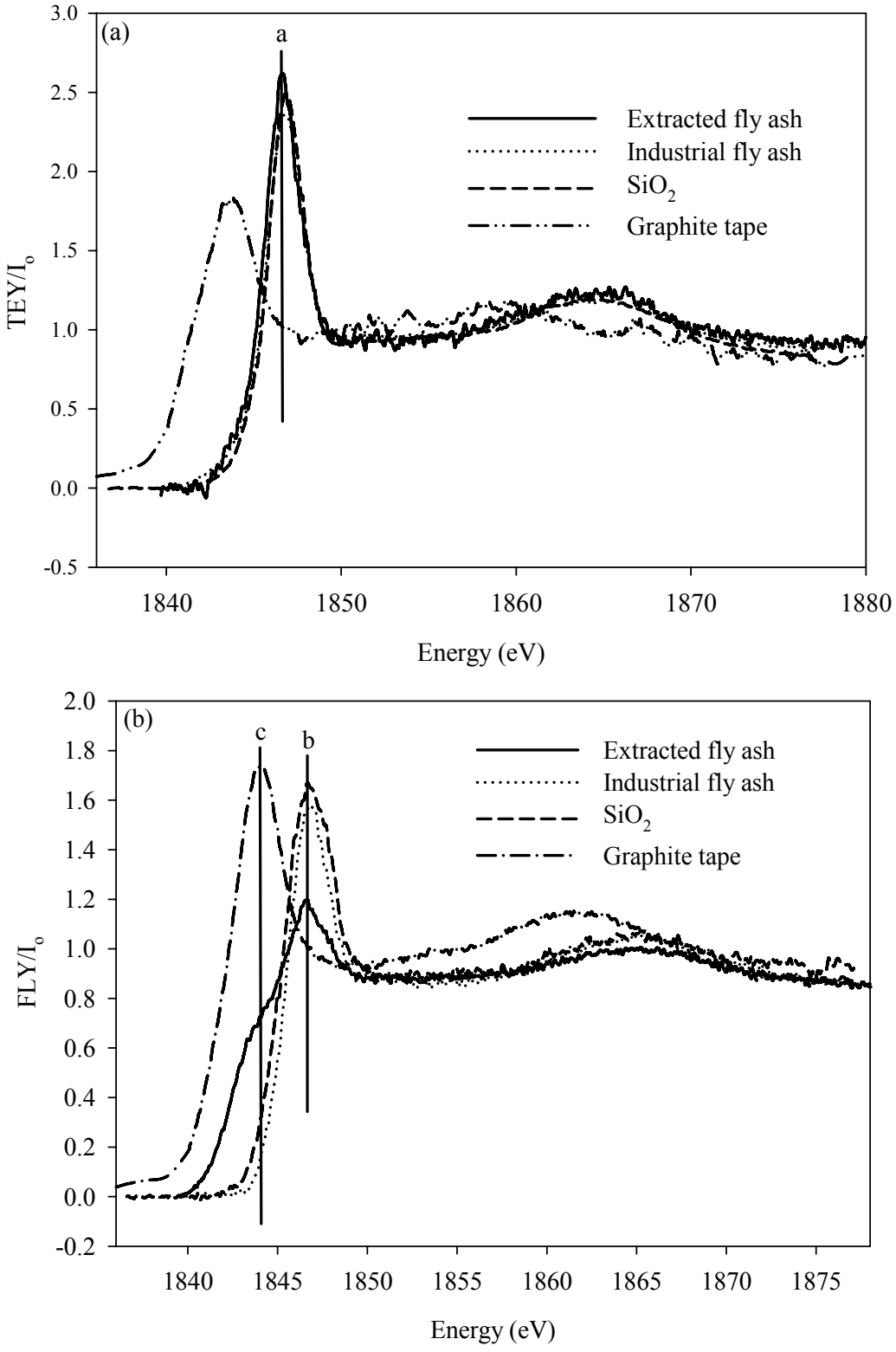

Figure 4.36. Normalized TEY and FLY of Al K-edge spectra of extracted fly ash, industrial fly ash, SiO_2, and graphite tape: (a) TEY and (b) FLY.

Table 4.9. Area under the peak labeled *b* in Al K-edge spectra of industrial and extracted fly ash.

Material	TEY (1852 eV)	FLY (1852 eV)
Extracted fly ash	4.6	5.2
Industrial fly ash	5.6	7.5

4.4. Summary

This study focused on two aluminium alloy composite systems which were prepared using the liquid-state fabrication method, namely, Al-Mg alloy A535 and Al-Cu-Mg alloy AA2618 composites. The alloys were reinforced with ceramic particles in order to improve their wear resistance, thermal expansion behaviour, and mechanical properties. AA2618 was reinforced with alumina, while A535 was reinforced with fly ash and silicon carbide. Fly ash was used as a reinforcement in A535 to reduce the disposal and environmental problems associated with it as well as reduce the weight and cost of the composite.

Two principal studies were carried out in this work. In the first, the effect of fly ash on the thermal expansion behavior of A535 was investigated. As mentioned in Section 2.2, the alloy has a good thermal stability. However, a previous study [16] showed that the addition of fly ash into it introduced porosities and reaction products which could affect the thermal expansion behavior. Therefore, the purpose of the present study was to understand the extent to which these defects affected the thermal expansion behavior of A535. The second study was to explore the use of XAS technique to study reactivity in aluminium alloy A535 and AA2618 composites. DSC was used to verify the occurrence of reactions and phase transformations in A535 and its MMCs. It was not done for AA2618 and its MMCs because phase transformations and reactions that occur in them have been studied in reference [33].

The thermal expansion results showed that the addition of fly ash in A535 decreased the CTE, which improved its thermal stability. Also, A535 and its composites underwent

phase transformations within the temperature range investigated. The undulations observed above 450 ^{o}C in the displacement and CTE plots were attributed to the melting/dissolution of Mg_2Al_3 formed in the test materials during fabrication, while those that occur below 450 ^{o}C are most likely due to vibrations in the equipment or from an external source during measurement. In order to identify phase transformations and reactions that occurred in A535 MMCs, OM, SEM, EDS, DSC and XAS were used. The OM, SEM, EDS studies of the alloy showed the presence of phases such as Mg_2Al_3, which is known to dissolve at 462^{o}C [105]. The DSC results presented in Section 4.2 showed an endothermic reaction peak within the temperature range where Mg_2Al_3 dissolves. The DSC was not able to pick up less energetic phase transformations in the materials below 450 ^{o}C. This is because DSC is sensitive only to thermal transitions in materials and, as such, may not capture any phase transformation that does not produce measurable thermal energies, but could lead to dimensional changes.

The DSC study of reactivity and phase transformations in A535 MMCs showed an endothermic reaction peak between 580 and 626.8 ^{o}C. This reaction peak at was attributed to the dissolution of the phase formed from the reaction between fly ash and the alloy. In order to identify this phase, an X-ray diffraction study of the phase transformation in this temperature range is recommended for further studies.

Previous XRD studies have identified the presence of reaction products such as spinel and magnesium disilicide in A535 MMCs reinforced with fly ash [16]. In order to improve the possibility of identifying reaction products using XAS, fly ash was extracted from the composite using Aqua Regia. The results obtained from the extracted fly ash shows the presence of spinel and silicon-rich phases in the composite. Based on this result, XAS can be used as a complimentary technique in identifying reaction products in aluminium MMCs.

Reactivity in AA2618 and its MMCs was studied using XAS and XRD, with a view to identify the reaction products that formed in them during fabrication. Both techniques were able to identify the presence of alumina and spinel, a reaction product, in the

composites. It was also observed that the interaction between the alloy and alumina affected the electronic structure of the alloy. The *p*-orbital population and the surface chemistry of aluminium on the surface of the alloy changed with the addition of alumina particles.

5.0 CONCLUSIONS AND RECOMMADATIONS

This chapter presents the conclusions drawn from this work as well as recommendations for future work.

5.1 Conclusions

1. The results of the thermal expansion study showed that the CTE of A535 decreases with the addition of fly ash and silicon carbide due to the low CTE of these ceramic materials.

2. The presence of spinel ($AlMg_2O_4$) in the extracted alumina shows that alumina reacted with AA2618 alloy during the fabrication of the MMCs. Similarly, spinel was formed in A535-fly ash composites due to the reaction between fly ash and A535 alloy during fabrication.

3. The melting temperature of A535 alloy increased with the addition of ceramic particles.

4. XAS is a viable complementary tool for studying reactivity in particulate aluminium MMCs as well as their electronic structures. The addition of alumina particles into AA2618 perturbed the occupation of *p*-orbitals in the aluminium in the alloy at the surface, and in the bulk of the aluminium in AA2618. Furthermore, the population of *d*-orbitals in the aluminium in AA2618 is about the same with those of the MMCs. The chemistry of aluminium on the surface of the alloy changed with the addition of alumina particles into AA2618, but remained about the same in the bulk.

5.2.1 Recommendations for Future Work

1. A mathematical model that predicts the effect of the addition of ceramic particles in A535 on its thermal expansion behaviour needs to be developed.

2. Fly ash contains oxides of iron which can react with A535, forming iron-rich reaction products. In order to identify and quantify these reaction products, XAS study of Fe K- and L- edges of A535 and its MMCs needs to conducted.

3. EXAFS study of aluminium K-edge of the test materials should be carried out to determine the effect of addition of ceramic particles into A535 and AA2618 on the aluminium coordination chemistry (bond lengths and coordination number) in the alloys. This will aid the understanding of the tensile thermal and electrical properties exhibited by these materials.

REFERENCES

1. I. J. Polmear, *General Introduction, Light Alloys: From Traditional Alloys to Nanocrystals*, 4th Ed., Elsevier Butterworth-Heinemann publications, Oxford, United Kingdom (2006).

2. E. L. Rooy, *Aluminium Alloy Castings: Properties, Processes and Applications,* ASM International, Materials Park, Ohio, USA (2004).

3. J. G. Kaufman, *Introduction to Aluminium Alloys and Tempers*, ASM International, Materials Park, Ohio, U.S.A (2000).

4. J. R. Davis; Corrosion of Aluminium Alloys. ASM International, Materials Park, Ohio, U.S.A (1999).

5. W. F. Hosford, *Physical Metallurgy*, Taylor and Francis Group, Florida, U.S.A (2005).

6. F. A. Fasoyinu, J. Thomson, T. Castles and M. Sahoo, "Mechanical Properties and Metallography of Al-Mg Alloy 535.0", *AFS Transactions*, Vol. 02 (2003), pp. 1-13.

7. St. Paul's Brass and Aluminium Foundry Aluminium-Magnesium Family 535.0, http://www.spba.net/pdf/almg535.pdf, cited on February 4th, 2009.

8. F. A. Fasoyinu, J. Thomson, T. Castles and M. Sahoo, "Gravity Permanent Mold Casting of Al-Mg Alloy 535", *AFS Transactions*, Vol. 02 (2002), pp. 1-19.

9. J. E. Hatch, Ed., *Aluminium: Properties and Physical Metallurgy*, ASM International, Ohio, U.S.A (1988).

10. Y. Bagaryatskii, "Mechanism of Artificial Aging of Aluminium-Copper-Magnesium Alloys", *Doklady Akademii Nauk SSSR*, Vol. 87 (1952), pp. 559-562.

11. R. Wilson and P. G. Patridge, "The Nucleation and Growth of S' Precipitates in an Aluminium-2.5% Copper-1.2% Magnesium Alloy", *Acta Materialia*, Vol. 13 (1965), pp. 1321-1327.

12. J. Silcock, "The Structural Aging Characteristics of Al-Cu-Mg Alloys with Copper:Magnesium Weight Ratios of 7:1 and 2.2:1", *Journal of the Institute of Metals*, Vol. 89 (1960-61), pp. 203-210.

13. I. N. A. Oguocha, *Ph.D. Thesis,* Characterization of Aluminium Alloy 2618 and Its Composite containing Alumina Particles, Dept. of Mechanical Engineering, University of Saskatchewan, Saskatoon, Canada, 1999.

14. H. Lu, P. Kadolkar, K. Nakazawa, T. Ando and C. A. Blue, "Precipitation Behaviour of AA2618", *Metallurgical and Materials Transactions*, Vol. 38A (2007), pp. 2379-2388.

15. R. Wilson and P. J. E. Forsyth, "Effects of Additions of 1% Iron and 1% Nickel on the Age-Hardening of an Aluminium-2.5% Copper-1.2% Magnesium Alloy", *Journal of the Institute of Metals*, Vol. 94 (1966), pp. 8-13.

16. E. Gikunoo, *M.Sc. Thesis*, Effect of Fly Ash Particles on the Mechanical Properties and Microstructure of Aluminium Casting Alloy A535, Dept. of Mechanical Engineering, University of Saskatchewan, 2004.

17. E. R. Obi, I. N. A. Oguocha and R. W. Evitts, "Effect of Fly Ash Reinforcement on the Corrosion Behaviour of Cast Al-Mg Alloy A535 in 3.5 wt.% NaCl Solution", 3rd International Conference on Computational Methods and Experiments in Material Characterization; WITPress, United Kingdom: Bologna, Italy, Vol. 57 (2007), pp. 21-30.

18. P. Cavaliere, "Mechanical Properties of Friction Stir Proceed 2618/Al_2O_3/20_p Metal Matrix Composite", *Composites: Part A*, Vol. 36 (2005), pp. 1657-1665.

19. J. H. Wang and D. Q. Yi, "Preparation and Properties of Aluminium Alloy AA2618 Reinforced by Submicron AlN Particles". *Journal of Materials Engineering and Performance*, Vol. 15 (2006), pp. 596-600.

20. F. Müller and J. Monaghan, Non-Conventional Machining of Particle Reinforced Metal Matrix Composite", *International Journal of Machine Tools and Manufacture*, Vol. 40 (2000), pp. 1351-1366.

21. T. W. Clyne and P. J. Withers, *An Introduction to Metal Matrix Composites*, Cambridge University Press, London, United Kingdom (1995).

22. N. Chawla and K. K. Chawla, *Metal Matrix Composites*, Springer, New York, U.S.A (2006).

23. I. N. A. Oguocha, M. Radjabi and S. Yannacoupoulos, "The Effect of Cooling Rate on the Quench Sensitivity of 2618 Al/Al_2O_3 MMC", *Journal of Materials Science*, Vol. 35 (2000), pp. 5629-5634.

24. J. M. Papazian, "The Effects of SiC of Whiskers and Particles on Precipation in Aluminium Matrix Composites", *Metallurgical and Materials Transactions*, Vol. 19A (1988), pp. 2945-2953.

25. E. Gikunoo, O. Omotoso and I. N. A. Oguocha, "Effect of Fly Ash Addition on the Magnesium Content of Casting Aluminium Alloy A535", *Journal of Materials Science*, Vol. 40 (2005), pp. 487-490.

26. A. D. Mclead and C. M. Gabryel, "Kinetics of the Growth of Spinel, $MgAl_2O_4$, on Alumina Particulate in Aluminium Alloys Containing Magnesium", *Metallurgical. Materials Transactions*, Vol. 23A (1992), pp. 1271-1283.

27. Z. P. Luo, Y. P. Song and S. Q. Zhang, "A TEM Study of the Microstructure of SiC_p/Al Composite Prepared by Pressureless Infiltration Method", *Scripta Materialia*, Vol. 45 (2001), pp. 1183-1189.

28. D. J. Lloyd, "Particle Reinforced Aluminium and Magnesium Matrix Composites", *International Materials Reviews*, Vol. 39 (1994), pp. 1-23.

29. C. Kawai, "Effect of Interfacial Reaction on the Thermal Conductivity of Al-SiC Composites with SiC Dispersions", *Journal of the American Ceramic Society*, Vol. 84 (2001), pp. 896-898.

30. C. Banerji and P. K. Rohatgi, "Cast Aluminium Alloy Containing Dispersoids of TiO_2 and ZrO_2 Particles", *Journal of Material Science*, Vol. 30 (1982), pp. 335-342.

31. B. C. Pai, G. Ramani, R. M. Pillai and K. G. Satyanarayana, "Review: Role of Magnesium in Cast Aluminium Alloy Matrix Composites", *Journal of Material Science*, Vol. 30 (1995), pp. 1903-1911.

32 R. Guo and P. K. Rohatgi, "Chemical Reactions between Aluminium and Fly Ash during Synthesis and Reheating of Al-Fly Ash Composite", *Metallurgical and Materials Transactions*, Vol. 29B (1998), pp. 519-525.

33. I. N. A. Oguocha and S. Yannacopoulos, "Microstructure and Age Hardening Characteristics of 2618 Aluminium Matrix Composites", *Science and Engineering Composite Materials*, Vol. 7 (1998), pp. 229-314.

34. L. D. Wang, W. D. Fei, M. Hu, L. S. Jiang and C. K. Yao, “A study on an aluminium matrix composite reinforced by both *β*–eucryptite particle and aluminum borate whisker”, *Materials Letters*, Vol. 53 (2002), pp. 20-24.

35 S. Lemieux, S. Elomari, J. A. Nemes and M. D. Skibo, Thermal Expansion of Isotropic Duralcan Metal-Matrix Composites. *Journal of Materials Science*, Vol. 33 (1998), pp. 4381-4387.

36 P. K. Rohatgi, D. Weiss and N. Gupta, "Applications of Fly Ash in Synthesizing Low-Cost MMCs for Automotive and Other Applications", *Journal of the Minerals, Metals and Materials*, Vol. 58 (2006), pp. 71-76.

37. C. Park, C. Kim, M. Kim and C. Lee, "The Effect of Particulate Size and Volume Fraction of the Reinforced Phases on the Linear Thermal Expansion in the Al-Si-SiC_p System", *Materials Chemistry and Physics*, Vol. 88 (2004), pp. 46-52.

38. W. D. Fei and L. D. Wang, "Thermal Expansion Behaviour and Thermal Mismatch Stress of Aluminium Matrix Composite Reinforced by β-Eucryptite Particle and Aluminium Borate Whisker", *Materials Chemistry and Physics*, Vol. 85 (2004), pp. 450-457.

39. E. Gikunoo and I. N. A. Oguocha, "Investigation of fly ash-aluminium alloy reaction using XRD and XFS", J. Lo, T. Nishino, S.V. Hao, H. Hamada, A. Nakai and C. Poon, Eds., Proceedings, 6th Joint Canada-Japan Workshop on Composites, DEStech Publications, Inc., Pennsylvania, U.S.A, (2006), pp. 387-396.

40. K. B. Lee, H. S. Sim, S. Y. Cho and H. Kwon, "Reaction Products of Al-Mg/B_4C Composite Fabricated by Pressureless Infiltration Technique", *Materials Science and Engineering,* Vol. 302A (2001), pp. 227-234.

41. N. Sobczak, J. Sobczak, J. Morgiel and L. Stobierski, "TEM Characterization of the Reaction Products in Aluminium–Fly Ash Couples", *Materials Chemistry and Physics*, Vol. 81 (2003), pp. 296-300.

42. A. Forn, M. B. Teresa and E. Rupérez, "Spinel Effect on the Mechanical Properties of Metal Matrix Composite AA6061/$(Al_2O_3)_p$", *Journal of Materials Processing Technology*, Vol. 143-144 (2003), pp. 58-61.

43. C. Badini, P. Fino, M. Musso, P. Dinardo, "Thermal Fatigue Behaviour of a 2014/Al_2O_3-SiO_2 (Saffil® Fibers) Composite Processed by Squeeze Casting", *Materials Chemistry and Physics*, Vol. 64 (2000), pp. 247-255.

44. R. Guo, D. Venugopalan and P. K. Rohatgi, "Differential Thermal Analysis to Establish the Stability of Aluminium-Fly Ash Composites During Synthesis and

Reheating", *Materials Science and Engineering*, Vol. 241A (1998), pp. 1841-1890.

45. J. Mei, R. D. Halldearn and P. Xiao, "Mechanisms of the Aluminium-Iron Oxide Thermite Reaction", *Scripta Materialia*, Vol. 41 (1999), pp. 541-548.

46. L. Yao, G. Sasaki and H. Fukunaga, "Reactivity of Aluminium Borate Whisker Reinforced Aluminium Alloys", *Materials Science and Engineering*, Vol. 225A (1997), pp. 59-68.

47. S. G. Shabestari and M. Malekan, "Thermal Analysis Study of the Effect of the Cooling Rate on the Microstructure and Solidification Parameters of 319 Aluminium alloy", *Canadian Metallurgical Quarterly*, Vol. 44 (2005), pp. 305–312.

48. A. A. Ureina, P. Rodrigo, L. Gil, M. D. Escalera and J. L. Baldonedo, "Interfacial Reactions in an Al-Cu-Mg/SiC_w Composite during Liquid Processing Part I Casting", *Journal of Materials Science*, Vol. 36 (2001), pp. 419-428.

49. D. J. Towle and C. M. Friend, "Effect of Fiber-Matrix-Binder Interactions on the Matrix Composition and Age-Hardening Behaviour of 6061-Based MMCs", *Journal of Materials Science*, Vol. 27 (1992), pp. 2781-2791.

50. K. Mondal, N. Sathitsuksanoh, M. Croft and S. B. Lalvani, "X-Ray Absorption Spectroscopic Analysis of Amorphous Cr-P obtained Via Electrodeposition", *Journal of Materials Science Letters*, Vol. 22 (2003), pp. 655-657.

51. S. Pattanaik, G. P. Huffman, S. Sahu and R. J. Lee, "X-Ray Absorption Fine Structure Spectroscopy and X-Ray Diffraction Study of Cementitious Materials Derived from Coal Combustion by-Products", *Cement and Concrete Research*, Vol. 34 (2004), pp. 1243-1249.

52. E. Piskorska, J. Lawniczak, R. Minikayev, A. Wolska, P. Paszkowicz, N. Bouzoubaa and B. Ewa, "Quantitative Phase Analysis of Cubic Boron Nitride Based Composites by X-Ray Absorption Near Edge Structure", *Spectrochimica Acta*, Vol. 62B (2007), pp. 461-469.

53. D. B. Miracle, "Metal Matrix Composites – from Science to Technological Significance", *Composites Science and Technology*, Vol. 65 (2005), pp. 2526-2540.

54. F. A. Fasoyinu, D. Cousineau and M. Sahoo, "Marrying Almag 535 to the Permanent Mold Process", *Modern Casting*, Vol. 95 (2005), pp. 43-45.

55. P. K. Rohatgi, N. Gupta and S. Alaraj, "Thermal Expansion of Aluminium-Fly Ash Cenosphere Composites Synthesized by Pressure Infiltration Technique", *Journal of Composite Materials*, Vol. 40 (2006), pp. 1163-1174.

56. Military Standardization Handbook: Aluminium and Aluminium Alloys, Washington DC, (1966).

57. Rainèr Cast Parts, Inc., http://rainiercast.com/535.html, cited on March 4th, 2009, adapted from reference [16].

58 S. Q. Wu, Z. S. Wei and S. C. Tjong, "The Mechanical and Thermal Expansion Behaviour of an Al-Si alloy Composite Reinforced with Potassium Titanate Whisker", *Composites Science and Technology*, Vol. 60 (2000), pp. 2873-2880.

59. N. Bouzoubaa and B. Fournier, "Current Situation of SCMs in Canada", *Materials Technology Laboratory Report MTRL* 2003-4(TR), (2003).

60. Cambridge Materials Selector (CES) EduPack, Granta Design Limited, Cambridge, United Kingdom, (2007).

61. Canadian Minerals Yearbook: Natural Resources Canada, Ottawa, (2002).

62. P. K. Rohatgi, R. Q. Guo and D. M. Golden, "Cast Aluminium, Fly Ash Composites for Engineering Applications", *Transactions of the American Foundrymen's Society*, Vol. 103 (1995), pp. 575-579.

63. R. Q. Guo, P. K. Rohatgi and D. Nath, "Preparation of Aluminium-Fly Ash Particulate Composite by Powder Metallurgy Technique", *Journal of Materials Science*, Vol. 32 (1997), pp. 3971-3974.

64. T. P. D. Rajan, R. M. Pillai, B. C. Pai, K. G. Satyanarayana and P. K. Rohatgi, "Fabrication and Characterization of Al–7Si–0.35Mg/fly Ash Metal Matrix Composites Processed by Different Stir Casting Routes", *Composites Science and Technology*, Vol. 67 (2007), pp. 3369-3377.

65. Q. Zhang, G. Wu, L. Jiang and G. Chen, "Thermal Expansion and Dimensional Stability of Al-Si Matrix Composite Reinforced with High Content of SiC", *Materials Chemistry and Physics,* Vol. 82 (2003), pp. 780-785.

66. Y. D. Huang, N. Hort and K. U. Kainer, "Thermal Behaviour of Short Fiber Reinforced $AlSi_{12}CuMgNi$ Piston Alloy", *Composites: Part A*, Vol. 35 (2004), 249-263.

67. S. C. Tjong, K. F. Tam and S. Q. Wu, "Thermal Cycling Characteristics of in-Situ Al-Based Composites Prepared by Reactive Hot Pressing", *Composite Science and Technology*, Vol. 63 (2003), pp. 89-97.

68. H. E. Nassini, M. Moreno and O. C. Gonzalez, "Thermal Expansion Behaviour of Aluminium Alloys Reinforced with Alumina Planar Random Short Fibres", *Journal of Materials Science*, Vol. 36 (2001), pp. 2759-2772.

69. S. O. Kasap, *Principles of Electronic Materials and Devices*, McGraw-Hill Companies, Inc., New York, (2006).

70. J. Sadanandam, G. Bhikshamaiah, B. Gopalakrishna, S. V. Suryanarayana, Y. R. Mahajan and M. K. Jain, "Effect of Different Reinforcements on the Thermal Expansion of 2124 Aluminium Metal-Matrix Composites", *Journal of Materials Science Letters*, Vol. 11 (1992), pp. 1518-1520.

71. S. Sharma, "Effect of Albite Particles on the Coefficient of Thermal Expansion Behaviour of the Al 6061 Alloy Composites", *Metallurgical and Materials Transactions,* Vol. 31A (2000), pp. 773-780.

72. S. Elomari and D. J. Lloyd, "Thermal Expansion Behaviour of Ceramic Particle Reinforced Aluminium Metal Matrix Composites", *Proceedings, Processing, Properties, and Applications of Cast Metal Matrix Composites: a Symposium at the TMS Fall Meeting,* Cincinnati (1996), pp. 201-211.

73. S. Elomari, M. D. Skibo, A. Sundarrajan and H. Richards, "Thermal Expansion Behaviour of Particulate Metal-Matrix Composites", *Composites Science and Technology,* Vol. 58 (1998), pp. 369-376.

74. S. Elomari, R. Boukhili and D. J. Lloyd, "Thermal Expansion of Prestrained Al_2O_3/Al Metal Matrix Composite", *Acta Materialia*, Vol. 44 (1996), pp. 1873-1882.

75. L. Z. Zhao, M. J. Zhao, X. M. Cao, C. Tian, W. P. Hu and J. S. Zhang, "Thermal Expansion of Novel Hybrid SiC Foam-SiC Particles-Al Composites", *Composites Science and Technology*, Vol. 67 (2007), pp. 3404-3408.

76. D. K. Balch, T. J. Fitzzgerald, V. J. Michaud, A. Morteensen, Y-L Shen and S. Suresh, "Thermal Expansion of Metals Reinforced with Ceramic Particles and Microcellular Foams", *Metallurgical and Materials Transactions*, Vol. 27A (1996), pp. 3700-3717.

77. R. A. Schapery, "Thermal Expansion Coefficients of Composite Materials based. on Energy Principles", *Journal of Composite Materials*, Vol. 2 (1968), pp. 380-404.

78. P. S. Turner, "Thermal-Expansion Stresses in Reinforced Plastics", *Modern Plastics*, Vol. 24 (1946), pp. 153-157.

79. E. H. Kerner, "The Elastic and Thermo-Elastic Properties of Composite Media", *Proceedings, the Physical Society Section B*, Vol. 69 (1956), pp. 808-813.

80. N. Chen, H. Zhanga, M. Gua and Y. Jina, "Effect of Thermal Cycling on the Expansion Behaviour of Al/SiC_p Composite", *Journal of Materials Processing Technology*, Vol. 209 (2009), pp. 1471-1476

81. S. Elomari, R. Boukhili, C. S. Marchi, A. Mortensen and D. J. Lloyd, "Thermal Expansion Responses of Pressure Infiltrated SiC/Al Metal-Matrix Composites", *Journal of Materials Science*, Vol. 32 (1997), pp. 2131-2140.

82. Y. Fei, Thermal Expansion; Mineral Physics and Crystallography: A Handbook of Physical Constants; Mineral Physics and Crystallography: A Handbook of Physical Constants AGU Reference Shelf 2, Washington, U.S.A. (1995), pp. 29-44.

83. Z. Hashin and S. A. Shtrikman, "Variational Approach to the Theory of the Elastic Behaviour of Multiphase Materials", *Journal of Mechanics Physical Solids*, Vol. 11 (1963), pp. 127-140.

84. M. W. Chase, C. A. Davies, J. R. Downey Jr., D. J. Frurip, R. A. Mcdonald and A. N. Syverud, "JANAF Thermodynamical Tables", *Journal of Physical Chemistry Reference Data*, Vol. 14, Sppl. 1, (1985).

85. V. Massardier, P. Kerdelhue, P. Merle and J. Besson, "Experimental Study of the Interaction of Magnesium with the Reinforcement in Al-Mg-Si Alloy/Î±-Alumina Platelet Composites", *Materials Science and Engineering*, Vol. 191A (1995), pp. 267-276.

86. Z. R. Xu, K. K. Chawla, R. Mitra and M. E. Fine, "Effect of Particle Size on the Thermal Expansion of TiC/Al XD^{TM} Composite", *Scripta Metallurgica*, Vol. 31 (1994), pp. 1525-1530.

87. M. Kobashi and T. Choh, "Wettability and the Reaction for SiC Particle/Al Alloy Sysytem", *Journal of Material Science*, Vol. 28 (1993), pp. 684-690.

88. G.Yang, T. Fan and D. Zhang, "Chemical Reaction in Al Matrix Composite Reinforced with SiC_p Coated by SnO_2", *Journal of Materials Science*, Vol. 39 (2004), pp. 3689-3694.

89. T. Sritharan, L. S. Chan, L. K. Tan and N. P. Huang, "A Feature of the Reaction between Al and SiC Particles in an MMC", *Materials Characterization*, Vol. 47 (2001), pp. 75-77.

90. J. Pelleg, D. Ashkenazi and M. Ganor, "The Influence of a Third Element on the Interface Reactions in Metal-Matrix Composites (MMC): Al–graphite System", *Materials Science and Engineering*, Vol. 281A (2000), pp. 239-247.

91. H. Q. Gao and W. D. Fei, "Interfacial Reaction and Tensile Properties of 6061Al Matrix Composite Reinforced with Copper-Coated $Al_{18}B_4O_{33}$ Whiskers", *Materials Letters*, Vol. 59 (2005), pp. 3756-3760.

92. S. Ren, X. He, X. Qu and Y. Li, "Effect of Controlled Interfacial Reaction on the Microstrucure and Properties of the SiC_p/Al Composites Prepared by Presureless Infiltration", *Journal of Alloys and Compounds*, Vol. 455 (2008), pp. 424-431.

93. J. C. Lee, G. H. Kim and H. I. Lee, "Characterization of Interfacial Reaction in $(Al_2O_3)_p$/6061 Aluminium Alloy Composite", *Materials Science and Technology*, Vol. 13 (1997), pp. 182-186.

94. G. Gorge and I. Pinkrings, Geology 898 Class Note, University of Saskatchewan, (2006).

95. Z. Zou, Y. F. Hu, T. K. Sham, H. H. Huang, G. Q. Xu, C. S. Seet and L. Chan, "XAFS Studies of Al/TiN_x Films on Si(100) at the Al K- and $L_{3,2}$-Edge", *Journal of Synchrotron Radiation*, Vol. 6 (1999), pp. 524-525.

96. M. Kasrain, Z. Yin, G. M. Bancroft and K. H. Tan, "Sampling depth of total Electron and Fluorescence Measurements in Si L- and K-edge Absorption Spectroscopy", *Journal of Vacuum Science and Technology*, Vol. 11A (1993), pp. 2694-2699.

97. J. A. van Bokhoven, H. Sambe, D. E. Ramaker and D. C. Koningsberger, "Al K-edge Near-Edge X-ray Absorption Fine Sructure (NEXAFS) Study on the Coordination Structure of Aluminium in Minerals and Y Zeolites", *Journal of Physical Chemistry B*, Vol. 103 (1999), pp. 7557-7564.

98. S. B. Lalvani, K. Mondal, N. Sathitsuksanoh, T. Wiltowski and Y. Xiao, "Characterization of Ni-P and Fe-P by X-Ray Absorption Spectroscopy", *Journal of Materials Science Letters*, Vol. 20 (2001), pp. 1097-1098.

99. R. E. Watson, J. Hudis and M. L. Perlman, "Charge Flow and *d* Compensation in Gold Alloys", *Physical Review B*, Vol. 4 (1971), pp. 4139-4144.

100 R. Blyth, "Sperical Grating Monochromator (SGM) Beamline 11ID-1", *Canadian Light Source Annual Report*, (2005-2006), Saskatoon, pp. 145-147.

101 Y. F. Hu, L. Zuin, G. Wright, M. Igarashi, S. Y. Wilson, T. Chen, B. W. Maxwell, B. W. Yates, T. K. Sham and R. Reininger, "Commisioning and Performance of the Variable Line Spacing Plane Grating Monochromator Beamline", *Canadian Light Source Review of Scientific Instruments*, Vol. 78 (2007), 083109-1-083109-5.

102. R. Van Basshuysen and F. Schafer, Eds., *Internal Combustion Engine Handbook: Basics, Components, Systems, and Perspective*, SAE International, Warrendale, Pennsylvania, USA, (2002).

103. Setsoft 2000 User's Manual Version 3.0, Seteram Inc., Paris, France.

104. C. Haavik, S. Stolen, H. Fjellvag, M. Hanfland and D. Hausermann, "Equation of State of Magnetite and its High-Pressure Modification: Thermodynamics of the Fe-O System at High Pressure", *American Mineralogist*, Vol. 85 (2000), pp. 514-523.

105. M. J. Starink and A. M. Zahra, "β' and β Precipitation in an Al-Mg Alloy Studied by DSC and TEM", *Acta Materialia*, Vol. 46 (1998), pp. 3381-3397.

106. H. Kang, "Microstructure and Electrical Conductivity of High Volume Al_2O_3-Reinforced Copper Matrix Composites Produced by Plasma Spray", *Surface Coatings Technology*, Vol. 190 (2005), pp. 448-452.

107. S. M. Zebarjad and S. A. Sajjadi, “Dependency of Physical and Mechanical Properties of Mechanical Alloyed Al–Al_2O_3 Composite on Milling Time”, *Materials Design*, Vol. 28 (2007), pp. 2113-2120.

108. G. Calas, A. M. Flank, P. Lagarde and P. Ildefonse, "Low Z Elements (Mg, Al, and Si) K-Edge X-Ray Absorption Spectroscopy in Minerals and Disordered Systems", *Nuclear Instruments and Methods in Physics Research*, Vol. 97 (1995), pp. 172-175.

APPENDIX

Appendix A. Operational Manuals

The standard operational procedures for carrying out experiments using the Seteram DSC111 and Setsys Evolution 2000 Thermomechanical Analyser are presented in this section.

A.1.0 Standard Operational Procedure for Seteram TG-DSC 111

The standard operational procedure for carrying out experiments using the Setsys TG-DSC111 is presented in this sub-section.

A.1.1 Setting-up Experiment

1. Important notes
    a. Before opening the furnace, check the furnace temperature to see if it has dropped down to about 25 ^{o}C. The following steps should be followed to check the furnace temperature.
        i. Open the Setsoft 2000 software by double-clicking on the icon on the desktop of the computer connected with the DSC and enter your password.
        ii. Take the mouse to the top left hand corner of the computer screen to display **acquisition, processing, tools, preference and connected apparatus moduli** tabs
        iii. Click on **acquisition** module tab. In the acquisition module, click on the **acquisition** drop down menu, **new acquisition**
        iv. Click on the **display** drop down menu and then on **real time**.

b. The minimum sample weight should be **45 mg** to improve the sensitivity of the measurements.

c. The temperature-time profile that the samples will be exposed to must start with isothermal heat treatment for at least 30 minutes in order to harmonize the furnace temperature with that of the sample.

d. Do not use Aluminium crucibles for experiments that go beyond 600 ^{o}C.

e. Steel crucibles can be used for temperature range above 600^{o}C. The steel lids should be fastened with either an Al or Ni O-ring. The Al O-rings should be used at a temperature range below 600 ^{o}C.

2. Measure the weight of the crucible and that of the crucible containing the sample. Determine the sample weight by subtracting the weight of the crucible from that of the crucible containing the sample.

3. Insert both the blank and reference crucibles (empty crucibles) into the slots in the furnace labeled "blank" and "sample", respectively.

4. Ensure that the crucibles are placed in the middle of the furnace by either inserting the positioning rod gently into the furnace or using a hook to hang the crucible from the sample holder.

5. Connect the **inlet gas** tubing system to the furnace inlet valve.

6. Open the **low flow** valve gently for the carrier gas to flow into the furnace. Please, do not open the **high flow** valve.

7. Configure the Setsoft 2000 software

   a. Click on **Acquisition** drop down menu, **New Acquisition**, and select DSC 111 in the **Select Apparatus** dialogue box before clicking **OK**.

   b. The **Experiment Explorer** dialogue box is displayed on clicking the **OK** button on the **Selected Apparatus** dialogue box.

   c. In the **Description** menu, enter the name of the experiment, comment, mass of sample etc.

   d. In the **Parameter** menu, ensure that the sample safety temperature is at least 20 ^{o}C greater than the maximum programmed temperature, set the **stop** mode to **pause**, and chose **sample** under "**temperature of**".

e. Right click on **the zones** to display a menu with "**Add zone, copy, paste, delete**". These functions adjust the zones to the desired temperature-time profile.

f. Right click on the **entered values** in the **List of Sequence** dialogue box to display the menu "**Add isotherm**, **Add ramp**, **Paste**, **Delete**". Make necessary adjustments by selecting the required functions.

g. Click on the **entered values** in the **list of sequence dialogue** box. Change "initial and final temperature and time". Click on the arrow pointing downward to save the adjustments made.

h. Check the "**save acquisition of zone**" box to save the result of the zones of interest.

i. Click on **start experiment** icon (displayed with a symbol of a man running) when all zones have been created or adjusted to the desired experimental set up.

j. Click on **display** and then on real time programming to display heat flow, temperature-time profile.

8. Repeat step 7 with blank (empty) crucible and the crucible containing the sample using the same temperature-time profile as that of the blank and the reference.

A.1.2 Data Processing

1. Click on **processing** module at the top left corner of the screen to load the test samples data-files.
2. Click on the **experiment** dropdown menu and click **open** to open the experiment dialogue box
3. On the experiment dialogue box,
   i. Check either **experiment in progress** or **done** box and hit the **apply criteria** button.
   ii. Highlight the name of the experiment of interest and click on **OK**
4. Baseline Subtraction
   a. Click on **zone**

b. Click on **subtract baseline**

c. Click on **OK**

d. Select the baseline (data from the blank experiment) to be subtracted and the zone of interest

e. Click on **OK**

5. To export the data as **ASCII** or **.XLS** files, click on zone and select export.

6. Enthalpy Calculation

a. Highlight heat flow

b. Click on the **processing** dropdown menu

c. Click on **integration**

d. Click on a point on the curve before and after the peak of interest

e. Click on **OK**

f. Select the baseline

g. Select desired enthalpy unit

h. Click on the print icon to print the result

7. Delete

a. Click on the **Tool module** Take the mouse to the top left hand corner of the computer screen to display

b. Click on **Experiment** dropdown menu

c. Click on **Modify**

d. Highlight the experiment of interest

e. Click on **OK**

A.1.3 Miscellaneous Information

1. Changing from Horizontal to Vertical Set up

a. Remove inlet and outlet tubing gas systems

b. Remove the crucible by unscrewing the right side of the platform. Remove the cover.

c. Pull the furnace out slowly

d. Erect the furnace vertically and screw it back at the back (with 4 screws)

e. Reconnect the cover

1. Archiving an Experiment

a. Click on the **Tools Module**

b. Click on **Experiment** drop down menu in the menu bar

c. Click on **archive**

d. Select the experiment of interest

e. Click on **OK**

f. Click on **OK** in the resulting dialogue box

g. Click on **open** in the Open dialogue box-noting the destination drive

h. Click on **start** in the storage dialogue box

i. Click on **OK** when dialogue box for successful execution of procedure appears

j. If desktop is the destination drive, click on Courbes folder on the desktop

k. Click on Acquis sub-folder within Courbes

l. Attach the **.DAT** file to email.

A.2.0 Standard Operational Procedure for Setsys Evolution 2000 Thermomechanical Analyser

A.2.1 Setting-up Experiment

1. Important notes:

a. In order to avoid thermal shock of the material used in lining the furnace, the furnace temperature **must be below 50^{o}C** when changing sample.

b. Check the water temperature, and the gas and water flow rate

i. Minimum carrier gas flow rate: 300-400 psi.

ii. Minimum water flow rate: 3.4 L/min

iii. Water temperature: 15-20 ^{o}C.

c. The recommended carrier gas is nitrogen. However, argon and helium gas can also be used. The carrier gas that I used for my TMA and DSC experiments was “4.8 purity argon gas”.

Warning: Do not use nitrogen gas as the carrier gas above 1000 ^{o}C.

d. Allow the gas to flow for at least 30 minutes before the start of the experiment.

e. Ensure that at least 8 green LEDs on the TMA are lit.

2. Open the plastic hood that covers the TMA.

3. Use the **power button** to bring the sample holder, with the sample on it, out of the furnace.

4. Cover the **furnace hole** with a lid to prevent the sample from dropping into the furnace.

5. Open the Setsoft 2000 software by double-clicking on the icon and entering your password.

6. Take the mouse to the top left hand corner of the computer screen to display **acquisition, processing, tools, preference and connected apparatus moduli.**

7. Click on **acquisition modulus** to display **select apparatus** dialogue box.

8. On the **select apparatus** dialogue box, select **Setsys Evolution – 1200** and click on **OK**.

9. Click on **acquisition** drop down menu, **new acquisition**, the **display** drop down menu and then **real time or direct programming**.

10. Click on **Direct programming** to display the **Manual programming -, PID -, TMA - Setsys Ev 1200 (TMA Al)** dialogue boxes.

11. On the **TMA - Setsys Ev 1200 (TMA Al)** dialogue box, click the **up arrow** to move the probe upward direction.

12. Place the sample on the **sample holder.** The sample should be placed in such a way that the probe will sit in the middle of it.

13. On the **TMA - Setsys Ev 1200 (TMA Al)** dialogue box,

    a. Click the **down arrow** to drop the probe on the sample.

    b. Adjust the **release control knob** on the TMA to bring the **TMA without tare** to zero.

    c. When the **TMA without tare** becomes stable and approximately zero, lock the **release control knob** using the **locking knob** on the TMA.

14. On the **Manual programming - Setsys Ev 1200 (TMA Al)** dialogue box, click

on **modify** to change the load on the sample.

a. Make sure that the P, I, D, U are set to 300, 700, 0, 0, respectively.

b. Minimum load: 5 g

c. Weigh the probe periodically by clicking on probe weight before starting new set of experiments to make sure that the probe weight is approximately 64 mg.

15. Close the **Manual programming-, PID-, TMA- Setsys Ev 1200 (TMA Al)** dialogue boxes.

16. Remove the lid that used in furnace hole.

17. Use the power button to put back the sample into the furnace.

18. Close the cover of the TMA.

19. Software Configuration (Setting the Temperature-Time profile)

a. On the **acquisition** dialogue box, click on **collection** to display **new acquisition**.

b. Click on **new acquisition** to display the **experiment explorer** dialogue box.

c. On the **experiment explorer** dialogue box,

i. Right click on the zones to display the menu "**Add zone, Copy, Paste, delete**". Make the necessary adjustments.

ii. Right click on the entered values in the **list of sequence** to display the menu, "**Add isotherm, Add ramp, Paste, Delete**". Make the necessary adjustments.

iii. Left click on the entered values in the **list of sequence** to change the information on **description of sequence (**initial and final temperatures, time, flow rate and load).

Important note: In all experiments, stabilize the system for at least 30 minutes before ramping.

Warning: Always ramp to a temperature below the melting temperature of the test sample to avoid the melt from damaging the thermocouples in the TMA.

20. Run the same experimental set-up for the blank (the probe making contact with

the sample holder), sapphire (the reference material) and the test samples.

A.2.2 Data Processing

1. Click on **processing** module at the top left corner of the screen to load the test samples data-files.
2. Click on the **experiment** dropdown menu and click **open** to open the experiment dialogue box
3. On the experiment dialogue box,
   i. Check on either **experiment in progress** for an experiment in progress or done for an experiment that has been completed and hit the **apply criteria** button.
   ii. Highlight the name of the experiment of interest and click **OK**
4. In order to calibrate the data of interest using the reference materials, click on **zone** and select **TMA correction.** This will pop up the experiment dialogue box.
5. Select the standard reference material on the experiment dialogue box and click **OK.** This pops up the signals selection dialogue box.
6. Select temperature and displacement on the **signals selection dialogue** box, and click **OK.** This pops up the TMA correction dialogue box.
7. Select the probe and standard materials from the catalog on the TMA correction dialogue box and click on **OK.** This pops up the processing dialogue box.
8. Right click on the **displacement correction** in the processing dialogue box to **save signal.**
9. To export the data as **ASCII** or **XLS** files, highlight the data of interest; click on **zone** dropdown menu and on **export**.

Appendix B A535 and Its MMCs

B.1.0 Sample Calculations of the CTE of A535 and Its MMCs

Table B.1.1. Properties of A535, Al-5wt.% Mg, some oxides in fly ash, and silicon carbide.

Materials	Bulk Modulus (GPa)	Shear Modulus (GPa)	CTE (μ /^{o}C)	References
A535	---	---	26.6	[7]
Al-5 wt.% Mg	26.1	75.5	---	[60]
Alumina	322.5	180	8.1	[60]
Silica	35.9	28.6	1.2	[60]
Magnetite	222	60.3	8.72	[84, 105]
Silicon carbide	221	200	4.1	[60]

Table B.1.2. Densities of the constituents of fly ash.

Element	SiO_2	Al_2O_3	Fe_2O_3
Density (Kg/m^3)	2197.7	961	5200

Table B.1.3. Vol.% of the constituents of fly ash.

Element	SiO_2	Al_2O_3	Fe_2O_3
Vol. fraction	0.534	0.605	0.121

$$\text{Vol.\%}_{\text{compound}} = \frac{\rho_{\text{composite}}}{\rho_{\text{compound}}} \times \text{Wt.\%}_{\text{compound}}$$

$$\text{Vol.\%}_{SiO_2} = \frac{\rho_{\text{composite}}}{\rho_{SiO_2}} \times \text{Wt.\%}_{SiO_2}$$

$$\text{Vol.\%}_{SiO_2} = \frac{2620\text{kgm}^{-3}}{2197.7\text{kgm}^{-3}} \times 44.8 = 53.4$$

$$\text{Vol. fraction} = \frac{53.4}{100} = 0.534$$

CTE and bulk and shear modulus of fly ash

$$\text{CTE}, \alpha = \left(0.534 \times 1.2 \times 10^{-6} + 0.605 \times 8.1 \times 10^{-6} + 0.121 \times 8.72 \times 10^{-6}\right)^{\circ}\text{C}^{-1} = 8.15\,\mu^{\circ}\text{C}^{-1}$$

$$\text{Bulkmodulus}, \text{K} = \left(0.534 \times 322.5 \times 10^{9} + 0.605 \times 35.9 \times 10^{9} + 0.121 \times 222 \times 10^{9}\right)\text{Pa}$$
$$= 241.2\,\text{GPa}$$

$$\text{Shear modulus}, \text{G} = \left(0.534 \times 180 \times 10^{9} + 0.605 \times 28.6 \times 10^{9} + 0.121 \times 60.3 \times 10^{9}\right)\text{Pa}$$
$$= 152.7\,\text{GPa}$$

Sample calculations for the CTE of A535/Fly ash/10p using ROM and models predicted by Turner, Kener and Schapery.

(a) ROM

$$\overline{\alpha}_c = \alpha_m V_m + \alpha_r V_r$$
$$= \left(0.9 \times 26.6 \times 10^{-6} + 0.1 \times 8.15 \times 10^{-6}\right)^{\circ}\text{C}^{-1}$$
$$= 24.7\,\mu^{\circ}\text{C}^{-1}$$

(b) Turner's model

$$\alpha_c = \frac{\alpha_r V_r K_r + \alpha_m V_m K_m}{V_r K_r + V_m K_m}$$
$$= \frac{\left(26.6 \times 10^{-6} \times 0.9 \times 26.1 \times 10^{9} + 8.15 \times 10^{-6} \times 0.1 \times 241.2 \times 10^{9}\right)}{\left(0.9 \times 26.1 \times 10^{9} + 0.1 \times 241.2 \times 10^{9}\right)}$$
$$= 17.2\,\mu^{\circ}\text{C}^{-1}$$

(c) Kener's model

$$\alpha_c = \overline{\alpha}_c + V_r * (1 - V_r) * (\alpha_r - \alpha_m) * \left[\frac{K_r - K_m}{(1 - V_r)K_m + V_r K_r + (3K_r K_m / 4G_m)}\right]$$

$$= 23.9\,\mu^{o}C^{-1} + 0.1 \times 0.9 \times \left(8.15 \times 10^{-6} - 26.6 \times 10^{-6}\right)^{o}C^{-1} \times$$
$$\left[\frac{(241.2 - 26.1)\,GPa}{0.9 \times 26.1\,GPa + 0.1 \times 241.2\,GPa + \left(3 \times 241.2 GPa \times 26.1\,GPa \Big/ 4 \times 75.5\,GPa\right)}\right]$$
$$= 23.6\,\mu^{o}C^{-1}$$

(d) Schapery model

i) Upper limit:

$$K_c^{upper} = K_r + \left[\frac{V_m}{\frac{1}{K_m - K_r} + \frac{V_r}{K_r + 4\frac{G_r}{3}}}\right]$$

$$= 241.2\,GPa + \left[\frac{0.9}{\frac{1}{26.1 GPa - 241.2\,GPa} + \frac{0.1}{241.2\,GPa + 4\frac{152.7\,GPa}{3}}}\right]$$

$$= 23.1\,GPa$$

$$\alpha_c = \overline{\alpha}_c + \left[\frac{4G_m}{K_c}\right]\left[\frac{(K_c - K_r)(\alpha_m - \alpha_r)V_r}{4G_m + 3K_r}\right]$$

$$= 24.5\,\mu^{o}C^{-1} + \left[\frac{4 \times 75.5\,GPa}{35\,GPa}\right] \times \left[\frac{(35\,GPa - 241.2\,GPa \times (26.6 - 8.15)\,\mu^{o}C^{-1} \times 0.1}{4 \times 75.5\,GPa + 3 \times 241.2\,GPa}\right]$$

$$= 17.0\,\mu^{o}C^{-1}$$

ii) Lower limit

$$K_c^{lower} = K_m + \left[\frac{V_r}{\frac{1}{K_r - K_m} + \frac{V_m}{K_m + 4\frac{G_m}{3}}} \right]$$

$$= 26.1\,\text{GPa} + \left[\frac{0.1}{\frac{1}{241.2\,\text{GPa} - 26.1\,\text{GPa}} + \frac{0.9}{26.1\,\text{GPa} + 4 \times \frac{75.5\,\text{GPa}}{3}}} \right]$$

$$= 34.6\,\text{GPa}$$

$$\alpha_c = \overline{\alpha}_c + \left[\frac{4G_r}{K_c} \right] \left[\frac{(K_c - K_m)(\alpha_r - \alpha_m)V_m}{4G_r + 3K_m} \right]$$

$$= 24.5\,\mu^{\circ}\text{C}^{-1} + \left[\frac{4 \times 241.2\,\text{GPa}}{35\,\text{GPa}} \right] \left[\frac{(35\,\text{GPa} - 26.1\,\text{GPa} \times (8.15 - 26.6)\,\mu^{\circ}\text{C}^{-1} \times 0.9}{4 \times 75.5\,\text{GPa} + 3 \times 26.1\,\text{GPa}} \right]$$

$$= 16.8\,\mu^{\circ}\text{C}^{-1}$$

B.2.0 Peak temperatures and enthalpies of the reaction peaks in A535 and its MMCs (second sample)

Table B.2.1. Peak temperatures and enthalpies of the reaction peaks in the thermograms of A535.

		Sample 1	Sample 2
Heating		Peak *c*	Peak *c*
	Temp. (^{o}C)	643.5	647.0
	Enthalpy (kJ/Kg)	306.6	320.46
Cooling		Peak *c′*	Peak *c′*
	Temp. (^{o}C)	603.1	604.1
	Enthalpy (kJ/Kg)	-307.1	-310.1

Table B.2.2. Peak temperatures and enthalpies of the reaction peaks in the thermograms of A535/Hybrid/10_p.

		Sample 1	Sample 2	Sample 1	Sample 2
Heating		Peak *b*	Peak *b*	Peak *c*	Peak *c*
	Temp. (^{o}C)	613.2	614.0	646.8	648.4
	Enthalpy (kJ/Kg)	17.0	21.1	31.1	44.0
Cooling		Peak *b*′	Peak *b*′	Peak *c*′	Peak *c*′
	Temp. (^{o}C)	571.1	567.2	608.5	605.0
	Enthalpy (kJ/Kg)	-56.3	-51.5	-134.4	-137.2

Table B.2.3. Peak temperatures and enthalpies of the reaction peaks in the thermograms of A535/Fly ash/10_p.

		Sample 1	Sample 2	Sample 1	Sample 2
Heating		Peak *b*	Peak *b*	Peak *c*	Peak *c*
	Temp. (^{o}C)	616.5	616.8	654.3	654.5
	Enthalpy (kJ/Kg)	30.9	33.7	65.1	79.3
Cooling		Peak *b*′	Peak *b*′	Peak *c*′	Peak *c*′
	Temp. (^{o}C)	569.1	565.3	606.9	605.2
	Enthalpy (kJ/Kg)	-21.1	-5.5	-187.1	-242.7

Table B.2.4. Peak temperatures and enthalpies of the reaction peaks in the thermograms of A535/Fly ash/15_p.

		Sample 1	Sample 2	Sample 1	Sample 2
Heating		Peak *b*	Peak *b*	Peak *c*	Peak *c*
	Temp. (^{o}C)	613.3	614.0	653.0	652.8
	Enthalpy (kJ/Kg)	32.8	43.2	60.5	65.9
Cooling		Peak *b*′	Peak *b*′	Peak *c*′	Peak *c*′
	Temp. (^{o}C)	558.7	565.7	606.5	606.5
	Enthalpy (kJ/Kg)	-22.4	-23.7	-177.6	-179.4